Doctoral Dissertation

Mechanical Performance of Laser-arc Hybrid Welded Joints for Steel Bridge Members

Chen Gang

June 2024

Department of Civil Engineering

Division of Global Architecture

Graduate School of Engineering

Osaka University

Abstract

To extend the application of laser-arc hybrid welding to the joining of thick steel bridge members, this study validated the effectiveness of laser-arc hybrid welding in fabricating these components. Additionally, the mechanical performance of hybrid-welded joints was evaluated through a comparative analysis with joints produced using conventional arc welding. A comprehensive series of experiments and numerical simulations was conducted to facilitate this comparison.

Weld cracking tests were performed on SBHS (Steels for Bridge High-performance Structure) with 15 mm in thickness to identify the appropriate welding condition for achieving one-pass full-penetration welding with sound welds. Using the established welding conditions, butt joints were fabricated. For comparative analysis, the same dimensional butt joints were also produced by arc welding. To elucidate the intricate distribution of welding deformation and residual stress in the as-welded joints, a thermal elastic-plastic analysis was performed. A thermal elastic-plastic analysis model for hybrid welding was developed by combining the different heat sources of laser and arc welding. The experiments and numerical analyses demonstrated that, compared to arc welding, hybrid welding reduced welding time by 98%, angular distortion by 95%, and the range of tensile residual stress in the longitudinal direction by approximately 50%. It is, therefore, validated that laser-arc hybrid welding is effective in the fabrication of steel bridge members.

The mechanical performance of hybrid-welded joints was evaluated from three perspectives: fatigue properties, toughness, and load-carrying capacity. The fatigue properties of the hybrid-welded butt joints were assessed through a comparison with their arc-welded counterparts. Four-point bending fatigue tests confirmed that the hybrid-welded joints met the class D design curve of JSSC, whereas the arc-welded joints underperformed at higher stress levels. The toughness of the hybrid-welded joints made of SBHS was verified by Charpy impact tests. Fracture Path

Deviation (FPD) occurred in all test pieces. As an alternative approach, simulated test pieces made of SBHS were meticulously fabricated using simulated thermal cycle tests to closely replicate the actual metallographic structures. For comparative purposes, conventional SM400B steel underwent the identical simulated thermal cycle tests as the simulated test pieces. These simulated test pieces of SBHS and SM400B were then subjected to Charpy impact tests. The test results indicated that at higher temperature levels (1200°C and 1350°C), SM400B's Charpy absorbed energy did not reach 27 J, while SBHS consistently achieved 47 J. The load-carrying capacity of hybrid-welded columns with L-shaped sections was evaluated by comparing them to their arc-welded counterparts. Monotonic compressive loading experiments were conducted on both types of columns. The results indicated that, compared to arc-welded columns, the average elastic stiffness of the hybrid-welded columns demonstrated a 25% enhancement, and the maximum average compressive load exhibited by these hybrid-welded columns increased by 5%. Accordingly, the mechanical performance of hybrid-welded joints was superior to those of arc-welded ones.

Therefore, laser-arc hybrid welding technology demonstrated its feasibility in the connection of steel bridge structural components, effectively enhancing manufacturing efficiency and improving structural performance and sustainability.

Table of content

Chapter 1 Introduction

1.1 Research Background

1.1.1 Laser-arc Hybrid Welding

The joining technology for steel bridge structural components has evolved from rivet connections to bolt connections and then to welded connections. Welded connections offer numerous advantages such as design flexibility and lightness and are widely used alongside bolting for joining steel bridge components. Various welding methods are available, including arc welding, gas welding, and electron beam welding. Among these, arc welding has been the most commonly used due to its long-standing technical development and high reliability [1.1].

In recent years, laser welding has garnered significant attention as a technique for welding metal components [1.2]. Utilizing the thermal energy from laser irradiation, laser welding offers a considerably higher energy density compared to arc welding. This capability allowed for high-speed, deep-penetration welding, and low heat input [1.3] [1.4], a feature not possible with conventional arc welding. The deep penetration characteristic reduces the number of welding passes necessary to achieve the required throat thickness, and the low heat input effectively minimizes welding deformation, thereby shortening the post-weld distortion correction process [1.5]. Consequently, laser welding has been increasingly employed in the production of high-precision, low-distortion, and low-heat input components, notably within the automotive industry [1.6]. Advances in the power, efficiency, and performance of laser equipment have further enhanced the feasibility of laser welding for thick steel plates in structural applications. Unlike traditional welding methods that necessitate groove processing for joining thick plates, laser welding eliminates this requirement. However, it necessitates meticulous management of the gap between steel plates to prevent defects such as misalignment of the laser focus [1.7], inadequate penetration, undercut [1.8], underfill [1.9], and other welding imperfections [1.10],

[1.11], [1.12], [1.13], [1.14]. Additionally, the high energy density in a confined area can induce rapid heating and cooling, potentially causing hardening [1.15], [1.16] and cracking [1.17], [1.18] in the welded joints, thereby complicating the selection of optimal welding parameters.

To address these challenges, the application of laser-arc hybrid welding, commonly referred to as hybrid welding, has been explored across various industrial sectors [1.19], [1.20], [1.21] [1.22]. This technique synergistically combines the advantages of laser welding and arc welding. In hybrid welding, the process leverages the high speed and deep penetration of laser welding [1.23], [1.24], [1.25]. Simultaneously, the arc welding wire supplies filler metal, thereby increasing the permissible gap tolerance compared to laser-only welding [1.26], [1.27] and reducing the occurrence of welding defects. While the heat input is higher than that of laser welding, it remains significantly lower than in conventional arc welding [1.28], presenting a promising solution for steel structure applications. This method not only enhances welding efficiency but also improves the overall structural integrity of the welds, making it a viable option for critical engineering projects. The ability to achieve high-quality welds with reduced deformation and enhanced strength underscores the potential of hybrid welding in advancing modern construction techniques. Consequently, hybrid welding has been gaining traction as a preferred method for the fabrication and assembly of large-scale steel structures [1.30], addressing both performance and reliability requirements in contemporary engineering.

1.1.2 High-performance Steel

High-performance steel (HPS) is distinguished by its outstanding strength, weldability, and toughness, enabling cost savings and productivity improvements in steel bridge construction compared to traditional steel grades. Research has shown that hybrid designs integrating HPS with conventional steel grades can achieve significant reductions in both steel weight and overall

costs [1.31]. Japan's innovative steel grade, SBHS (Steels for Bridge High-performance Structure), developed through thermo-mechanical controlled processing (TMCP), exemplifies these improvements. SBHS, standardized by JIS G3140 in 2008, is noted for its high strength, toughness, weldability, and workability. For example, SBHS500 was used in 10,000 tons of the 20,000-ton steel weight in the three-span continuous composite truss bridge section of the Tokyo Gate Bridge, achieving a 3% reduction in steel weight and a 12% reduction in total cost [1.32]. Consequently, SBHS was selected for this investigation, as its application in fabricating steel bridge components is expected to reduce construction costs and enhance the durability of steel structures.

1.1.3 Characteristics of Welded Joints

(a) Fatigue property

Fatigue performance is critical to the structural integrity and longevity of steel bridges. Bridges are subjected to repeated cyclic loads from traffic, wind, and environmental changes, making fatigue a significant concern. Understanding the fatigue behavior of welded joints is essential to ensuring the safety and durability of these structures. Most existing research has focused on the fatigue performance of joints created using traditional arc welding techniques, providing a solid foundation of knowledge in this area [1.33], [1.34], [1.35]. These studies have shown that while arc welding can produce strong and reliable joints, it also has limitations, particularly in terms of weld quality and the occurrence of defects that can initiate fatigue cracks. Improvements in welding techniques and post-weld heat treatments have mitigated some of these issues [1.36], but the quest for better performance and efficiency continues. This is where laser-arc hybrid welding comes into play. Despite the promising advantages of laser-arc hybrid welding, research into the fatigue performance of hybrid-welded joints remains limited. This gap

in knowledge is particularly important to address given the application of hybrid welding in steel bridge construction. Investigating the fatigue behavior of hybrid-welded joints made of SBHS materials will provide valuable insights into their suitability for use in critical infrastructure.

(b) Toughness of welded zone

The toughness of the welded zone is crucial for the structural integrity and safety of steel bridges, especially when these joints are subjected to sudden or unpredictable loads. In laser welding, significant hardening occurred in the fusion zone due to rapid heating and cooling [1.37], [1.38], leading to increased brittleness. Hybrid welding reduces temperature gradients compared to laser-only welding. This reduction potentially mitigates the severity of hardening. However, even with less severe gradients, the risk of hardening remains. Any hardening can still compromise the mechanical properties of the welded joints, making them vulnerable to failure under operational stresses. Although SBHS materials are specifically designed for bridge applications and offer high performance in toughness, it is critical to understand how hybrid welding affects the toughness in the fusion zones and heat-affected zones of welded joints made of SBHS. This poses significant concerns for bridge durability and safety, necessitating thorough investigation.

Charpy absorbed energy is a crucial indicator for evaluating the toughness of materials, including welded joints [1.39]. The Charpy impact test measures the amount of energy absorbed by a material during fracture, which is indicative of its ability to withstand sudden impacts or loads without breaking. The test helps distinguish between brittle and ductile materials. Brittle materials absorb less energy and tend to fracture suddenly without significant deformation, while ductile materials absorb more energy and exhibit significant deformation before fracturing. This

distinction is crucial for assessing the performance of welded joints under sudden or unpredictable loads.

(c) Load-carrying Capacity

The load-carrying capacity of welded members is a critical factor in the design and construction of steel bridges. These structures must withstand a variety of loads, including dead loads, live loads, and environmental forces such as wind and seismic activity. The welded members in these bridges play a crucial role in bearing the loads transmitted from the bridge deck and distributing them to the foundation. Any weakness in these members, particularly at the welded joints, can significantly affect the overall stability of the structure. Numerous investigations have been conducted on the load-carrying capacity of arc-welded members [1.40], [1.41], [1.42], [1.43], [1.44]. However, there are few studies on the load-carrying capacity of hybrid-welded members. This gap in research highlights the need for comprehensive studies to evaluate the performance of hybrid-welded members, considering their unique characteristics and potential advantages over traditional welding methods. Understanding the behavior of hybrid-welded members under various loading conditions is essential for optimizing bridge design and ensuring long-term structural integrity and safety.

1.2 Research Objective

This study aims to expand the application of hybrid welding in the manufacturing of steel bridge components by verifying its effectiveness and investigating the performance of hybrid-welded joints made of SBHS. The joining method employed is laser-arc hybrid welding technology, which has garnered significant attention in recent years. The selected steel material is high-performance steel (SBHS), recently developed and anticipated for extensive use in steel bridge structural components. This research will explore the welding conditions necessary to achieve single-pass full penetration welding for thick SBHS plates using hybrid welding technology and assess its applicability in manufacturing steel bridge structural components. Additionally, experiments will be conducted using both hybrid welding and arc welding to produce butt joints, and thermal elastic-plastic analysis models will be developed to replicate these experiments. A series of experiments and analytical results will verify the effectiveness of hybrid welding in the manufacturing of steel bridge components.

Furthermore, the performance of hybrid-welded joints will be investigated from various perspectives, including fatigue performance, toughness, and compressive load-carrying capacity. For comparative analysis, arc-welded joints will also be evaluated from the same perspectives. The ultimate goal is to expand the application of hybrid welding in steel bridge components, thereby providing new welding process options and technological advancements to the bridge construction industry.

1.3 Structure of the Dissertation

This dissertation is structured into six chapters:

Chapter 1 describes the research background and objectives of the research.

Chapter 2 conducts weld cracking experiments using hybrid welding and explores the welding conditions for achieving full penetration welding for 15 mm thick SBHS plates by varying the welding parameters. Employing the established welding conditions, butt welding experiments are performed to obtain sound hybrid-welded and arc-welded joints.

Chapter 3 evaluates the out-of-plane deformation and residual stress of hybrid-welded and arc-welded joints fabricated in Chapter 2. These experiments are further simulated using thermal elastic-plastic analysis to provide a comprehensive understanding of the deformation and residual stress in hybrid-welded butt joints. Two hypotheses are derived: the first posits that the fatigue performance of hybrid-welded joints may surpass that of arc-welded joints, and the second suggests that the load-carrying capacity of hybrid-welded joints could be superior to that of arc-welded joints. Additionally, a concern is raised that the toughness of hybrid-welded joints may not meet the requirements specified by the standards.

Chapter 4 examines the fatigue characteristics of hybrid-welded joints by comparing them with butt joints using arc welding, thus validating one of the hypotheses. Additionally, this chapter addresses the concern regarding toughness by discussing the toughness of hybrid-welded SBHS joints based on Charpy impact tests.

Chapter 5 conducts monotonic compressive loading experiments to evaluate the load-carrying capacities of both hybrid-welded and arc-welded columns, thereby validating the other hypothesis.

Chapter 6 summarizes the findings of the study and outlines future work.

Reference

[1.1] Fatemeh Bodaghi, Mojtaba Movahedi, Suck-Joo Na, Lin-Jie Zhang, Amir Hossein Kokabi (2024) Effect of welding current and speed on solidification cracking susceptibility in gas tungsten arc fillet welding of dissimilar aluminum alloys: Coupling a weld simulation and a cracking criterion. Journal of Materials Research and Technology 30: 4777-4785. https://doi.org/10.1016/j.jmrt.2024.04.195

[1.2] Katayama Seiji, Kawahito Yousuke, Mizutani Masami. (2012) Latest progress in performance and understanding of laser welding. Phys Procedia 39:8–16. https://doi.org/10.1016/j.phpro.2012.10.008

[1.3] Xiangzhong Jin. (2008) A three-dimensional model of multiple reflections for high-speed deep penetration laser welding based on an actual keyhole. Optics and Lasers in Engineering 46 (1): 83-93. https://doi.org/10.1016/j.optlaseng.2007.05.009

[1.4] J. Yan, M. Gao, X. Zeng. (2010) Study on microstructure and mechanical properties of 304 stainless steel joints by TIG, laser and laser-TIG hybrid welding. Opt Laser Eng, 48 (4): 512-517. https://10.1016/j.optlaseng.2009.08.009

[1.5] Hirohata, M., Chen, G., Morioka, K. et al. (2022) An investigation on laser-arc hybrid welding of one-pass full-penetration butt-joints for steel bridge members. Weld World 66: 515–527. https://doi.org/10.1007/s40194-021-01221-0

[1.6] Mori K., Tarui T., Hasegawa T., Yoshikawa N. (2010) Remote laser welding application for car body. Weld Int 24(10):758–763. https://doi.org/10.1080/09507111003655283

[1.7] P.I. Oliveira, F.V. Antunes, A. Loureiro, J.M. Costa. (2019) Effect of the angular misalignment of laser welded T-joints on fatigue curves. International Journal of Fatigue 128,105180. https://doi.org/10.1016/j.ijfatigue.2019.06.040

[1.8] S. Jallouf, K. Casavola, C. Pappalettere, G. Pluvinage. (2016) Assessment of undercut defect in a laser welded plate made of Ti–6Al–4V titanium alloy with probabilistic domain failure assessment diagram. Engineering Failure Analysis 59: 17-27. https://doi.org/10.1016/j.engfailanal.2015.11.018

[1.9] Mingjun Zhang, Zheng Zhang, Kun Tang, Cong Mao, Yongle Hu, Genyu Chen. (2018) Analysis of mechanisms of underfill in full penetration laser welding of thick stainless steel with

a 10kW fiber laser. Optics & Laser Technology 98: 97-105. https://doi.org/10.1016/j.optlastec.2017.07.037

[1.10] Yiyang Hu, Xiong Zhang, Zehui Liu, Fei Yan, Shenli Su, Chunming Wang. (2024) Investigation on the formation mechanism of collapse defects, microstructural evolution and mechanical properties in full penetration laser welding of thick-section steel. Journal of Manufacturing Processes 118: 341-356. https://doi.org/10.1016/j.jmapro.2024.03.060

[1.11] Katayama S., Kawahito Y., Mizutani M. (2010) Elucidation of laser welding phenomena and factors affecting weld penetration and welding defects. Phys Procedia B 5:9–17. https://doi.org/10.1016/j.phpro.2010.08.024

[1.12] Jiang Meng, Chen Xi, Chen Yanbin, Tao Wang. (2020) Mitigation of porosity defects in fiber laser welding under low vacuum. J Mater Process Technol 276:116385. https://doi.org/10.1016/j.jmatprotec.2019.116385

[1.13] Fujii Hidetoshi, Umakoshi Hideaki, Aoki Yasuhiro, Nogi Kiyoshi. (2004) Bubble formation in aluminum alloy during electron beam welding. J Mater Process Technol 155:1252–1255. https://doi.org/10.1016/j.jmatprotec.2004.04.141

[1.14] Kutsuna M, Yan C. (1998) Study on porosity formation in laser welds in aluminum alloys (Report 1): effects of hydrogen and alloying elements. Weld Int 12:937–949. https://doi.org/10.1080/0950711980944

[1.15] E. Anusha, Adepu Kumar, S.M. Shariff. (2020) A novel method of laser surface hardening treatment inducing different thermal processing condition for Thin-sectioned 100Cr6 steel. Optics & Laser Technology 125:106061. https://doi.org/10.1016/j.optlastec.2020.106061

[1.16] Kaplan, A. (2017) Metallurgy and Imperfections of Welding and Hardening. In: Dowden, J., Schulz, W. (eds) The Theory of Laser Materials Processing. Springer Series in Materials Science, vol 119. Springer, Cham. https://doi.org/10.1007/978-3-319-56711-2_8

[1.17] Zhi Tian, Shuangjian Chen, Yanjun Wang, Wu Tao, Xiangxi Ye, Wenjie Ren, Shanglu Yang. (2023) Dynamic laser welding hot cracking behavior and mechanism of new structural material Ni–28W–6Cr alloy for molten salt reactor. Journal of Materials Research and Technology 25: 3022-3036. https://doi.org/10.1016/j.jmrt.2023.06.170

[1.18] Jin Wang, Hui-Ping Wang, Xiaojie Wang, Haichao Cui, Fenggui Lu. (2015) Statistical analysis of process parameters to eliminate hot cracking of fiber laser welded aluminum alloy. Optics & Laser Technology 66:15-21. https://doi.org/10.1016/j.optlastec.2014.08.009

[1.19] Reutzel EW, Sullivan MJ, Mikesic DA. (2006) Joining pipe with the hybrid laser-GMAW process: weld test results and cost analysis. Weld J 85:66–71.

[1.20] Olschok S, Reisgen U, Dilthey U. (2007) Robot application for laser-GMA hybrid welding in shipbuilding, In: Proc. of the Laser Materials Processing Conference ICALEO 2007, Orlando, USA, pp 308–315. https://doi.org/10.2351/1.5061084

[1.21] Walz C, Springer IS, El Rayes M, Seefeld T, Sepold G. (2001) Hybrid welding of steel for offshore applications, In: ISOPE International Ocean and Polar Engineering Conference, p. ISOPE-I-01-380.

[1.22] Staufer H (2006) Laser hybrid welding and laser brazing at Audi and VW. Weld World 50:44–50. https://doi.org/10.1007/BF03266535

[1.23] Coutouly JF, Deprez P, Demonchaux J, Kouruk AI. (2006) The optimization of laser welding and MIG/MAG-laser hybrid welding of thick steel sheets. Laser Eng 16:399–411

[1.24] Kah P, Salminen A, Martikainen J. (2011) The influence of parameters of penetration, speed and bridging in laser hybrid welding. Mechanika 17(3):324–333. DOI:10.5755/j01.mech.17.3.511

[1.25] Bunaziv I, Akselen OM, Frostevarg J, Kaplan AFH. (2018) Deep penetration fiber laser-arc hybrid welding of thick HSLA steel. J Mater Process Technol 256:216–228. https://doi.org/10.1016/j.jmatprotec.2018.02.026

[1.26] Gook, S., Gumenyuk, A., & Rethmeier, M. (2010) Weld seam formation and mechanical properties of girth welds performed with laser-GMA-hybrid process on pipes of grade X65. In International Congress on Applications of Lasers & Electro-Optics (Vol. 2010, No. 1, pp. 62–69). Laser Institute of America. https://doi.org/10.2351/1.5062091

[1.27] Üstündag Ö, Fritzsche A, Avilov V et al. (2018) Study of gap and misalignment tolerances at hybrid laser arc welding of thick-walled steel with electromagnetic weld pool support system. Procedia CIRP 74:757–760. https://doi.org/10.1016/j.procir.2018.08.016

[1.28] Chen, G., Hirohata, M., Hyoma, K. et al. (2024) Deformation and residual stress of T-shaped joints fabricated by laser-arc hybrid welding for steel bridge members. Weld World 68: 459–473. https://doi.org/10.1007/s40194-023-01650-z

[1.29] Inose, K, Owaki, K, Kanbayashi, J, and Nakanishi, Y. (2012) Functional Assessment of Laser Arc Hybrid Welded Joints and Their Application for Bridge Construction. Welding in the World 56: 118-124. https://doi.org/10.1007/BF03321371

[1.30] Inose, K., Kanbayashi, J., Abe, D. et al. (2013) Design and welding method for high-strength steel structure using laser-arc hybrid welding. Weld World 57: 657–664. https://doi.org/10.1007/s40194-013-0064-0

[1.31] Barker, M. G., & Schrage, S. D. (2000) High-Performance Steel Bridge Design and Cost Comparisons. Transportation Research Record. 1740(1):33-39. https://doi.org/10.3141/1740-05

[1.32] Koji Homma. (2015) Newly Developed Bridge High-performance Steel and its Application to Tokyo Gate Bridge. IABSE Symposium Report 104(25):1-6. DOI:10.2749/222137815815774403

[1.33] Xu Jiang, Daqian Cao, Xuhong Qiang, Chunli Xu. (2024) Study on fatigue performance of steel bridge welded joints considering initial defects. Journal of Constructional Steel Research 212: 108309. https://doi.org/10.1016/j.jcsr.2023.108309

[1.34] Ernian Zhao, Hang Yin, Jinhui Liu, Xin Zhang. (2023) Experimental and comparative investigation on fatigue performance of three typical welded joints of Q370qNH bridge weathering steel. Case Studies in Construction Materials 19: e02630. https://doi.org/10.1016/j.cscm.2023.e02630

[1.35] Han Su, Jian Wang, Jinsheng Du. (2020) Fatigue behavior of corroded non-load-carrying bridge weathering steel Q345qDNH fillet welded joints. Structures 26: 859-869. https://doi.org/10.1016/j.istruc.2020.05.019

[1.36] Hirohata, M., Chang, K., Suzuki, T., Konishi, H. (2024) Local heating for reducing residual stress and fatigue-performance improvement of welded joints. Journal of Constructional Steel Research 215:108544. https://doi.org/10.1016/j.jcsr.2024.108544

[1.37] Farabi, N., Chen, D.L. & Zhou, Y. (2012) Tensile Properties and Work Hardening Behavior of Laser-Welded Dual-Phase Steel Joints. J. of Materi Eng and Perform 21: 222–230. https://doi.org/10.1007/s11665-011-9865-8

[1.38] Bunaziv, I., Dørum, C., Nielsen, S.E. et al. (2021) Root formation and metallurgical challenges in laser beam and laser-arc hybrid welding of thick structural steel. Int J Adv Manuf Technol 116: 561–578. https://doi.org/10.1007/s00170-021-07453-0

[1.39] Inose, K., Yamaoka, H., Nakanishi, Y. et al. (2017) Toughness assessments of laser arc-hybrid welds of ultra high strength steel. Weld World 61: 955–961. https://doi.org/10.1007/s40194-017-0483-4

[1.40] Zhongwei Zhao, Wuyang Wang, Xiangyang Jian, Shengjie Mo. (2024) Experimental investigations on the compression capacity of rectangular steel tubular columns strengthened with intermittently welded angle steel. Journal of Constructional Steel Research 212: 108272. https://doi.org/10.1016/j.jcsr.2023.108272

[1.41] Xianlei Cao, Yunxu Chen, Wenjuan Wang, Zhengqiang Tao, Pei Wang, Zhengyi Kong, Yu jie Zhang. (2023) Local buckling of high strength steel welded cruciform-section columns under axial compression. Structures 56: 104941. https://doi.org/10.1016/j.istruc.2023.104941

[1.42] Bo Yang, Le Shen, Shao-Bo Kang, Mohamed Elchalakani, Shi-Dong Nie. (2018) Load bearing capacity of welded Q460GJ steel H-columns under eccentric compression. Journal of Constructional Steel Research 143: 320-330. https://doi.org/10.1016/j.jcsr.2018.01.011

[1.43] Fei Yin, Lu Yang. (2024) Minor-axis flexural buckling of Q1100 ultra high strength steel welded I-section columns. Thin-Walled Structures 197: 111644. https://doi.org/10.1016/j.tws.2024.111644

[1.44] Xianlei Cao, Yunxu Chen, Hangfei Wang, Chao Cheng, Xuejun Zhou, Haitang Zhang, Seung-Eock Kim, Zhengyi Kong. (2023) Experimental and numerical investigation of 800 MPa HSS welded T-section column strengthened with CFRP. Thin-Walled Structures 184: 110510. https://doi.org/10.1016/j.tws.2022.110510

Chapter 2 Exploring Hybrid Welding Conditions and Fabricating Hybrid-welded Joints

2.1 Introduction

To validate the effectiveness of hybrid welding in the manufacture of steel bridge components, it is imperative to establish the hybrid welding conditions for the thick steel plates used in steel bridge structures. Accordingly, this chapter aims to identify the hybrid welding parameters for 15 mm thick steel plates by conducting weld cracking experiments and subsequently employing the established welding parameters to fabricate one-pass full penetration hybrid-welded butt joints with SBHS. Comparisons are made between butt joints fabricated using both hybrid welding and conventional arc welding techniques, from the viewpoints of welding time and energy consumption.

2.2 Exploring Hybrid Welding Conditions

2.2.1 Weld Cracking Experimental Specimens

Figure 2.1 illustrates the geometry and size of test samples. The geometric shape of the test specimens referred to the shape of weld cracking experimental specimens with the y-shaped groove specified in JIS Z 3158 [2.1]. The test specimens measured 200 mm in length, 145 mm in width, and 15 mm in thickness. An 80 mm long and 0.2 mm wide slit was provided at the center of the specimens using electrical discharge machining.

The test samples were made of SBHS400. Table 2.1 provides the chemical composition and mechanical properties (mill sheet values) of the test steel material used.

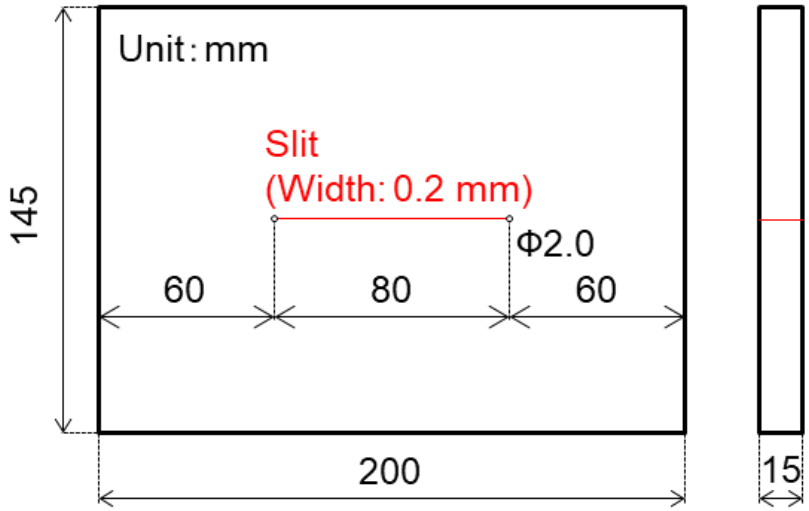

Figure 2.1 Geometry and size of experimental specimens

Table 2.1 Chemical composition and mechanical properties of the steel material and filler wire

Material	Chemical compositions [mass%]								Yield strength [N/mm²]	Tensile strength [N/mm²]	Elon-gation [%]
	C	Si	Mn	P	S	Ni	Cr	Fe			
SBHS400	0.11	0.29	1.36	0.009	0.001	0.01	0.02	bal	503	567	22
G49AP3M16	0.11	0.74	1.36	0.006	0.017	—	—	bal	450	573	27

2.2.2 Experimental Setup

Hybrid welding integrates MIG arc welding with fiber laser welding. A digital pulse welding power source from DAIHEN Corporation (model: DP350) was employed for the arc welding. The welding wire, G49AP3M16, specified in JIS Z 3312 [2.2] and produced by Kobe Steel Corporation, had a diameter of 1.2 mm. Table 2.1 presents the chemical composition and mechanical properties of the welding wire. The shielding gas, comprising Ar+5% O_2, was delivered at a flow rate of 20 L/min. For the laser oscillator, a fiber laser from IPG Photonics Corporation (model: YLR-20000) with a maximum output of 20 kW was employed. Key laser parameters included a focal length of 250 mm, a laser spot diameter of 600 μm, and a focal offset distance of -5 mm. Figure 2.2 illustrates the experimental setup for hybrid welding,

highlighting the strategic placement of heat sources: an arc heat source followed by the laser, spaced 3 mm apart. The arc torch was angled at 30°, and the laser head was inclined at 5° relative to the vertical.

Table 2.2 provides the specific conditions for hybrid welding. The arc current and voltage were maintained constant, while the laser output and welding speed were varied to determine the welding conditions for achieving full penetration in a single pass.

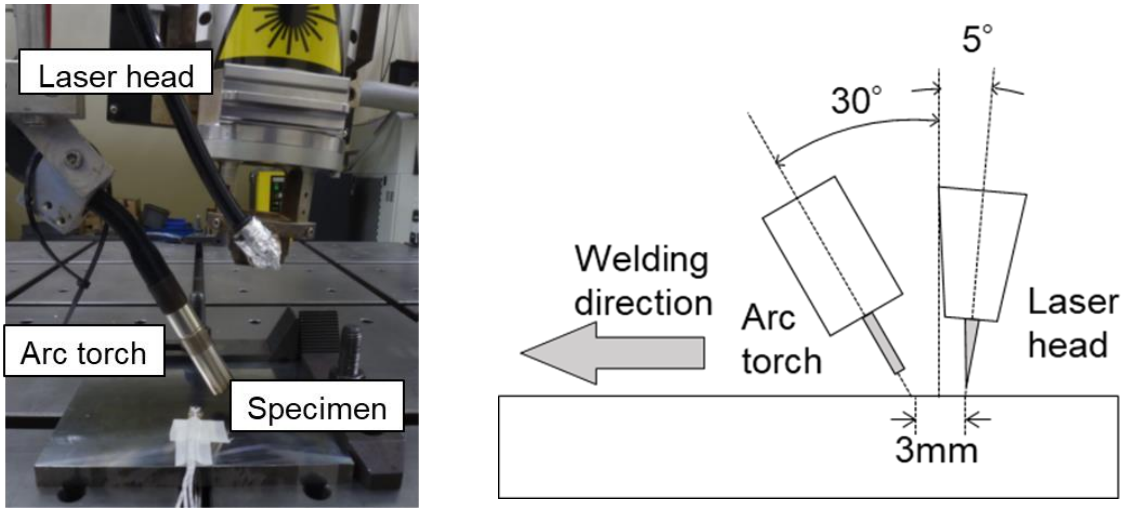

(a) Appearance of hybrid welding (b) Arrangement and angles of heat sources

Figure 2.2 Experimental setup for hybrid welding

Table 2.2 Hybrid welding conditions

Welding condition	Laser power [kW]	Welding speed [m/min]	Arc current [A]	Arc voltage [V]	Number of specimens
1	13.1	1.4	250	28	2
2	13.1	1.6	250	28	2
3	13.1	1.8	250	28	2
4	15.3	1.6	250	28	1
5	12.5	1.6	250	28	1

2.2.3 Experimental Results

Figure 2.3 demonstrates cross-sectional macroscopic photographs of welds taken under the tested welding conditions 1 to 5, as specified in Table 2.2. In an attempt to investigate welding conditions conducive to achieving single-pass full penetration, the welding speeds were initially adjusted for welding conditions 1 to 3, maintaining all other welding parameters constant. As a result, underfill was observed in welding condition 1 at a welding speed of 1.4 m/min, and significant melt-off was induced in welding condition 3 at a welding speed of 1.8 m/min. However, an overall satisfactory bead shape was achieved in welding condition 2 at a welding speed of 1.6 m/min. Subsequently, in pursuit of achieving satisfactory weld seams, adjustments were made to the laser power based on welding condition 2, leading to welding conditions 4 and 5. In welding condition 4, the excess weld metal on the laser-irradiated surface was slightly reduced. On the other hand, the weld seam was smooth on the front and back surfaces of the welded joint in welding condition 5. Ultimately, it was determined that welding condition 5 was the optimal solution for hybrid welding, with a laser power of 12.5 kW, an arc current of 250 A, an arc voltage of 28 V, and a welding speed of 1.6 m/min.

Condition	No. 1	No. 2	No. 3	No. 4	No. 5
Laser power [kW]	13.1	13.1	13.1	15.3	12.5
Welding speed [m/min]	1.4	1.6	1.8	1.6	1.6
Macroscopic photograph					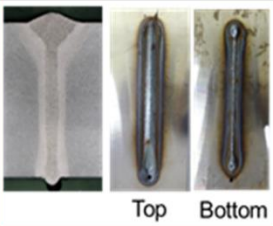 Top Bottom

Figure 2.3 Macroscopic photographs taken under tested welding conditions

2.3 Fabricating Hybrid-welded Butt Joints

In steel bridge construction, butt joints are extensively employed to join deck plates, beams, and columns, thereby ensuring structural integrity and stability. Consequently, butt joints have been selected as a primary subject of this research. Figure 2.4 illustrates the application of butt joints in the joining of deck plates. The thickness of the steel deck plate is generally 12 mm – 16 mm.

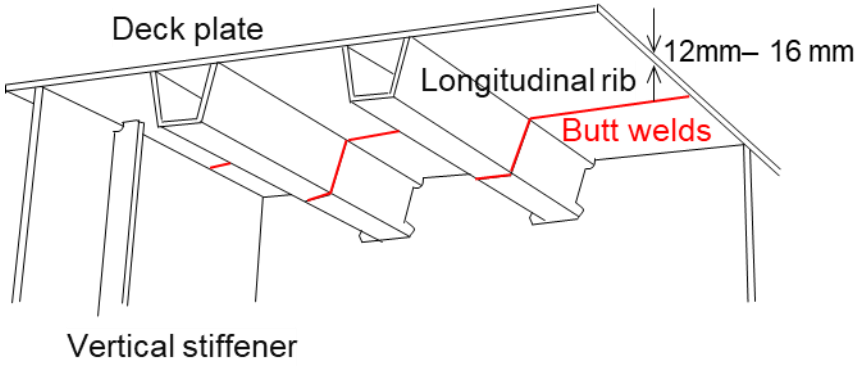

Figure 2.4 Butt joints in steel deck plates

2.3.1 Butt Joint Specimens

Figure 2.5 illustrates the dimensions and groove shape of the butt joint specimens utilized for both hybrid and arc welding processes. The material used was SBHS400, with three prepared in total: two for hybrid welding, labeled as HWBJ-1 and HWBJ-2, and one for arc welding, labeled as AWBJ-1. The base material was 16 mm thick, while the welded portions were milled down to 15 mm thick. To ensure a precise assessment of deformation and residual stress induced by hybrid and arc welding, it was crucial to fabricate the specimens without any misalignment caused by tack welding. Consequently, a single steel plate with a central groove was utilized for welding instead of two steel plates [2.3]. The dimensions of the steel plate were 500 mm in width and 300 mm in length. Additionally, protruding tabs were provided at the start and end of the

weld line, with the length of the weld line set at 340 mm. Figure 2.5 (c) shows a 0.3 mm slit created by electric discharge machining for hybrid welding. Figure 2.5 (d) depicts a V-shaped groove with a 50-degree angle, used in arc welding. The chemical composition and mechanical properties (mill sheet values) of the test steel material have been shown in Table 2.1.

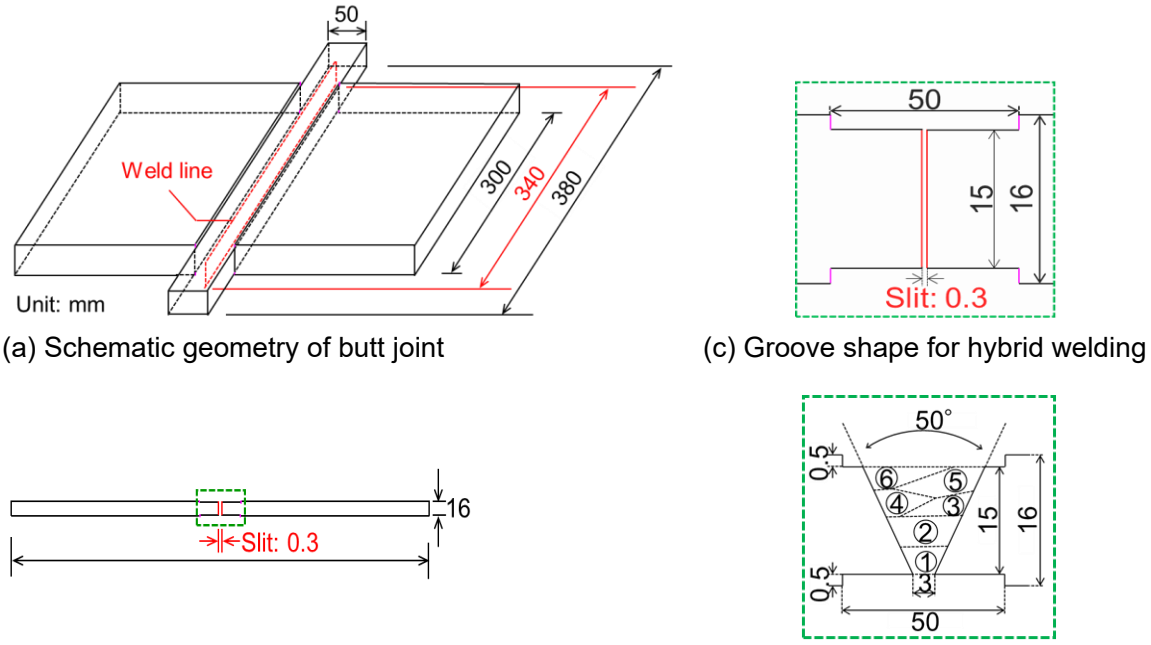

(a) Schematic geometry of butt joint

(c) Groove shape for hybrid welding

(b) Schematic cross-sectional view of butt joint

(d) Groove shape for arc welding

Figure 2.5 Specimen geometry and groove shape

2.3.2 Experimental Setup

As illustrated in Figure. 2.6 (a) and (b), the hybrid welding setup utilized the same equipment as described in Section 2.2.2, including the welding machine, welding wire, shielding gas, and so on. The welding conditions determined in Section 2.2.3 were slightly modified to accommodate the longer weld line (340 mm) compared to the weld line (80 mm) in Section 2.2.1. The longer weld line might result in slit closure during welding, making it challenging to achieve a stable back wave. To avoid this phenomenon, the slit was widened from 0.2 mm to 0.3 mm,

and the laser output was increased. The deformation of hybrid-welded butt joints was not restrained during welding. Table 2.3 presents the welding conditions for hybrid welding.

For arc welding, the technique employed was Gas Metal Arc Welding (GMAW). A digital pulse welding power source from DAIHEN Corporation (model: Welbee P500L) was used for the arc welding power supply. The filler wire, specified as YGW11 by JIS Z 3312 and manufactured by Kobe Steel Corporation, had a diameter of 1.2 mm. The chemical composition and mechanical properties of filler wire are shown in Table 2.4. The shielding gas used was 100% CO_2, with a flow rate maintained at 23 L/min. The backing was a ceramic U-groove, with a protrusion length of 15 mm. The angle of the arc torch was 0 degrees, and the inter-pass temperature was kept below 100°C. The experimental setup is illustrated in Figure 2.6 (c) and (d). The test specimens during welding were unconstrained. Table 2.3 presents the welding conditions for arc welding. In addition, the wire feeding speed was maintained at 5.9 m/min.

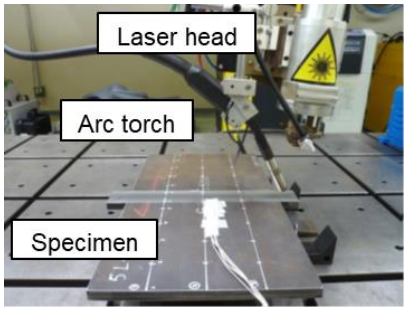

(a) Hybrid welding

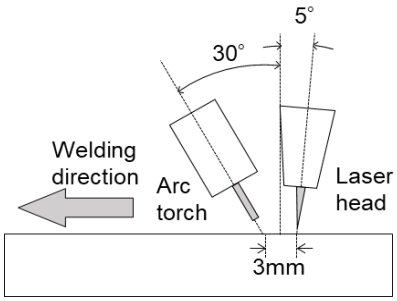

(b) Arrangement and angles of hybrid heat sources

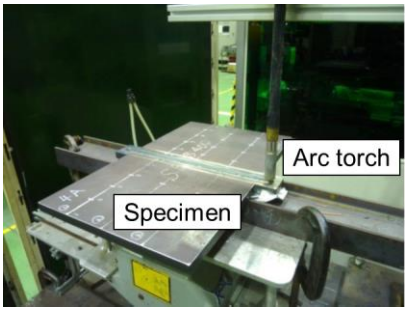

(c) Arc welding

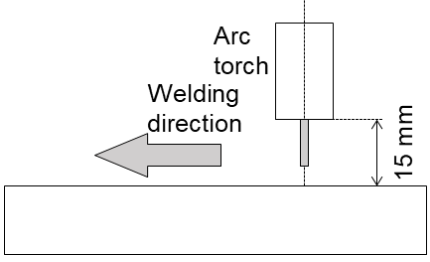

(d) Arrangement and angles of arc heat source

Figure 2.6 Experimental setup for hybrid and arc welding

Table 2.3 Welding conditions for hybrid and arc welding

Welded joint type	Specimen ID-No.	Welding pass	Laser power [kW]	Welding speed [m/min]	Arc current [A]	Arc voltage [V]	Welding time [s]	Heat input [J/mm]		
								Laser	Arc	Total
Hybrid-welded butt joint	HWBJ-1	1	13.01	1.6	255	28.1	12.75	488	269	757
	HWBJ-2	1	13.01	1.6	258	28.1	12.75	488	272	760
Arc-welded butt joint	AWBJ-1	1		0.15	200	27	616.5		2160	9576
		2		0.18	200	27			1800	
		3		0.25	200	26			1248	
		4		0.25	200	26			1248	
		5		0.20	200	26			1560	
		6		0.20	200	26			1560	

Table 2.4 Chemical composition and mechanical properties of filler wire

Material	Chemical composition [mass%]					Yield strength [N/mm²]	Tensile strength [N/mm²]	Elon-gation [%]
	C	Si	Mn	P	S			
YGW11	0.08	0.51	1.10	0.010	0.010	490	570	31

2.3.3 Experimental Results

(a) Welding time

In comparing the welding time between hybrid- and arc-welded butt joints, a pronounced disparity was observed. As delineated in Table 2.3, the hybrid welding technique enabled full penetration of 15 mm thick steel plates with a single pass, completing the task in approximately 12.75 seconds. In stark contrast, conventional arc welding required up to six passes to achieve similar penetration, amassing a total of about 616.5 seconds, excluding the time for inter-pass cooling. Consequently, hybrid welding exhibited a remarkable time efficiency improvement of approximately 98% over conventional arc welding. This substantial reduction in welding time indicates that hybrid welding technology markedly enhances manufacturing efficiency, particularly for joining thick steel plates.

(b) Energy conservation

In the comparative analysis of energy efficiency between hybrid- and arc-welded butt joints, a notable discrepancy in energy consumption was evident. As detailed in Table 2.3, the heat input required for hybrid welding to achieve single-pass full penetration of 15 mm thick steel plates was approximately 760 J/mm. Conversely, the arc welding technique required an approximate heat input of 9580 J/mm to achieve a similar depth of penetration. Therefore, hybrid welding offered an energy savings of approximately 92% over arc welding. This significant reduction in energy consumption aligns with the Sustainable Development Goals, particularly SDGs Goal 9: Industry, Innovation, and Infrastructure. This goal emphasizes sustainable industrialization, which is directly furthered by innovations that reduce energy consumption in manufacturing processes, thereby contributing to resource conservation and reducing the environmental impact of industrial activities.

(c) Macroscopic photograph

Figure 2.7 displays the cross-sectional macroscopic photographs of butt joints fabricated by hybrid welding and arc welding. Hybrid welding was capable of achieving one-pass full-penetration butt joints, whereas arc welding required six passes to fabricate the same dimensional full-penetration joints. In addition, the maximum heights of excessive convexity on the top and bottom surfaces, as measured by a laser displacement meter, were approximately 0.5 mm and 0.6 mm, respectively.

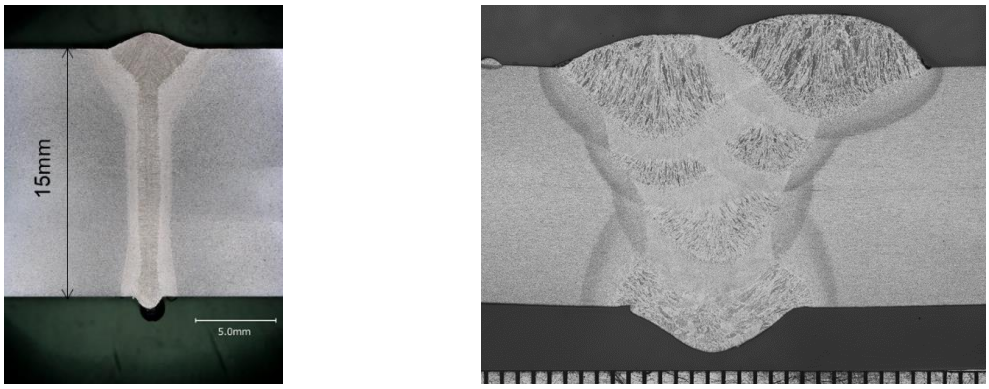

(a) Hybrid-welded butt joint (b) Arc-welded butt joint

Figure 2.7 Macroscopic photographs of the welded part

2.4 Summary

This chapter delved into the investigation of hybrid welding parameters designed to achieve single-pass full penetration on 15 mm thick steel plates from one side. Through a series of weld cracking experiments, optimal welding conditions were identified. Subsequently, using these established parameters, hybrid-welded butt joints were fabricated. The following are the main findings obtained.

(1) Within the scope of this experiment, a sound hybrid-welded butt joint was successfully fabricated under specific conditions: a laser power of 12.5 kW, a welding speed of 1.6 m/min, an arc current of 250 A, and an arc voltage of 28 V.

(2) In terms of time efficiency and energy savings, hybrid welding demonstrated approximately 98% and 92% improvements, respectively, when compared to conventional arc welding.

Reference

[2.1] Japan Standards Association. (2014) JIS Handbook Welding I (Basics), JIS Z 3158, 860-863. (In Japanese)

[2.2] Japanese Standards Association. (2013) Solid wires for MAG and MIG welding of mild steel, high strength steel and low temperature service steel. JIS Z 3312.

[2.3] Lee, J.-Y., Kim, Y.-C., and Inose, K. (2010) Verification of Validity and Generality of Dominant Factors in High Accurate Prediction of Welding Distortion. Welding in the World 54: 279-285. https://doi.org/10.1007/BF03266740

Chapter 3 Characteristics of Welding Deformation and Residual Stress in Hybrid-welded Butt Joints

3.1 Introduction

In examining the effectiveness of hybrid welding in the fabrication of steel bridge components, this chapter focuses on the out-of-plane deformation and residual stresses in welded joints. The welded steel structures inevitably undergo deformation, necessitating correction procedures that entail both time and monetary expenses. Therefore, it is desirable to minimize welding deformation.

Residual stresses, both along and perpendicular to the weld line directions, critically impact the structural performance. Residual stress along the weld line direction can compromise the load-carrying capacity of welded steel structures. Residual stress perpendicular to the weld line direction can adversely affect fatigue performance. This necessitates post-weld treatments such as heat treatment, peening, and overloading to mitigate residual stress [3.1].

A detailed analysis of the residual stress distribution is essential for ensuring structural integrity and longevity. This analysis uses hybrid-welded joints fabricated as described in Chapter 2 to measure out-of-plane deformation and residual stresses. Furthermore, numerical simulations are performed using thermal elastic-plastic analysis to further understand these phenomena. By comparing conventional arc welding with hybrid welding, this study aims to validate the superiority of hybrid welding in the production of steel bridge components from the viewpoints of welding deformation and residual stress.

3.2 Butt Welding Experiments

3.2.1 Experimental Specimens

The experimental specimens utilized in this chapter consisted of two hybrid-welded specimens (HWBJ-1 and HWBJ-2) and one arc-welded specimen (AWBJ-1), as described in Section 2.3.2.

3.2.2 Experimental Methods

In Section 2.3.2, thermocouples were attached to the specimens prior to the fabrication of hybrid-welded butt joints, aiming to record temperature histories throughout the process. The locations of the thermocouples, as detailed in Figure 3.1, were positioned 10 mm from the centerline (depicted as a light blue dotted line, x = -10 mm). Specifically, four thermocouples were mounted on the surface at positions: y = -15, -30, -50, and -80 mm.

Following the welding process, the out-of-plane deformation was measured using a digital depth gauge along three measurement lines at x = -75, 0, and 75 mm. Additionally, residual stresses— both parallel and perpendicular to the weld line— were measured using the X-ray diffraction method near the weld line at positions x = -20 mm, and y = -20, -15, -10, -5, 5, 10, 15, 20 mm. To mitigate the potential impact of surface finishing on the measurements, electrolytic polishing was performed to a depth of approximately 200 μm from the surface at the residual stress measurement points, as illustrated in Figure 3.2.

For arc welding, the methodologies utilized to measure temperature histories, out-of-plane deformation, and residual stresses were consistent with those employed in hybrid welding, ensuring comparability between the two welding processes.

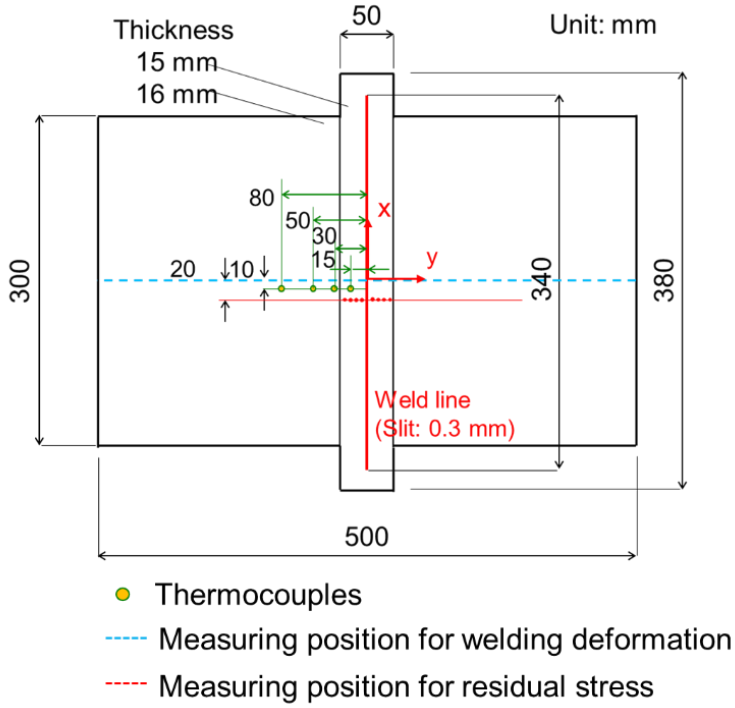

Figure 3.1 Hybrid-welded specimen for temperature histories, deformation, and residual stress

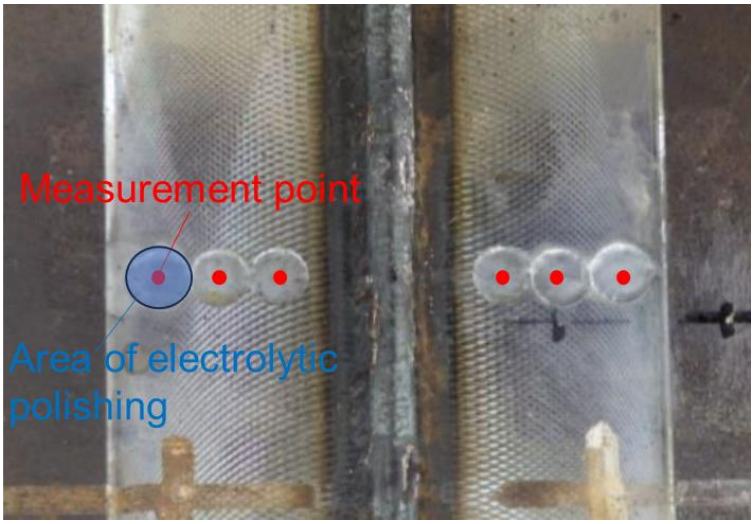

Figure 3.2 Area of electrolytic polishing

3.2.3 Experimental Results

(a) Temperature histories

Figures 3.3 and 3.4 illustrate the temperature histories recorded for both hybrid-welded and arc-welded butt joints. Notably, the temperature data for the first and second passes were not captured in the case of arc welding. These temperature measurements are critical and will be employed to validate the thermal elastic-plastic analysis model, as discussed later in Section 3.3.3 (a).

(b) Welding deformation

Figure 3.5 illustrates the angular distortion measured in hybrid- and arc-welded butt joints. The initial geometry of each specimen was meticulously documented prior to welding. The angular distortion resulting from the welding process was then quantified by subtracting these initial measurements from the values obtained post-welding. Measurements from -50 mm to 50 mm were unattainable due to the interference from the weld bead, leading to the necessity of predicting the value at y = 0 mm through linear interpolation from adjacent measurements.

The angular distortion observed in both hybrid- and arc-welded butt joints presented a V-shaped pattern. Specifically, the hybrid-welded butt joints, HWBJ-1 and HWBJ-2, exhibited relatively minor distortions of 0.56 mm and 0.44 mm, respectively. In stark contrast, the arc-welded butt joint, AWBJ-1, displayed a more pronounced angular distortion of 10.95 mm. This marked variation in angular distortion could be primarily attributed to the substantial differences in heat input between the two welding methods: hybrid welding utilized an input of 760 J/mm, compared to 9576 J/mm for arc welding, as detailed in Table 2.3. Regarding longitudinal bending deformation, the small variations in measurements at lines of x = -75, 0, and 75 mm suggest that the longitudinal bending deformation from both welding methods was minimal.

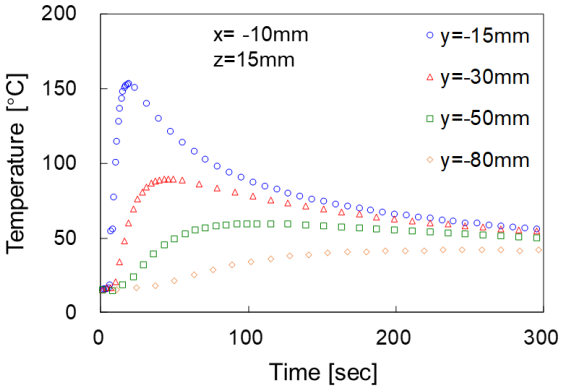

(a) HWBJ-1

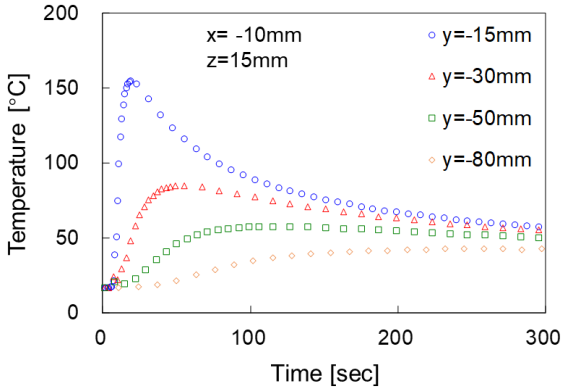

(b) HWBJ-2

Figure 3.3 Temperature histories for hybrid welding

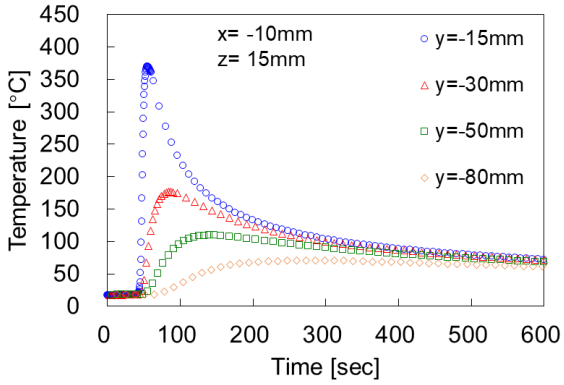

(a) Pass 3

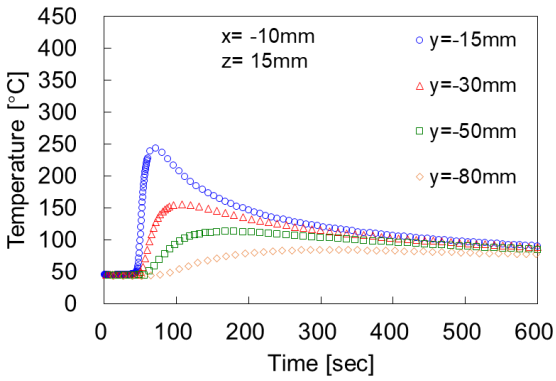

(b) Pass 4

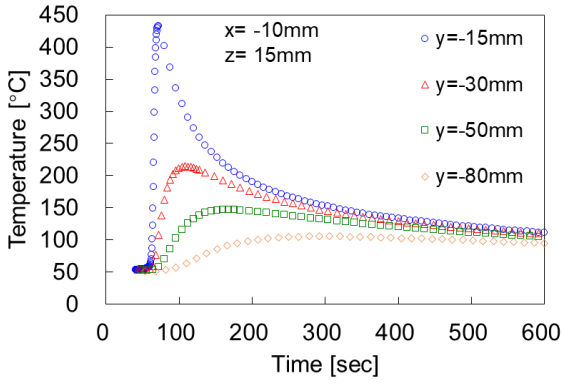

(c) Pass 5

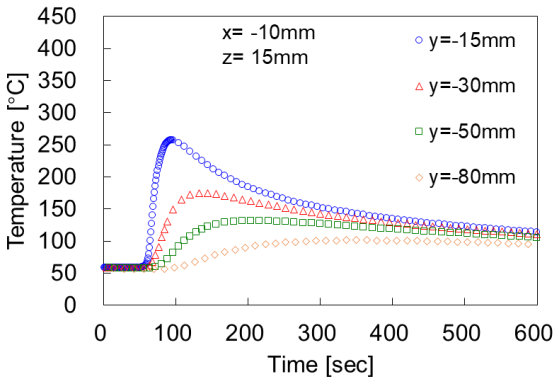

(d) Pass 6

Figure 3.4 Temperature histories for arc welding

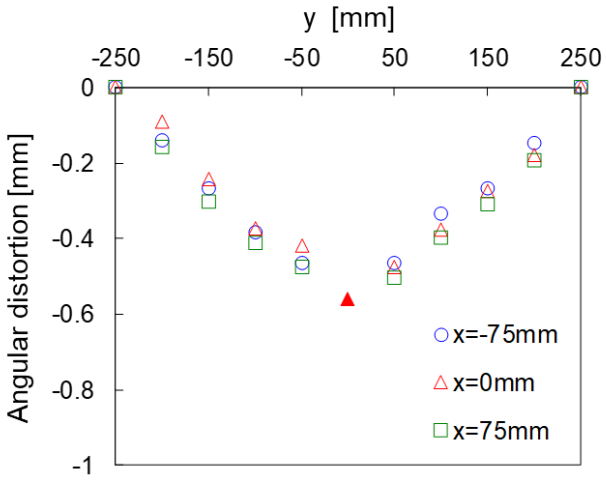

(a) HWBJ-1

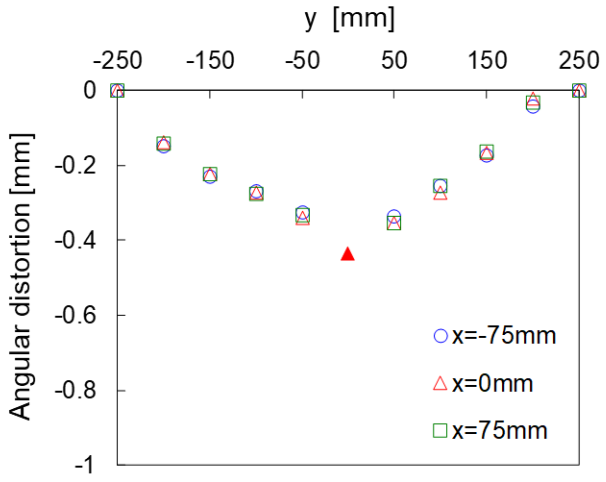

(b) HWBJ-2

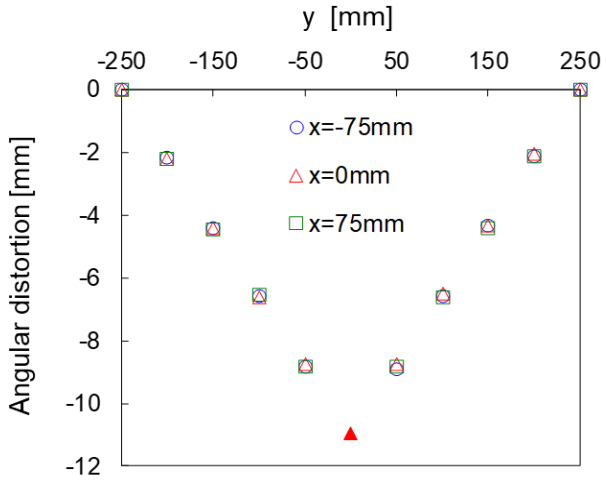

(c) AWBJ-1

Figure 3.5 Angular distortion for hybrid- and arc-welded butt joints

(c) Residual stress

Figure 3.6 presents the average values and standard deviations of the residual stresses measured in both parallel and perpendicular directions to the weld line for hybrid welding. Measurements were obtained from specimen HWBJ-1 at locations y = -20, -15, -10, 10, 15, 20 mm, and from specimen HWBJ-2 at positions y = -10, -5, 5, 10 mm. A comparative analysis between the measurements at locations y = -10 and 10 mm for both specimens HWBJ-1 and HWBJ-2 revealed no significant differences in residual stress. Consequently, the residual stress data for HWBJ-1 and HWBJ-2 were combined for further analysis.

In the direction parallel to the weld line, tensile residual stresses were observed within approximately 25 mm of the weld center (-12.5 mm < y < 12.5 mm), peaking at 341 N/mm². Beyond this zone (y < -12.5 mm and y > 12.5 mm), compressive residual stresses were observed, with the maximum being -47 N/mm². Perpendicular to the weld line, the maximum tensile residual stress recorded was 174 N/mm², with stresses diminishing toward zero as the distance from the weld line increased.

Figure 3.7 illustrates the residual stresses measured for arc welding in both parallel and perpendicular directions to the weld line. In the parallel direction, all measured residual stresses were tensile, with a maximum of 415 N/mm². In the perpendicular direction, the peak tensile stress was 296 N/mm².

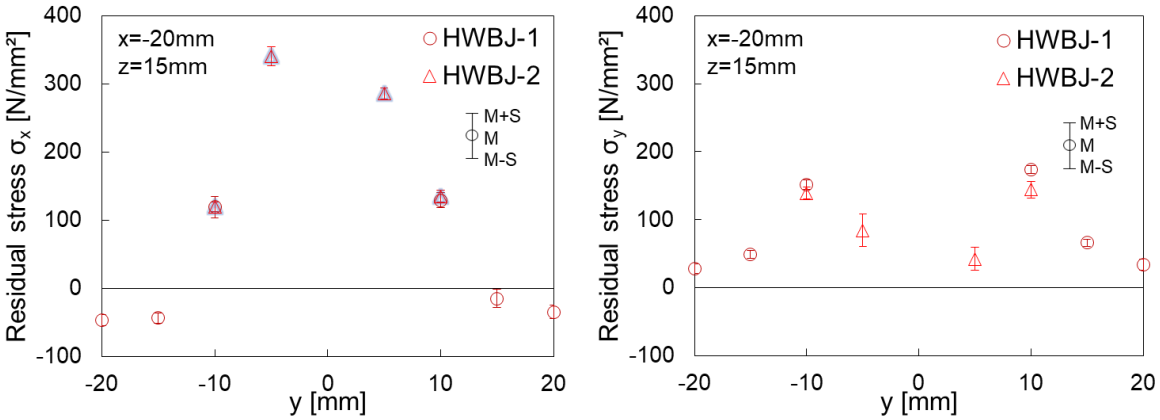

(a) Stress component in the weld line direction

(b) Stress component in cross direction

Figure 3.6 Residual stresses caused by hybrid welding

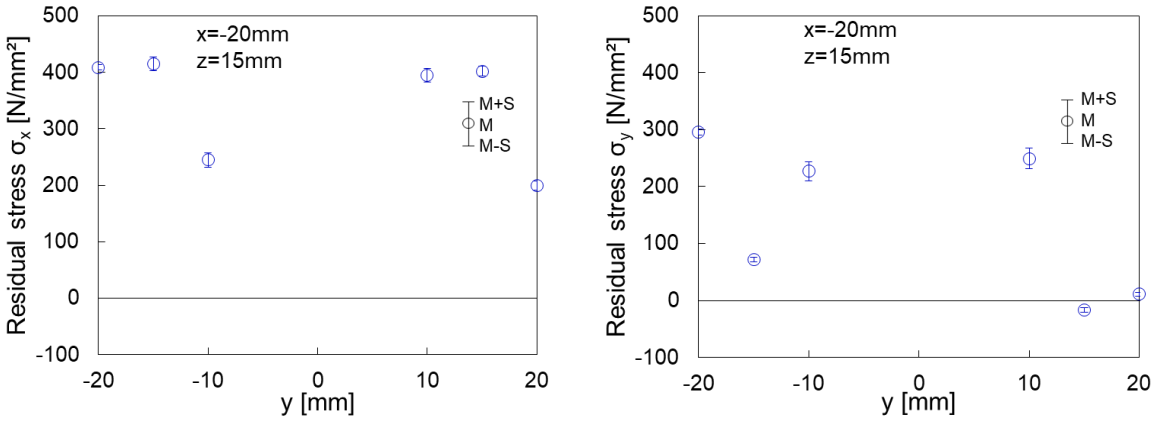

(a) Stress component in the weld line direction

(a) Stress component in cross direction

Figure 3.7 Residual stresses caused by arc welding

3.3 Thermal Elastic-Plastic Analysis

In this section, to reproduce the hybrid and arc welding experiments conducted in Section 2.3.2, fully-coupled thermal elastic-plastic welding models are developed using the finite element method. The validity of the models is assessed by comparing the experimental results with the analytical outcomes. This comparative analysis substantiates that the models accurately replicate the physical and mechanical behaviors observed during the welding processes, thereby affirming their reliability for further analyses in welding studies.

3.3.1 Investigation of the Mechanical Properties of Weld Metal

In hybrid welding, the accelerated cooling rate necessitated consideration of hardening in the weld metal. Hence, based on prior research [3.2] [3.3], this study quantified the Vickers hardness of hybrid weld seams and used the ratio of average Vickers hardness between the weld metal and the base material to establish the mechanical properties of the weld metal.

Figure 3.8 illustrates the locations where the Vickers hardness measurements were taken for HWBJ-1. The test force applied was 0.98 N. Hardness measurements for hybrid-welded joints were conducted along lines ① and ② (refer to Figure 3.8). These measurements covered points subjected to the combined heat input from both laser and arc welding (at z=14 mm on line ①), and areas affected solely by laser heat (at z=7.5 mm on line ②). Each line consisted of 50 points spaced 0.2 mm apart, extending from the center of the weld metal through the heat-affected zone on both sides to the base material. Results revealed a hardness ratio of approximately 1:1.5 between the base material and the weld metal. Consequently, in the simulation model (as detailed later in Section 3.3.2), the yield stress and tensile strength of the weld metal were set to 1.5 times as high as those of the base material.

Figure 3.9 presents the results of the Vickers hardness measurements performed on the arc-welded joint. The test force was maintained at 0.98 N, consistent with that used in hybrid welding. Measurements were taken along lines ①, ②, and ③ (see Figure 3.9). The measurement points on the lines from ① to ③ comprised 50 points, spaced 0.4 mm apart, centered on the weld metal, extending through the heat-affected zone on both sides and reaching down to the base metal. The Vickers hardness of the weld metal was found to be equivalent to that of the base material across all measured locations. Consequently, for this analysis, the yield stress and tensile strength of the weld metal were not adjusted based on the

average Vickers hardness ratio; instead, values derived directly from the welding wire specifications, as detailed in Table 2.4, were utilized.

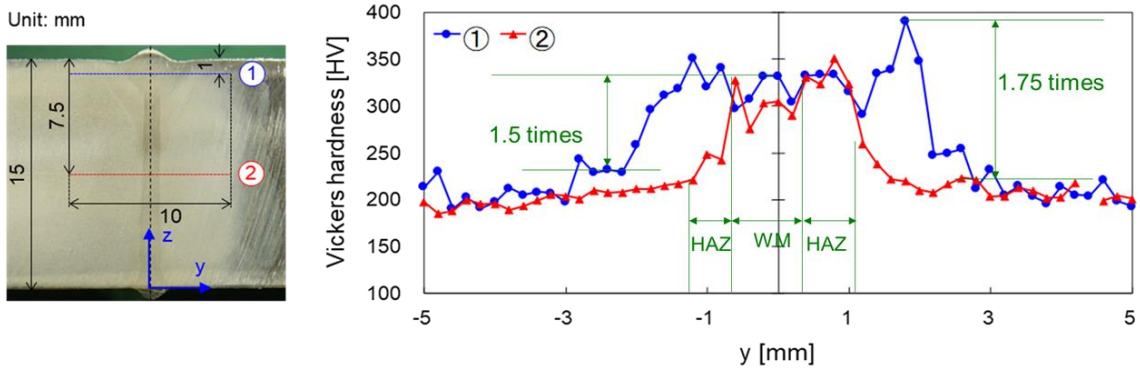

Figure 3.8 Vickers hardness of hybrid-welded butt joint (HWBJ-1)

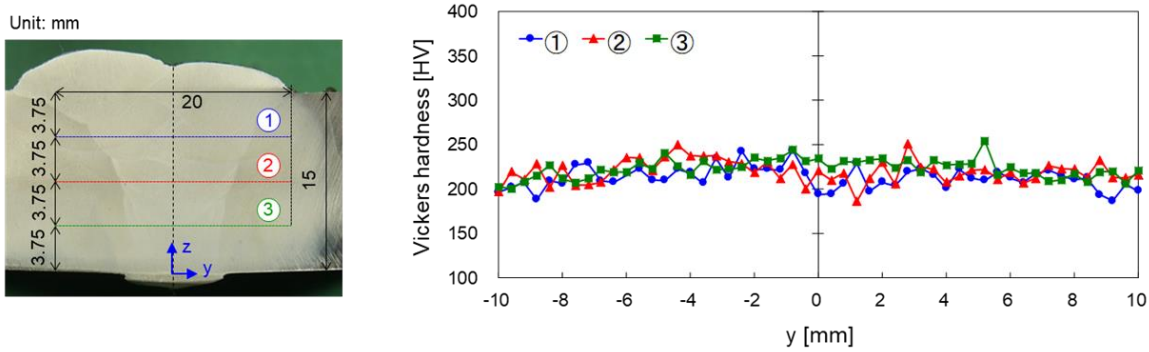

Figure 3.9 Vickers hardness of arc-welded butt joint

3.3.2 Analysis Conditions

(a) Hybrid welding simulation

The fully-coupled thermal elastic-plastic analysis was performed using the software Abaqus to simulate the butt welding experiment detailed in Section 2.3.2. The analytical model, depicted in Figure 3.10, utilized an 8-node brick element with reduced integration. The mesh division perpendicular to the weld line was determined from the cross-sectional macroscopic photographs presented in Figure 2.6 (a), and the element length along the weld line direction was established at 1 mm. An element birth function was employed to accurately model the

deposition of weld metal in the excess and slit areas. The moving heat sources were employed. Mechanical boundary conditions were constrained to rigid body displacement, and thermal boundary conditions considered heat transfer to the surrounding air. The ambient and initial temperatures of the model were set based on the experimental conditions. Moreover, the model leveraged the symmetry of the experimental specimen by employing a half-model approach.

Regarding the material properties of the base metal, the temperature-dependent stress-strain relationship and various physical constants shown in Figure. 3.11 were derived from previous literature [3.4] [3.5] [3.6].

In this study, following previous research [3.2], the heat input from the laser and the arc was modeled as uniform body heat fluxes. The respective melt zones were defined as the areas of arc and laser heating. Repeated heat conduction analyses were conducted to determine these zones, effectively replicating the molten pool shapes observed experimentally. The spatial relationship between the laser and arc heat sources during welding was not considered; simultaneous heating was assumed.

The calculations for the laser heat input, Q_L [J/mm], and arc heat input, Q_A [J/mm], were conducted using equations (3.1) and (3.2), respectively.

$$Q_L = \frac{P \cdot \eta_L}{v} \tag{3.1}$$

$$Q_A = \frac{I \cdot V \cdot \eta_A}{v} \tag{3.2}$$

Here

P : laser power (W)

I : arc current (A)

V : arc voltage (V)

v : welding speed (mm/s)

η_L : thermal efficiency of laser

η_A : thermal efficiency of arc

Thermal efficiencies vary by the welding process. Prior studies have documented thermal efficiencies ranging from 0.5 to 0.9 for laser [3.7] [3.8] and from 0.65 to 0.8 for arc [3.9]. In light of these findings, the efficiency values were carefully examined to ensure alignment between the simulated and experimental temperature histories. Consequently, the thermal efficiencies selected were η_L = 0.6 for laser and η_A = 0.7 for arc. This selection was based on the criterion that the model's predicted thermal profiles closely match those measured experimentally, ensuring that the simulations are both realistic and reliable.

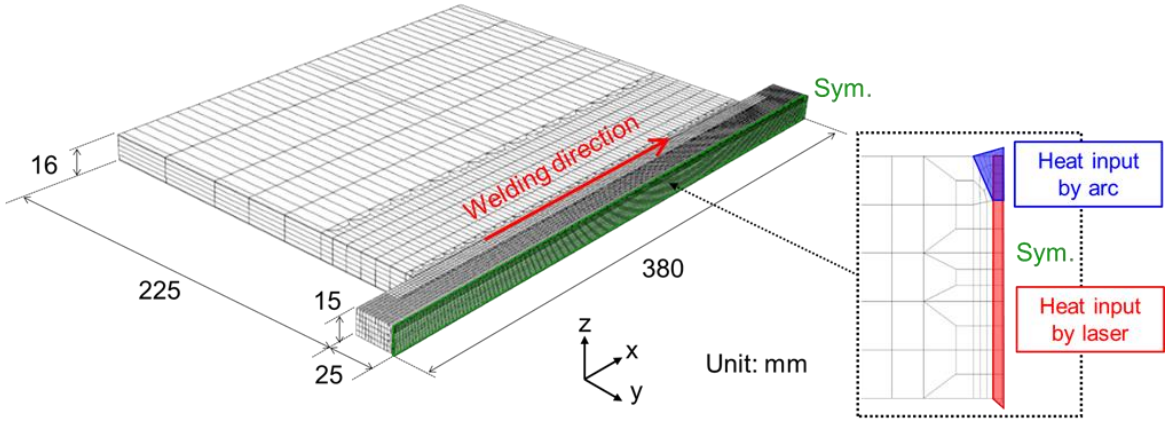

Figure 3.10 FE model for thermal elastic-plastic analysis on hybrid welding specimen.

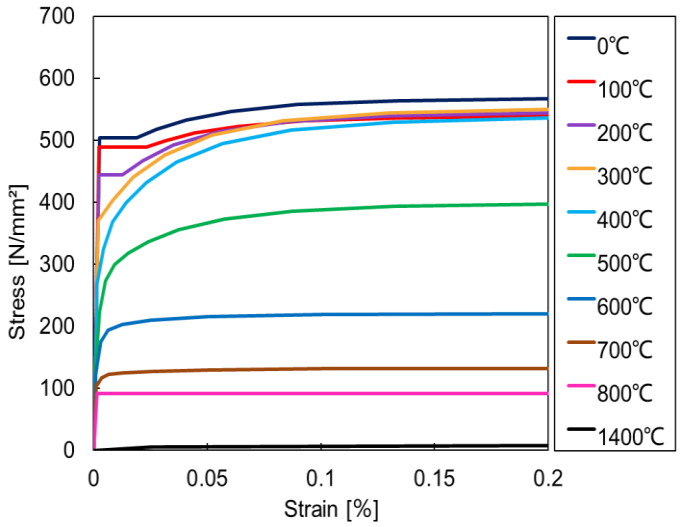

(a) Relationship between stress and strain (base metal)

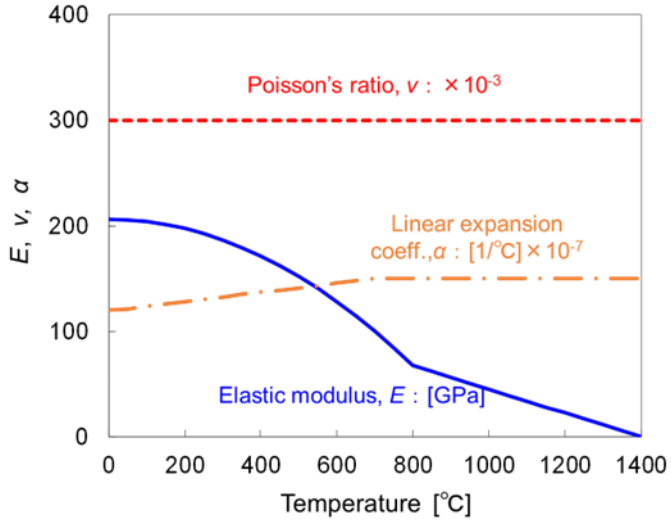

(b) Elastic modulus, Poisson's ratio, and linear expansion coefficient

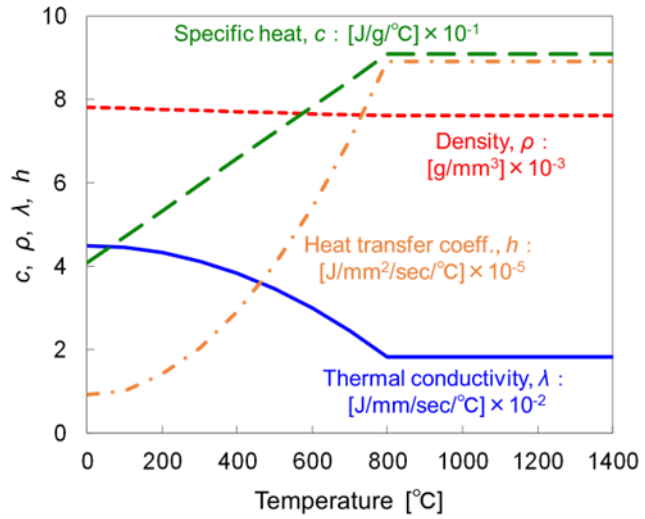

(c) Physical constants and heat transfer coefficient

Figure 3.11 Mechanical properties and physical constants used for analysis

(b) Arc welding simulation

The arc-welded butt joint experiment was simulated by a fully-coupled thermal elastic-plastic analysis. Unlike the symmetrical half-model employed in hybrid welding, the analytical model for arc welding, depicted in Figure 3.12, utilized a full model to accurately represent the asymmetrical buildup of the weld bead. The mesh division perpendicular to the weld line was based on the cross-sectional macroscopic photographs displayed in Figure 2.6 (b), with an

element length of 10 mm along the weld line. Other analysis conditions were consistent with those described in Section 3.3.2 (a). After repeatedly examining the thermal efficiency to ensure alignment with the experimental temperature history, a thermal efficiency of η_A = 0.7 was determined.

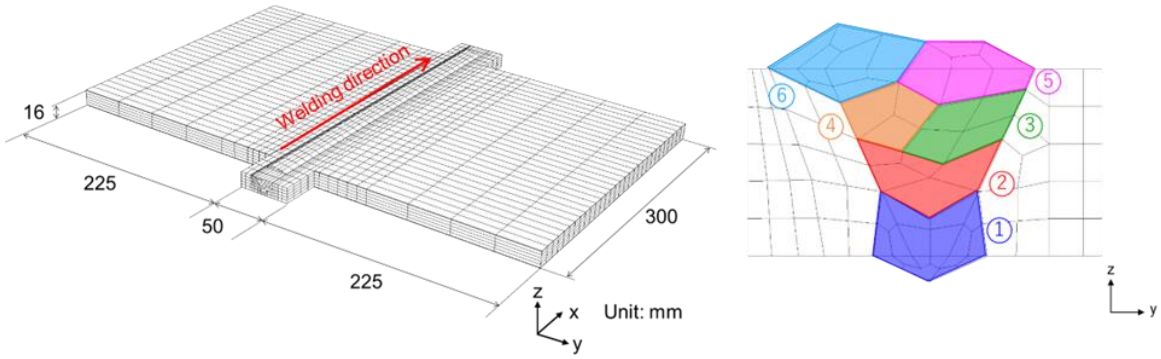

Figure 3.12 FE model for thermal elastic-plastic analysis on arc welding specimen

3.3.3 Analysis Results

(a) Temperature history

Figure 3.13 illustrates the temperature histories obtained from both the hybrid welding experiments and their corresponding simulations. It was confirmed that the experimental and analytical results generally align.

Figure 3.14 displays the temperature histories from arc welding and its simulation, with a similar confirmation that both experimental and analytical results coincide.

It was evident that the maximum temperatures reached in hybrid welding were lower than those in arc welding at identical measurement positions. Furthermore, it was confirmed that the cooling rate of hybrid welding was faster than that of arc welding.

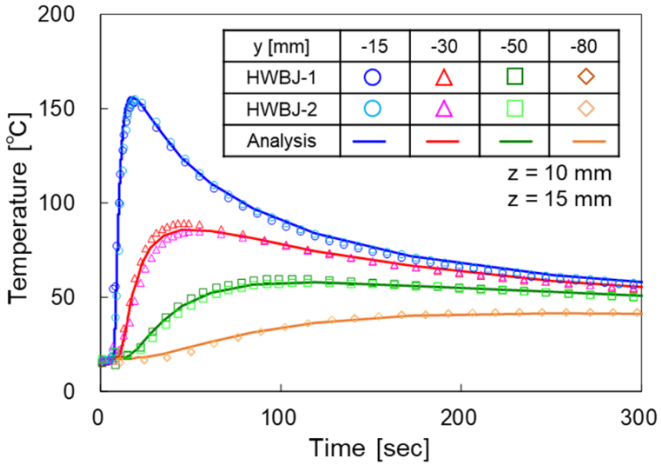

Figure 3.13 Temperature histories obtained by hybrid welding and its simulation

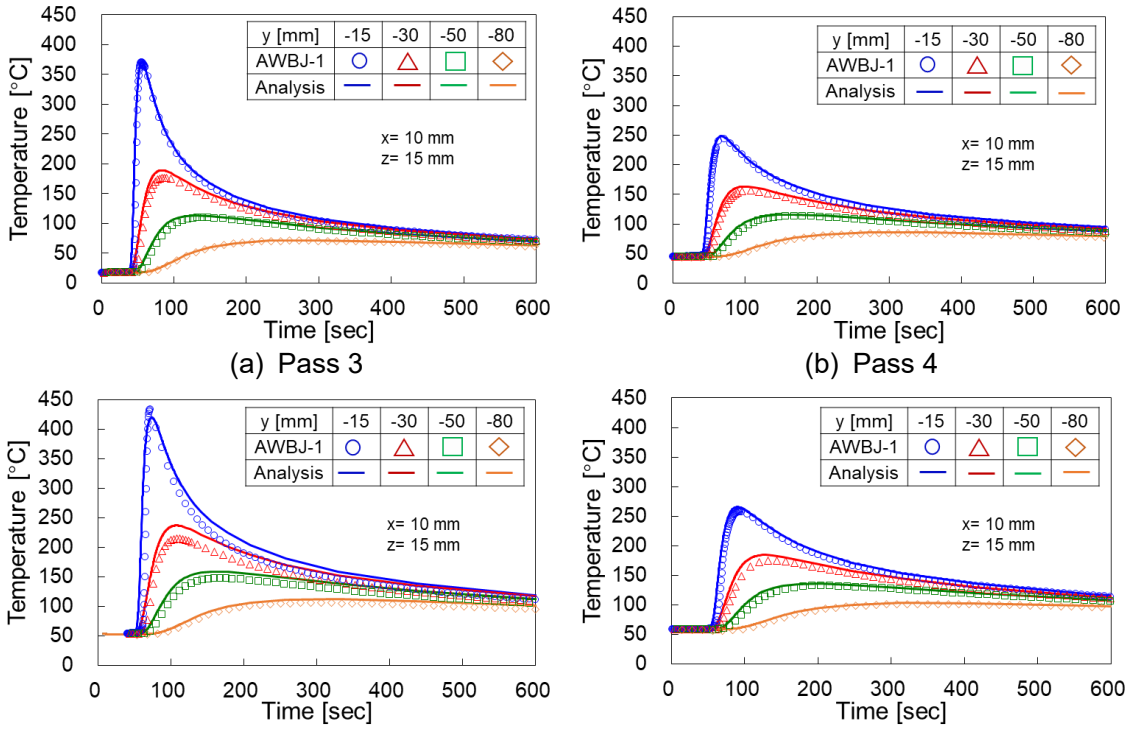

(a) Pass 3 (b) Pass 4

(c) Pass 5 (d) Pass 6

Figure 3.14 Temperature histories obtained by arc welding and its simulation

(b) Welding deformation

Figure 3.15 (a) and (b) illustrate the angular distortion at x = 0 mm for both hybrid and arc welding, derived from experiments and simulations. In hybrid welding (refer to Figure 3.15 (a)), the central plots depict predicted values interpolated linearly from measured data, with dashed lines representing simulated interpolations in the weld bead region. Similarly, in arc welding (see Figure 3.15 (b)), predicted values are shown, with dashed lines indicating simulated angular distortions in the same region. The analytical results for both welding methods closely replicate the trends observed in the experimental data, thereby confirming the accuracy of the simulations in reflecting actual welding distortions.

Figure 3.15 (c) presents a comparison of angular distortions from hybrid and arc welding, according to the analysis. The angular distortions were 0.6 mm for hybrid welding and 10.8 mm for arc welding. Compared to conventional arc welding, the angular distortion in hybrid welding was reduced by 95%.

In the initial welding pass of arc welding, the underside of the steel plate was heated to a high temperature, leading to an inverted V-shaped distortion as it cooled and contracted. Subsequent passes heated and contracted the top side of the plate, with the latter contractions exceeding the initial, thereby resulting in a V-shaped overall distortion. In contrast, hybrid welding completed full penetration welding in a single pass, reducing the heat input and minimizing the temperature gradient across the steel plate compared to arc welding. This led to less angular distortion in hybrid welding than in arc welding. The reduced angular distortion in hybrid welding could diminish the need for strain correction during the fabrication of steel structural components, potentially offering advantages in terms of time and cost efficiency.

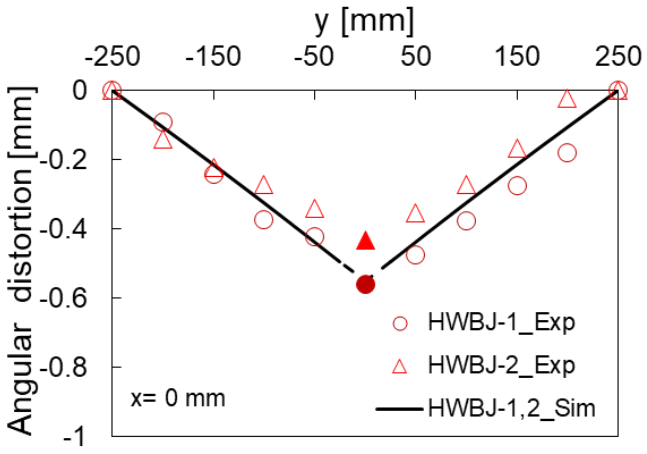

(a) Hybrid welding experiments and simulation

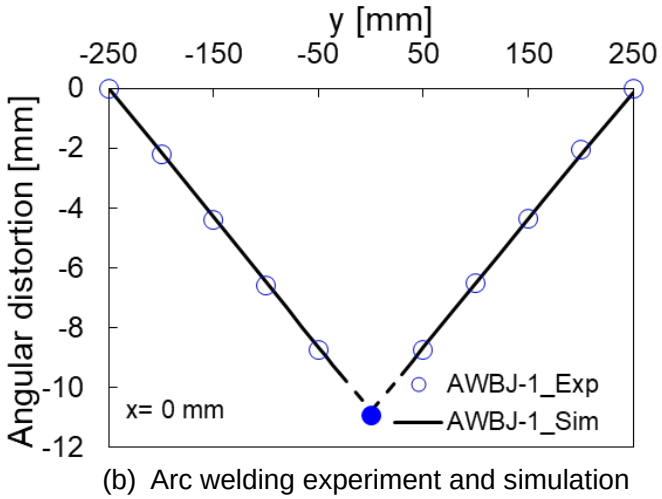

(b) Arc welding experiment and simulation

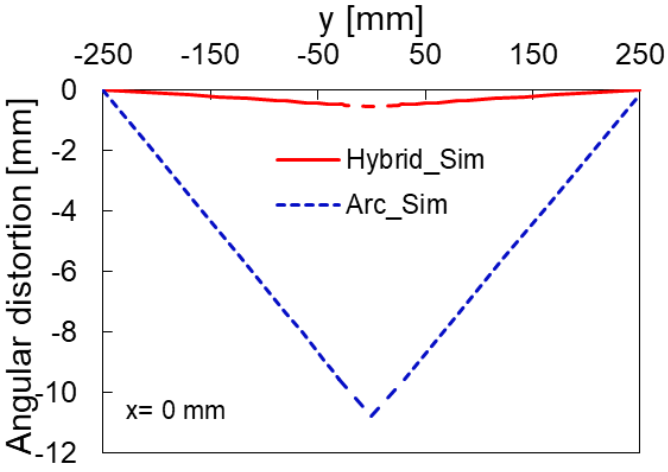

(c) Hybrid and arc welding simulation

Figure 3.15 Angular distortions obtained by welding experiments and simulation

(c) Residual stress

Figure 3.16 (a) and (b) illustrate the residual stresses aligned with and perpendicular to the weld line direction in hybrid welding, derived from both experimental data and analytical predictions. The experimental data averaged residual stress measurements from specimens HWBJ-1 and HWBJ-2 at locations y = -10 mm and 10 mm. The analytical values of the welded metal section were extracted from the surface of the weld seam in the model. The analytical results were well-aligned with the observed experimental trends, both parallel and perpendicular to the welding line. Moreover, the analysis has revealed detailed distributions of residual stresses that were not captured by experimental measurements. Specifically, Figure 3.16 (a) shows that tensile stresses were observed within approximately 25 mm of the center (-12.5 mm < y < 12.5 mm), consistent with experimental observations. The analytical model predicted a sharp increase in residual stress values near the weld line due to higher yield stress and tensile strength settings for the weld metal compared to the base material (detailed in Section 3.3.1). In the direction of the welding line, the peak analytical tensile residual stress reached 721 N/mm², and the maximum analytical compressive residual stress was -52 N/mm². In the perpendicular direction, the maximum analytical tensile and compressive stresses were 149 N/mm² and -288 N/mm², respectively, indicating a sharp increase in compressive stresses near the weld line.

As confirmed by Section 3.3.3 (a), (b), and (c), the developed analytical model for hybrid welding accurately replicated experimental outcomes with high fidelity, supporting the validity of the hybrid welding model. Furthermore, the analysis also provided an in-depth look at the detailed distributions of residual stresses.

Figure 3.17 (a) (b) presents the experimental and analytical residual stresses for arc welding in both directions. The analytical values for the weld metal section were obtained from the bead surface. In Figure 3.17 (a), while the analytical values were generally close to the experimental results, discrepancies such as the value at location y = -10 mm were observed but considered

acceptable given that the positions within ±10 mm of the weld line fell within the weld bead area, where significant measurement error by the X-ray diffraction method (XRD) increased [3.10]. The maximum tensile residual stress obtained through analysis was 689 N/mm², and the maximum compressive residual stress was -122 N/mm². Regarding Figure 3.17(b), both experimental and analytical values showed significant fluctuations near the welding line, making it difficult to assert a consistent trend between experimental and analytical results. Nevertheless, the position at a distance of 10 to 20 mm from the cross direction of the weld line was the region, where the weld bead changed to the based metal. It was thus inferred that the measurement error by the X-ray diffraction method (XRD) increased. The analytical approach obtained a maximum tensile stress of 274 N/mm², with no compressive residual stress detected.

These results thus confirmed that the analytical model for arc welding developed in this study could closely replicate the experimental findings and provide detailed insights into the distributions of residual stresses.

Figure 3.18 (a) and (b) compare the residual stresses from hybrid and arc welding simulations. In Figure 3.18 (a), hybrid welding exhibited maximum tensile residual stresses of 721 N/mm² and compressive residual stresses of -52 N/mm², localized within a 25 mm span around the weld line (-12.5 mm ≤ y ≤ 12.5 mm). In contrast, arc welding showed a broader distribution of tensile residual stresses, up to 689 N/mm², extending over 50 mm (-25 mm ≤ y ≤ 25 mm), with the maximum compressive residual stresses reaching -122 N/mm². Beyond the region, the compressive residual stresses in the direction of the welding line were generated to counterbalance the tensile residual stresses, thus reducing the load-carrying capacity of welded structures. Compared to arc welding, hybrid welding displayed a narrower range of tensile residual stress and a correspondingly lower maximum compressive residual stress. Considering the reduced out-of-plane deformation associated with hybrid welding, as discussed in Section

3.3.3 (b), this suggested that, compared to arc welding, hybrid welding may offer superior compressive load-carrying capacity in welded structures.

In Figure 3.18(b), the maximum tensile residual stresses in hybrid welding and arc welding are 149 N/mm² and 274 N/mm², respectively. The tensile residual stresses perpendicular to the weld line direction could critically reduce the fatigue strength of butt joints. Hybrid welding exhibited a substantial 125 N/mm² reduction compared to arc welding. This significant decrease suggests that hybrid-welded butt joints are likely to have superior fatigue strength than arc-welded ones.

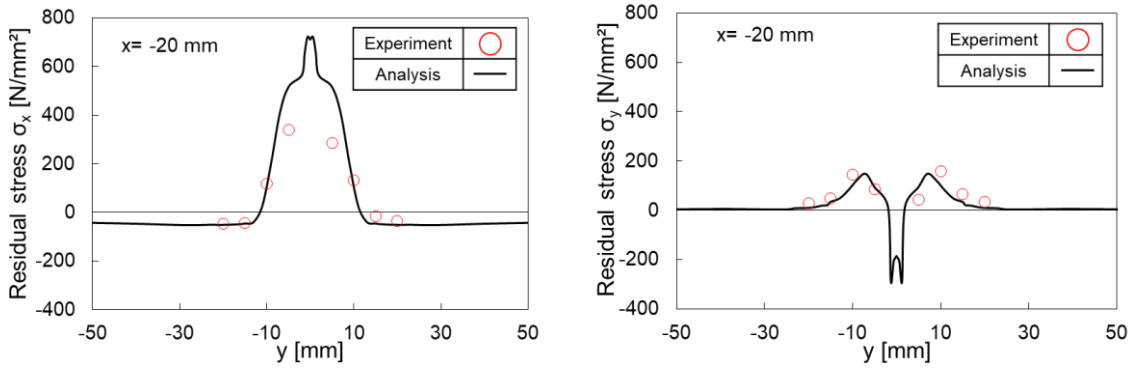

(a) Residual stress in welding direction (b) Residual stress in cross direction

Figure 3.16 Residual stresses obtained by hybrid welding and its simulation

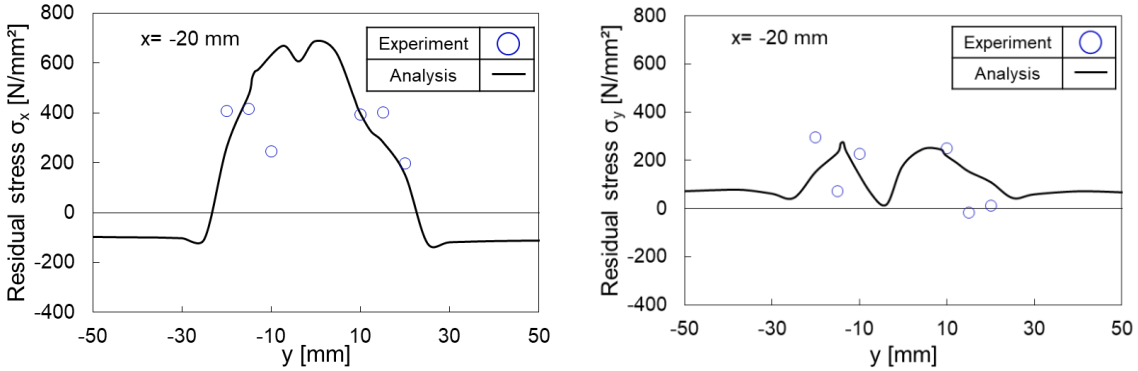

(a) Residual stress in welding direction (b) Residual stress in cross direction

Figure 3.17 Residual stresses obtained by arc welding and its simulation

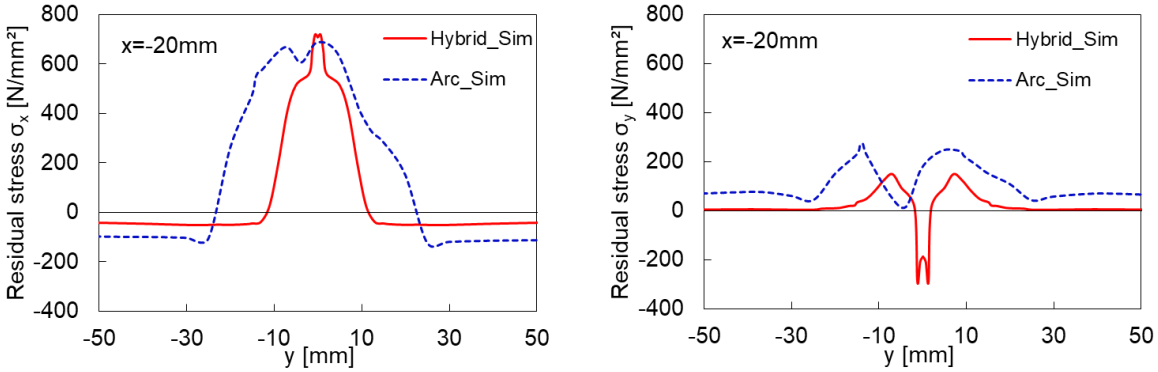

(a) Stress component in welding direction

(b) Stress component in cross direction

Figure 3.18 Comparison of stress components by hybrid and arc welding simulation

3.4 Summary

In this chapter, hybrid-welded butt joints fabricated in Chapter 2 were employed to obtain out-of-plane deformations and residual stresses. Thermal elastic-plastic analysis was performed to elucidate the detailed distribution of deformations and stresses. For comparative analysis, similar measurements and simulations were conducted on conventional arc-welded butt joints. Through a series of experiments and numerical simulations, this chapter presented the following conclusions.

(1) The angular distortions were 0.6 mm for hybrid welding and 10.8 mm for arc welding. Compared to conventional arc welding, the angular distortion in hybrid welding was reduced by 95%.

(2) The maximum compressive residual stress along the weld line direction in hybrid welding was around 70 N/mm² lower than that in arc welding. Furthermore, the range of tensile residual stress was reduced by about 50%. Given the diminished out-of-plane deformation induced by hybrid welding, hybrid welding may offer superior compressive load-carrying capacity in welded structures compared to arc welding.

(3) Hybrid welding exhibited a substantial reduction of 125 N/mm² in tensile residual stress along the cross direction relative to arc welding. Therefore, hybrid-welded butt joints are likely to have superior fatigue strength than arc-welded ones.

Reference

[3.1] P. Dai, P.M. Kyaw, N. Osawa, S. Rashed, D. Ma, J. Okada, M. Honnami. (2023) Numerical study on local residual stresses induced by high frequency mechanical impact post-weld treatment using the optimized displacement-controlled simulation method. J Manuf Process 92: 262-271. https://doi.org/10.1016/j.jmapro.2023.03.002

[3.2] Hirohata M, Takeda F, Suzaki M, Inose K, Matsumoto N, Abe D. (2019) Influence of laser-arc hybrid welding conditions on cold cracking generation. Weld World 63: 1407-1416. https://doi.org/10.1007/s40194-019-00749-6

[3.3] P. ZHANG, S. X. LI, Z. F. ZHANG. (2011) General Relationship between Strength and Hardness. Materials Science and Engineering A 529: 62-73. https://doi.org/10.1016/j.msea.2011.08.061

[3.4] F. FURUMURA, T. ABE, T. OKABE and W.-J. KIM. (1986) A Uniaxial Stress-strain Formula of Structural Steel at High Temperature and Its Application to Thermal Deformation Analysis of Steel Frames. Journal of Structural and Construction Engineering (Transaction of AIJ) 363: 110-117. (in Japanese)

[3.5] H. NAKAGAWA and H. SUZUKI. (1999) Ultimate Temperatures of Steel Beams Subjected to Fire. Steel Construction Engineering 6 (22): 57-65. (in Japanese) https://doi.org/10.11273/jssc1994.6.22_57

[3.6] Kim Y-C, Lee J-Y, Inose K. (2007) Dominant factors for high accurate predication of distortion and residual stress generated by fillet welding. Steel Stru 7(2): 93-100.

[3.7] Yasuda K, Kitani Y. (2000) Metallurgical characteristics of CO2 laser weld metal in heavy plates. Weld Int 14(10):787–793. https://doi.org/10.1080/09507110009549269

[3.8] Miyazaki Y, Katayama S. (2016) Power attenuation and focus shift of solid state laser beam caused by laser-induced plume. Weld Int 30(11):846–857. https://doi.org/10.1080/09507116.2016.1142207

[3.9] Joseph A, Harwig D, Farson DF, Richardson R. (2003) Measurement and calculation of arc power and heat transfer efficiency in pulsed gas metal arc welding. Sci Technol Weld Join 8(6):400–406. https://doi.org/10.1179/136217103225005642

[3.10] PS Prevey (1986) X-ray Diffraction Residual Stress Techniques. ASM Handbook,10, ASM, 380–392.

Chapter 4 Mechanical Performance of Laser-arc Hybrid-welded Joints

4.1 Introduction

The fatigue performance of welded joints is crucial for ensuring the long-term reliability and durability of steel structures, such as steel bridges, vehicles, and ships. In Section 3.3.3 (c) of Chapter 3, it was inferred that the fatigue performance of laser-arc hybrid-welded joints may be superior to that of arc-welded joints. This inference is further examined in this chapter by assessing the fatigue strength of hybrid-welded joints under the established fatigue design curves for arc-welded joints.

Furthermore, the toughness of materials, critically quantified by Charpy absorbed energy, is vital when materials are subject to sudden or unpredictable loads. Detailed in Section 3.3.1 of Chapter 3, the weld metal (WM) and heat-affected zone (HAZ) in hybrid-welded butt joints using SBHS have undergone significant hardening due to substantial temperature gradients at the weld seam. Since hardening in steel typically leads to a reduction in toughness, it is essential to investigate the toughness of hybrid-welded butt joints. One of the key metrics for assessing the toughness of welded structures is the Charpy absorbed energy. Consequently, Charpy impact tests will be performed to determine the toughness of both the weld metal and the heat-affected zone in these hybrid-welded joints.

4.2 Four-point Bending Fatigue Test

4.2.1 Experimental Specimens

The experiment specimens with shapes and dimensions as shown in Figure 4.1 were extracted from hybrid- and arc-welded butt joints.

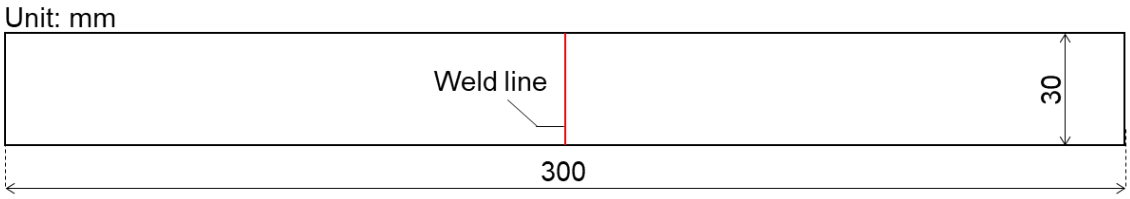

Figure 4.1 Experimental specimen for fatigue test.

4.2.2 Experimental Setup

To investigate the fatigue characteristics of hybrid-welded joints, fatigue tests were conducted. For comparative purposes, the fatigue strength of arc-welded joints was also assessed. The loading conditions, as depicted in Figure 4.2, involved subjecting specimens to four-point bending loads with a support span of 240 mm and a uniformly stressed region of 100 mm. This setup ensured the central placement of the weld zone within the uniformly stressed section. The specimens were positioned on the supports such that tensile stresses from the bending loads acted on the upper surfaces of the hybrid-welded joints. The relationship between stress and time during the fatigue tests is illustrated in Figure 4.3. The range of applied stresses was determined based on the nominal tensile stresses at the surface of the specimens within the uniform bending section, with a stress ratio set at 0.1. Strain gauges were attached to 5 mm from the weld toes to monitor the strain amplitude during repeated loading cycles. Upon the initiation and propagation of fatigue cracks at the weld toe, a decrease in strain amplitude was observed relative to its initial value. This reduction, quantified as 5% from the initial value, was defined as the endpoint for fatigue life in these experiments. Prior research indicated that a 5%

reduction in strain gauge amplitude at a location 5 mm from the weld toes corresponded to a crack depth of approximately 1 mm (a physical microcrack) [4.1]. The termination of the tests occurred when the specimen either succumbed to fracture or surpassed 2.5 million cycles of repeated loading; subsequently, the number of cycles at which the strain amplitude demonstrated a 5% reduction from the initial value was computed.

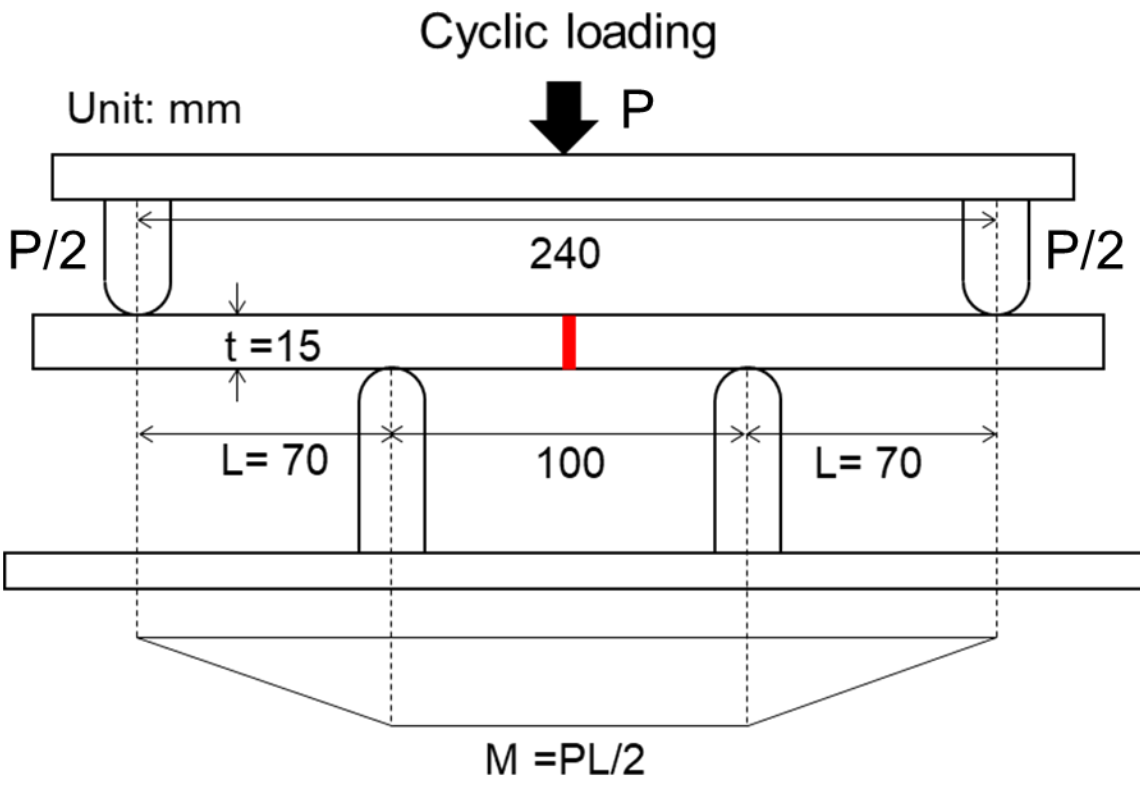

Figure 4.2 Loading conditions

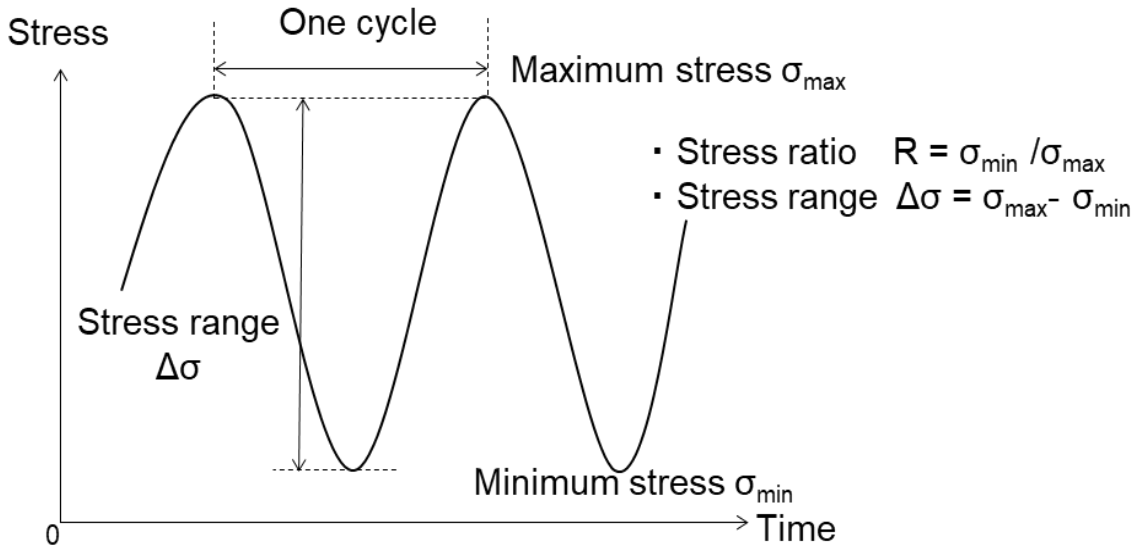

Figure 4.3 Relationship between stress and time.

4.2.3 Test Results

The fatigue behavior of hybrid-welded joints was evaluated through four-point bending fatigue tests, as detailed in Figure 4.4. These fatigue specimens conformed to the JSSC class D design curve, which is typically applied to arc-welded joints (butt, without weld toe treatment according to reference [4.2]). The fatigue life of these joints closely followed the JSSC class D mean curve.

The fatigue strength under bending loads is typically approximately one grade higher than under axial loads, with an increase of about 20% to 25%. The "Fatigue Design Recommendations for Steel Structures" issued by the Japan Society of Steel Construction [4.2] recommends that when welded joints are subjected to out-of-plane bending, the resultant stress should be scaled down by a factor of 4/5. This adjusted stress range should then be combined with the axial stress range to obtain the normal stress range. Adhering to the JSSC Guidelines, the fatigue test outcomes with the adjusted nominal stress range are presented in Figure 4.5. After applying the 4/5 conversion factor, the hybrid-welded joints still met the requirements of the

Class D design curve, whereas the arc-welded joints did not perform adequately at higher stress ranges.

Figure 4.6 demonstrates that fractures in all fatigue specimens originated from the weld toes. At a nominal stress of 200 N/mm², prior to adjusting by the 4/5 factor, there was no evidence of crack initiation in either the hybrid-welded or arc-welded specimens. This suggests that both types of joints maintained structural integrity under these lower stress ranges. However, at stress levels elevated to 250 N/mm² and beyond, without the 4/5 conversion factor, the hybrid-welded specimens exhibited a fatigue strength that was either equivalent to or exceeded that of the arc-welded specimens.

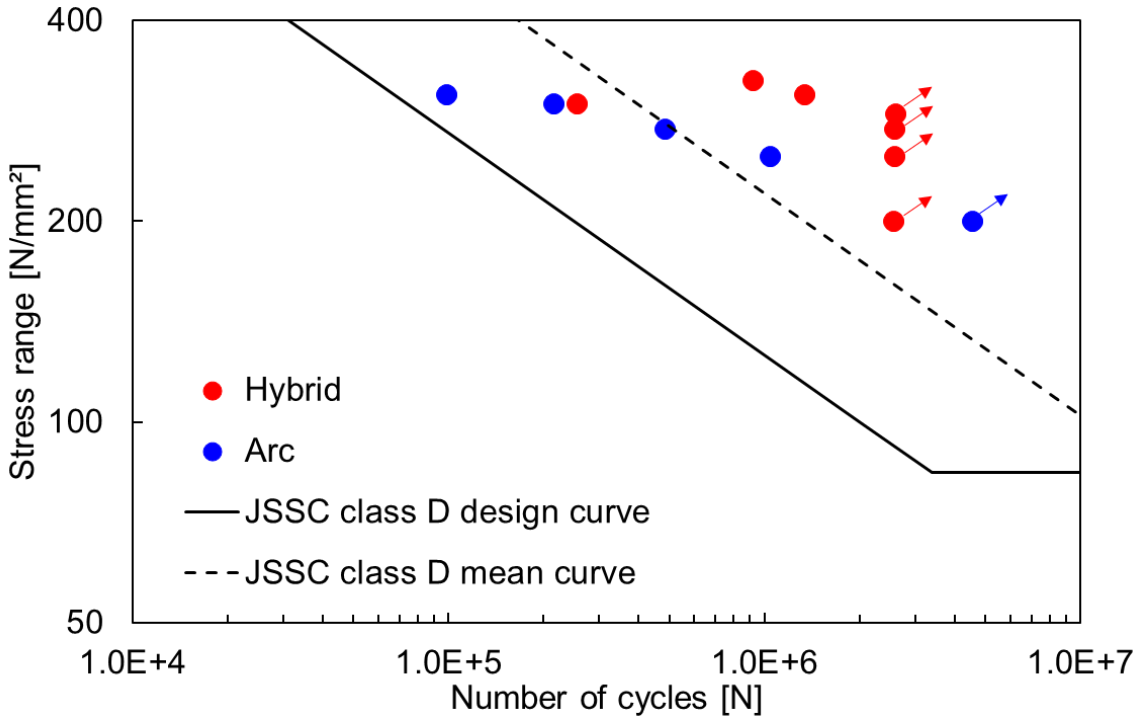

Figure 4.4 Fatigue test results.

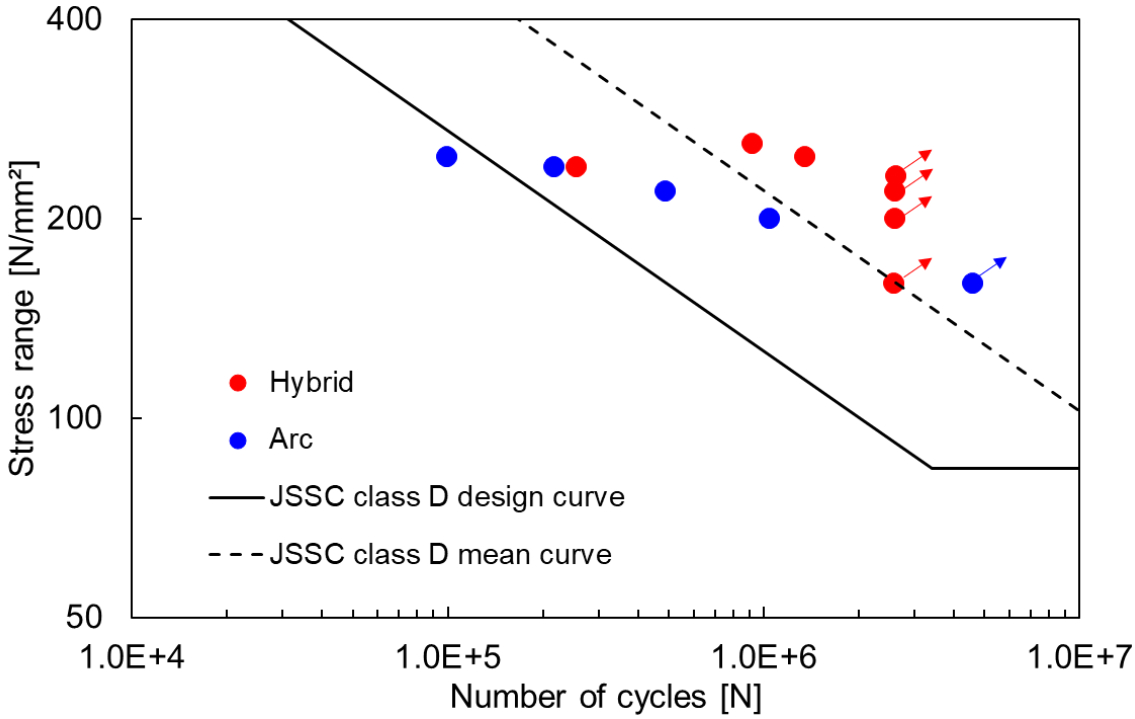

Figure 4.5 Fatigue test results with stress range multiplied by 4/5

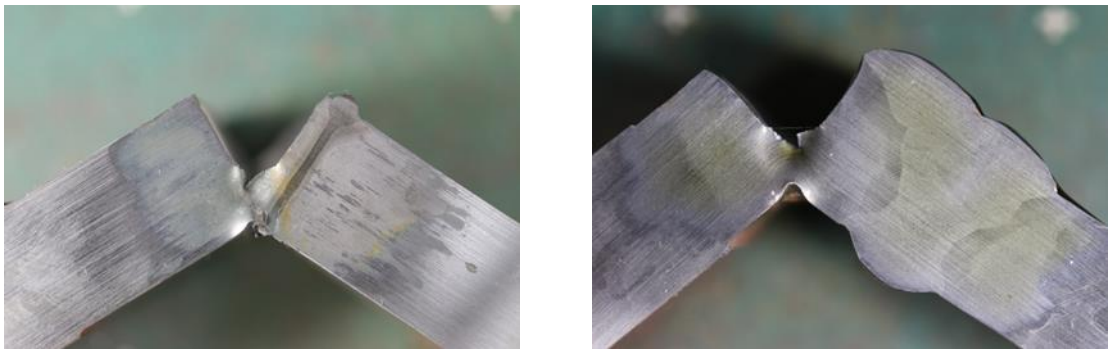

(a) Hybrid welding (b) Arc welding

Figure 4.6 Ruptured specimens for hybrid- and arc-welded joints

4.2.4 Investigation of Differences in Fatigue Life

In Section 4.2.3, it was demonstrated that the fatigue life of hybrid-welded joints surpassed that of arc-welded joints when subjected to stress ranges exceeding 250 N/mm². As illustrated in Figure 4.7, a slower rate of strain amplitude reduction was observed for specimens under a 300 N/mm² stress range in hybrid welded joints, suggesting an inhibited crack propagation rate. This trend was consistent under stress ranges of 275 N/mm², 290 N/mm², and 310 N/mm². Moreover, as shown in Figure 4.6, fatigue cracks originated at the weld toe, progressed through the heat-affected zone, and then propagated through the base material. Given that the properties of the base material were identical for both welded joints, it was inferred that there were no significant differences in the rate of crack propagation through the base material. Therefore, the superior fatigue life of hybrid-welded joints was attributed primarily to a suppressed rate of crack initiation and early-stage propagation.

To elucidate the mechanisms underlying this suppression, Vickers hardness tests were performed on the weld toes of both hybrid-welded and arc-welded joints. As displayed in Figure 4.8, measurements were conducted at intervals of 0.5 mm within a 2 mm span centered on the weld toes, ranging from -1 mm to 1 mm, and at depths from 0.5 mm to 1 mm below the surface of the welded joints. As shown in Figure 4.9, the hardness values ranged between 268 HV and 311 HV in hybrid-welded joints and between 187 HV and 215 HV in arc-welded joints. The greater hardness near the weld toes in hybrid welded joints, likely due to rapid heating and cooling, confirmed an increase in strength at the weld toes. This enhanced strength is considered to significantly contribute to the inhibition of crack propagation during the initial stages.

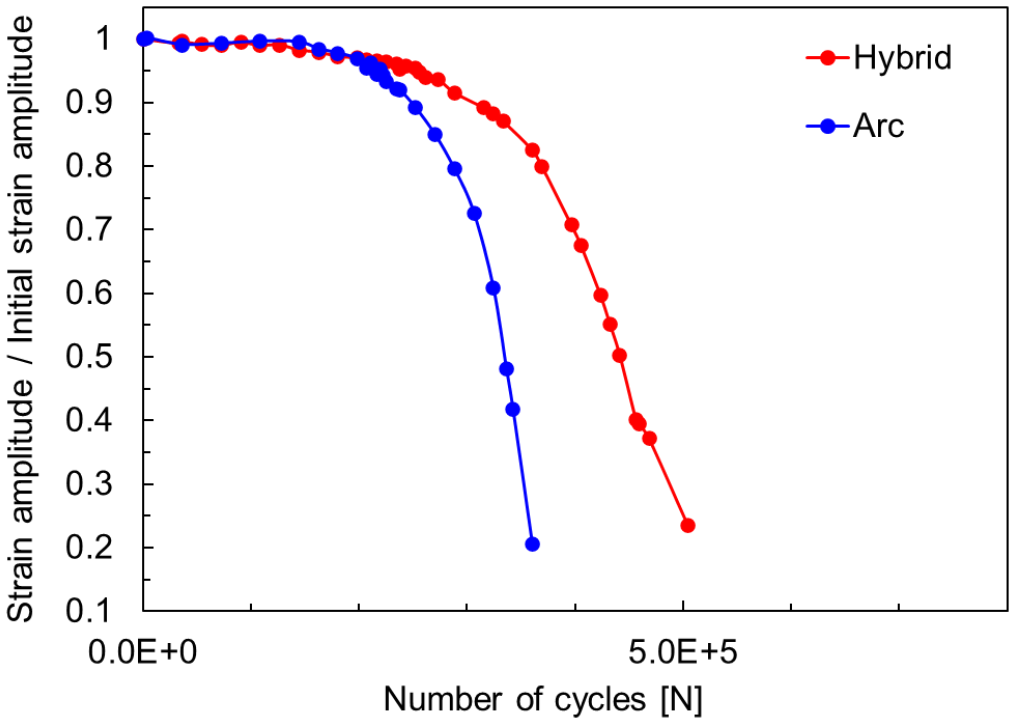

Figure 4.7 Fatigue behavior of decreasing strain amplitude (300 N/mm²)

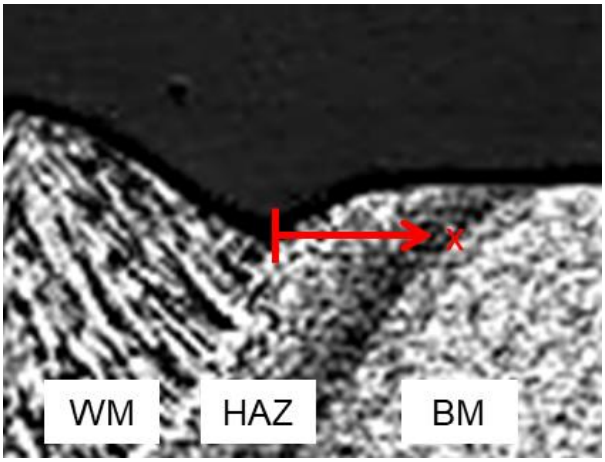

(a) Hybrid welding

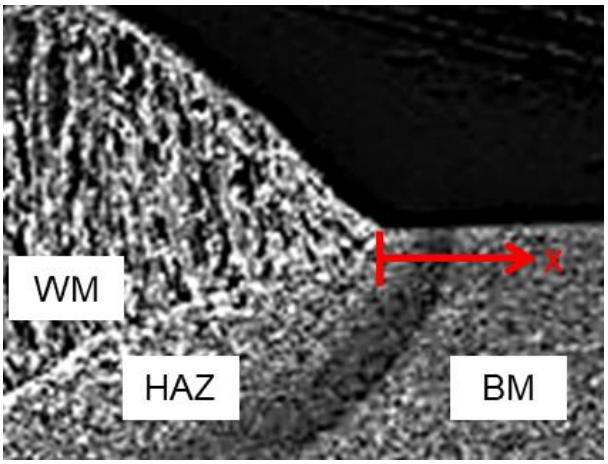

(b) Arc welding

Figure 4.8 Vickers hardness test on weld toe

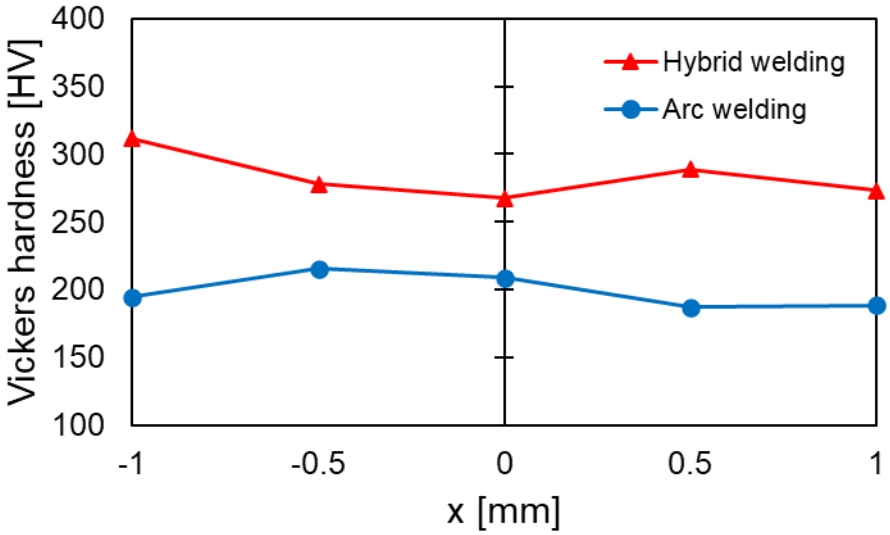

Figure 4.9 Test results of Vickers hardness

4.3 Charpy Impact Test of Welded Joints

4.3.1 Test Specimen

Test pieces were extracted from the weld metal (WM), heat-affected zone (HAZ), and base metal (BM) of two hybrid-welded joints, HWBJ-1 and HWBJ-2. For each category, three specimens were taken at a depth of 1-2 mm from the surface of welded joints. These specimens were prepared in accordance with the No. 4 test piece, featuring a V-shaped notch as prescribed by JIS Z 2242. The three-dimensional geometry of the test pieces is depicted in Figure 4.10. Charpy impact tests were then performed on these specimens at a test temperature of 0°C.

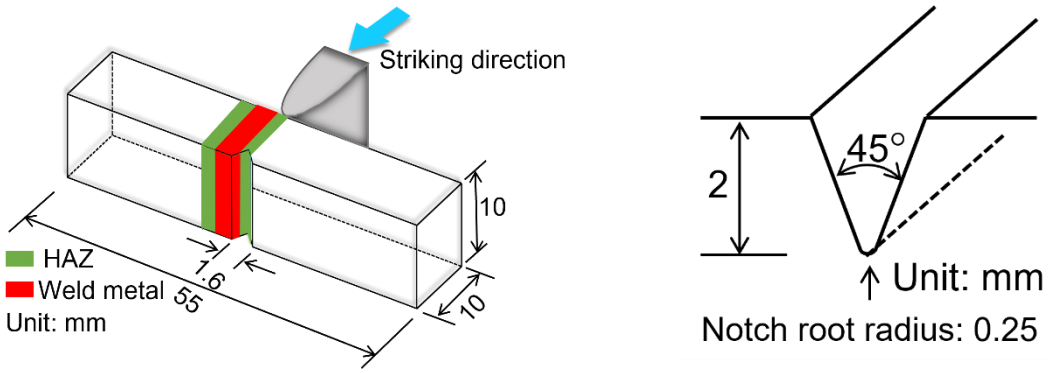

(a) Shape and dimensions of test pieces (b) V-shaped notch

Figure 4.10 The three-dimensional geometry of the test piece

4.3.2 Charpy Absorbed Energy

Figure 4.11 presents the Charpy absorbed energy for each specimen category, with identifiers for each specimen distinctly marked. The figure delineates the specified value of Charpy absorbed energy for the base material, which is 100 J, represented by a solid line. In contrast, the actual measured average value of the base material, depicted by a dashed line, was significantly higher, recorded at 294 J. This measured value is nearly threefold the specified

value. Consistent findings were observed in both the weld metal (WM) and the heat-affected zone (HAZ), where the Charpy absorbed energy values closely aligned with those recorded for the base material.

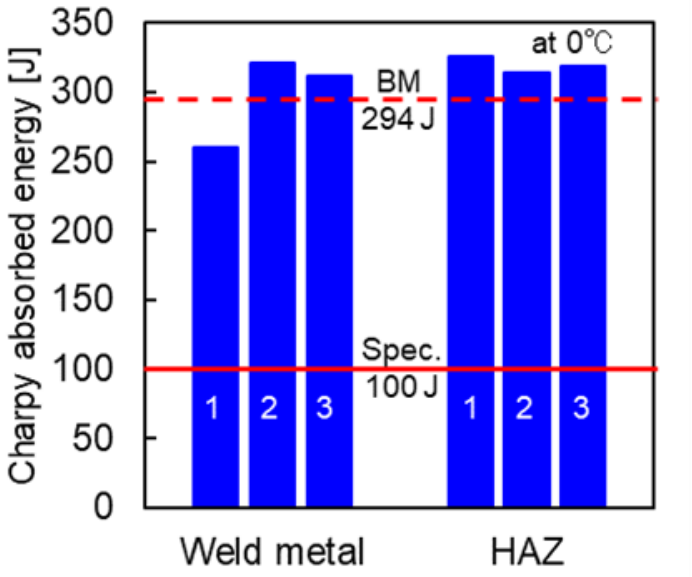

Figure 4.11 Charpy absorbed energy for each specimen category

4.3.3 Fracture States and Brittle Fracture Surface Ratio

Figure 4.12 illustrates the fracture states of the specimens, all of which displayed brittleness fraction surface ratios of 0%. In these specimens, it was observed that cracks deviated from the notch tip, extending toward the base material and culminating in ductile fractures within the base material itself. This phenomenon suggested that the test outcomes may not accurately reflect the Charpy absorbed energy of the weld metal and the heat-affected zone (HAZ). The challenges associated with measuring localized toughness in the narrow weld metal and HAZ of hybrid-welded joints were well-documented [4.3]. Similar challenges have been noted in previous studies examining narrow weld zones in laser welding, where Fracture Path Deviation (FPD) was frequently observed, with cracks originating in the weld metal and deviating toward the base

material [4.3]. The width of the HAZ in hybrid-welded butt joints was approximately 1 mm, a dimension within which significant variations in material properties, such as hardness, were found. Consequently, capturing the localized toughness of such narrowly defined areas via Charpy impact tests presented considerable difficulties. In this study, all specimens exhibited FPD, underscoring the potential influence of notch placement precision and the varying material characteristics of the HAZ on test results. This variability made the fracture path likely to deviate from the notch tip toward the base material, contrasting with results from more homogeneous materials.

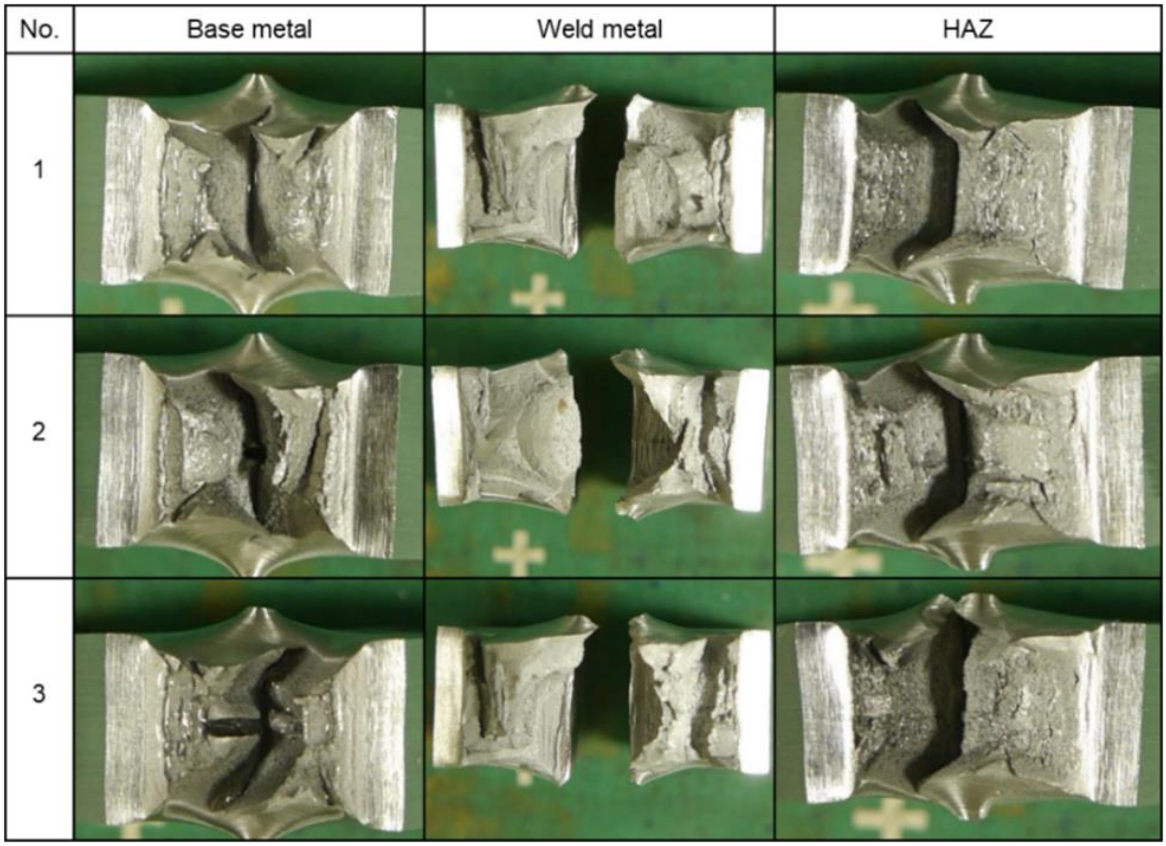

Figure 4.12 Fracture state

4.4 Simulated Welding Thermal Cycle Tests

4.4.1 Thermal Cycle Simulated Test Pieces

In the Charpy impact tests conducted on the hybrid-welded butt joints, no specimen succeeded in accurately determining the Charpy absorbed energy for the weld metal and HAZ, thus hindering a comprehensive assessment of the toughness of welded joints. To overcome this limitation, simulated thermal cycle tests were implemented to reproduce the HAZ as a homogeneous material. These tests aimed to replicate the metallurgical structure of the HAZ by simulating the thermal cycles that the base material undergoes during hybrid welding, thereby reducing material heterogeneity and enabling an estimation of the Charpy absorbed energy of HAZ. It is crucial to acknowledge, however, that this method does not replicate the metallurgical structure of the weld metal, since the material does not melt and only the HAZ is simulated.

For the simulated thermal cycle tests, specimens measuring 120 mm × 12 mm × 12 mm were extracted from the base metal of the hybrid-welded joints. The testing employed the THERMECMASTOR-Z, produced by Fuji Electronic Industrial Corporation, utilizing high-frequency induction heating for thermal cycles and helium gas injection for cooling. Thermocouples installed in the center of the specimens controlled the temperature. The specimens were heated to peak temperatures of 1350 °C, 1200 °C, 1050 °C, and 900 °C, maintained for 5 seconds, and then cooled at a rate of 80 °C/s.

4.4.2 Metallographic Observation

The metallographic structures of the actual heat-affected zone (HAZ) and simulated thermal cycle materials were thoroughly compared and examined. The actual HAZ was categorized into three distinct regions: Region ① (coarse-grain HAZ), Region ② (midsection HAZ), and Region

③ (fine-grain HAZ), as shown in Figure 4.13. These regions were imaged at a magnification of 500x, as shown in Figure 4.14 (a). To facilitate the comparison of metallographic structures between the actual HAZ and the simulated HAZ, the structures of materials subjected to various peak temperatures (1350°C, 1200°C, 1050°C, and 900°C) were similarly captured at a magnification of 500x, as illustrated in Figure 4.14 (b).

Upon heating the steel above its transformation temperature, an austenitic structure forms, which, upon quenching, transforms into martensite and bainite. This transformation results in the coarsening of metallographic structures, thereby increasing hardness while decreasing toughness. The proportions of these coarsened structures are crucial in evaluating the metallurgical similarity between the actual HAZ and simulated materials. These proportions were quantitatively analyzed using the image analysis software WinROOF2018, and the findings are presented in Table 4.1.

In the actual HAZ, coarsened structures were observed in Regions ① and ②. In contrast, in the simulated materials, such structures were found in the specimens heated to 1350°, 1200°, and 1050°C. Both the 1350°C and 1200°C materials exhibited nearly 100% coarsened structures, with the 1350°C material predominantly composed of martensite. The 1200°C and 1050°C materials primarily consisted of bainite. For the specimen heated to 900°C and held for 5 seconds, no complete transformation to the γ-phase occurred, and consequently, no coarsened structures were detected. Although direct measurement of the grain size from the microstructural photographs of Region ③ and the 900°C material is challenging, comparative analysis indicates that the grain size in the 900°C simulated material was finer than that observed in Region ③.

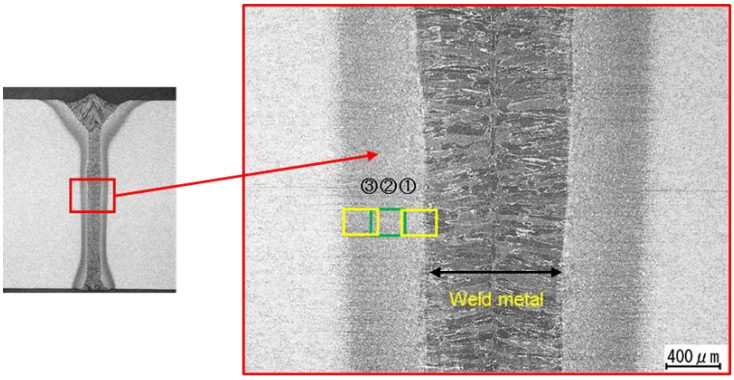

Figure 4.13 Metallographic observation location for hybrid-welded joints

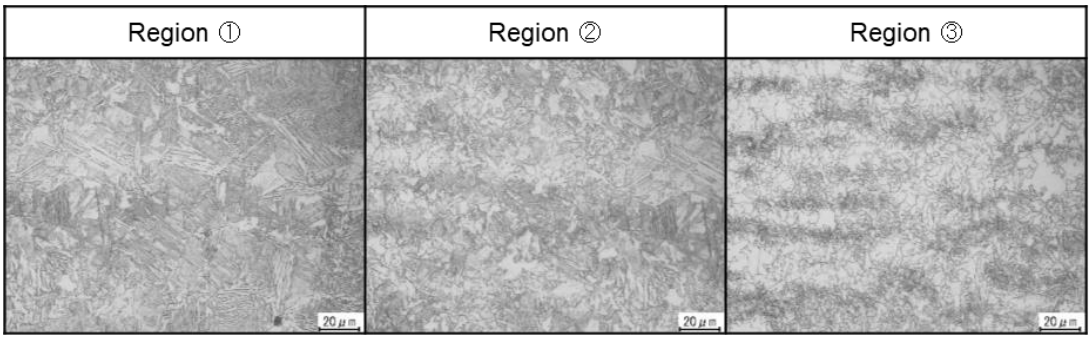

(a) Metallographic structure in actual HAZ

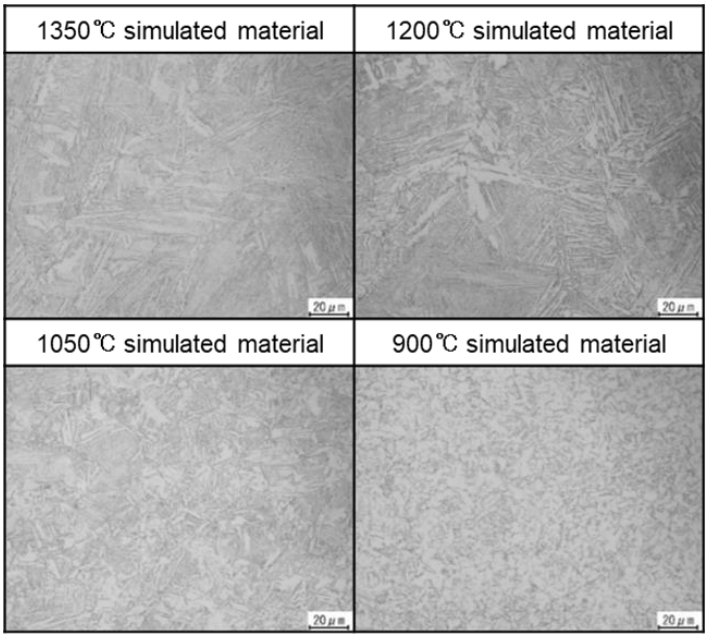

(b) Metallographic structure in simulated material

Figure 4.14 Comparison of metallographic structures between actual HAZ and simulated material

Table 4.1 Coarsened fraction of HAZ and simulated thermal cycle material

	Actual HAZ			
	Region①	Region②	Region③	
Coarsened metallographic structure fraction [%]	85	23	0	
	Thermal cycle simulated materials			
	1350°C	1200°C	1050°C	900°C
Coarsened metallographic structure fraction [%]	100	95	70	0

4.4.3 Vickers Hardness Test

Hardness, similar to the proportion of coarsened metallographic structures, is also an essential metric for assessing the metallurgical similarity. Accordingly, the hardness of each specimen was quantitatively evaluated using the Vickers hardness test. The results are displayed in Figure 4.15. The analysis revealed that the hardness of the material subjected to a peak temperature of 1350°C aligned with that observed in Region ①. Similarly, the hardness values for materials exposed to peak temperatures of 1200°C and 1050°C corresponded to those measured in Region ②. The hardness of the material that was subjected to a peak temperature of 900°C paralleled the hardness observed in Region ③.

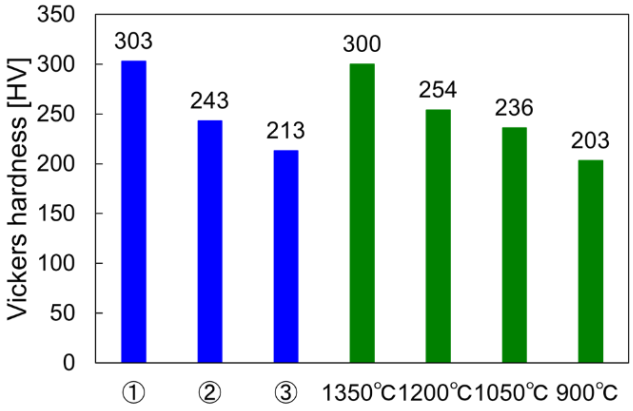

Figure 4.15 Hardness of actual heat-affected zone and thermal cycle simulated materials

4.4.4 Metallographic Similarity Assessment

Metallurgical similarity was evaluated by analyzing both the proportion of coarsened metallographic structures and the Vickers hardness measurements. Region ① exhibited a metallographic state intermediate between the materials subjected to peak temperatures of 1200°C and 1350°C. The 1350°C material demonstrated a fully coarsened structure, predominantly composed of martensite, whereas Region ① consisted largely of bainite (85%), thereby showing greater similarity to the 1200°C material that was also bainite-dominant. Region ② aligned more closely with the 1050°C material. The comparatively lower proportion of coarsened structures in Region ②, as compared to that in the 1050°C materials, was attributed to the inclusion of metallographic features nearer to the base metal within this region's micrographs. Region ③ was assessed to resemble the metallurgical condition of the 900°C material or to be slightly more akin to the heat-affected zone microstructure on the base metal side.

It was, therefore, concluded that the simulated thermal cycle tests, conducted under conditions of maximum heating temperatures of 1200°C, 1050°C, and 900°C with a cooling rate of 80°C/sec, effectively replicated the metallurgical structures across the three regions of the heat-affected zone in the hybrid welded joints.

4.5 Charpy Impact Test on Simulated Thermal Cycle Materials

4.5.1 Simulated Test Specimen

Charpy impact tests were conducted on simulated test pieces, which were extracted from materials subjected to simulated thermal cycles. These specimens effectively replicated the metallurgical structures of the heat-affected zone (HAZ) in the hybrid-welded butt joints, as described in Section 4.4.4. Three specimens from each set of conditions— 1350°C, 1200°C, 1050°C, and 900°C— were tested. The shape and dimensions of these simulated test pieces conformed precisely to those used in the Charpy impact tests detailed in Section 4.3.1. The tests were conducted at a temperature of 0°C.

4.5.2 Test Results

Figure 4.16 presents the Charpy absorbed energy for the simulated test pieces, and Figure 4.17 displays the corresponding fracture states. Due to the uniform metallographic structures near the notch tip, no fracture path deviation (FPD) was observed in these simulated test pieces, and cracks propagated directly from the notch tip, leading to fracture. The simulated test pieces from the 900°C and 1050°C materials exhibited almost no brittle fracture surface, with the brittle fracture surface ratios being close to 0%. In contrast, the brittle fracture surface ratios for the simulated test pieces from the 1350°C and 1200°C materials ranged from approximately 60% to 80%. The Charpy absorbed energy for the simulated test pieces from the 900°C material, resembling fine-grain HAZ, from the 1200°C material, akin to coarse-grain HAZ, as well as from the 1050°C material, representing an intermediate state between the two metallographic states, met the 47 J required to prevent brittle fracture in SBHS400 [4.5]. Moreover, the simulated test pieces from the 1350°C material, which exhibited a more coarsened metallographic structure

than that observed in coarse-grain HAZ, demonstrated a Charpy absorbed energy of 97 J, thereby not only meeting the requirements for bending workability by being below 100 J but also simultaneously preventing brittle fracture by exceeding the 47 J.

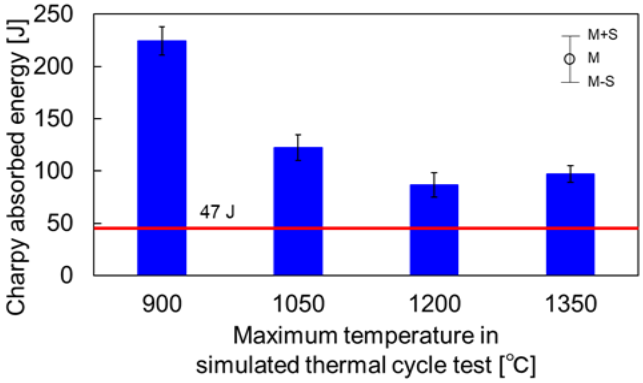

Figure 4.16 Charpy absorbed energy for simulated test pieces

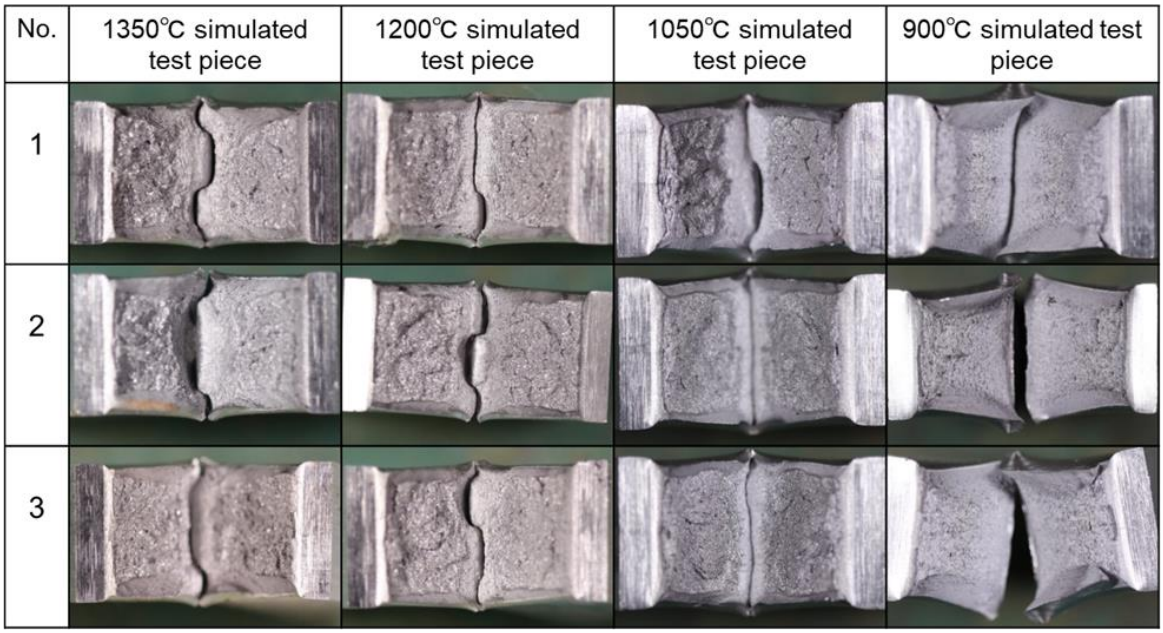

Figure 4.17 Fracture states for simulated test pieces

4.5.3 Comparison with SM400B

To assess the influence of the high Charpy absorbed energy, as guaranteed by SBHS, on the toughness of hybrid-welded joints, this study contrasted the Charpy absorbed energy of thermally simulated test pieces derived from SBHS with those from conventional steel. The conventional steel chosen for this comparative analysis was SM400B, a commonly used structural rolled steel. The mechanical properties and Charpy absorbed energy values for SM400B are detailed in Table 4.2.

Simulated thermal cycle tests replicated the conditions applied to SBHS400, involving peak heating temperatures of 1350°C, 1200°C, 1050°C, and 900°C, coupled with a rapid cooling rate of 80°C/sec. The resultant metallographic images of the simulated thermal cycle materials for SM400B are displayed in Figure 4.18. Consistent with observations in SBHS400, coarsened structures such as martensite and bainite were identified in materials heated to 1350°C, 1200°C, and 1050°C. Notably, the material exposed to 1350°C was completely comprised of martensite, while the material heated to 1200°C and 1050°C predominantly featured bainite, with the 1200°C material showing a higher proportion of bainite.

Specimens were extracted from each condition of the simulated thermal cycle materials and subjected to Charpy impact tests. The geometric specifications of these specimens conformed to those delineated in Section 4.3.1, with the testing temperature maintained at 0°C. The comparative outcomes of the Charpy absorbed energy between the simulated thermal cycle materials for SBHS400 and SM400B are illustrated in Figure 4.19.

For the 900°C material, akin to the fine-grain HAZ, and the 1050°C material, representing the intermediate state between fine-grain and coarse-grain HAZ, both SBHS400 and SM400B satisfied the minimum energy requirement of 47 J. However, for the 1200°C material, analogous to coarse-grain HAZ, and the 1350°C material, which exhibited a more coarsened structure than

the coarse-grain HAZ, the Charpy absorbed energy of SM400B did not exceed 27 J. In contrast, the SBHS material met the 47 J within the scope of this test, indicating that its high toughness was effectively utilized. These results suggest that the high Charpy absorbed energy guaranteed by SBHS could ensure values exceeding 47 J in the heat-affected zones of hybrid-welded joints.

Table 4.2 Mechanical properties of SM400B

Material	Yield strength [N/mm²]	Tensile strength [N/mm²]	Elongation [%]	Charpy absorbed energy [J]
SM400B	300	448	29	185

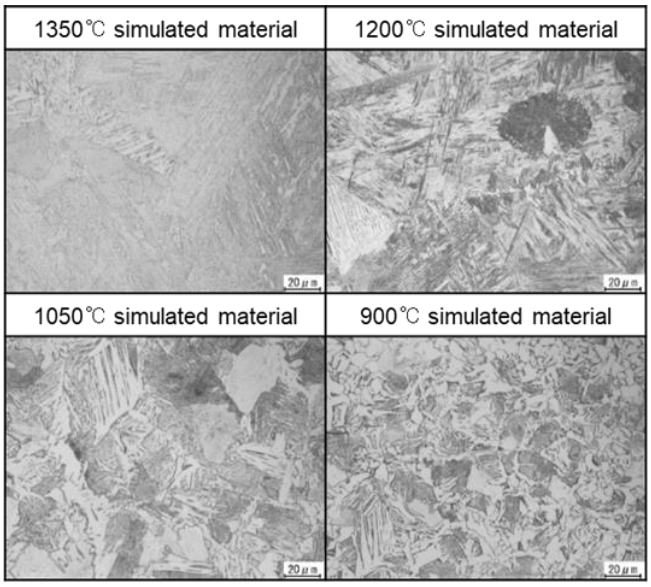

Figure 4.18 Metallographic structure in simulated thermal cycle material using SM400B

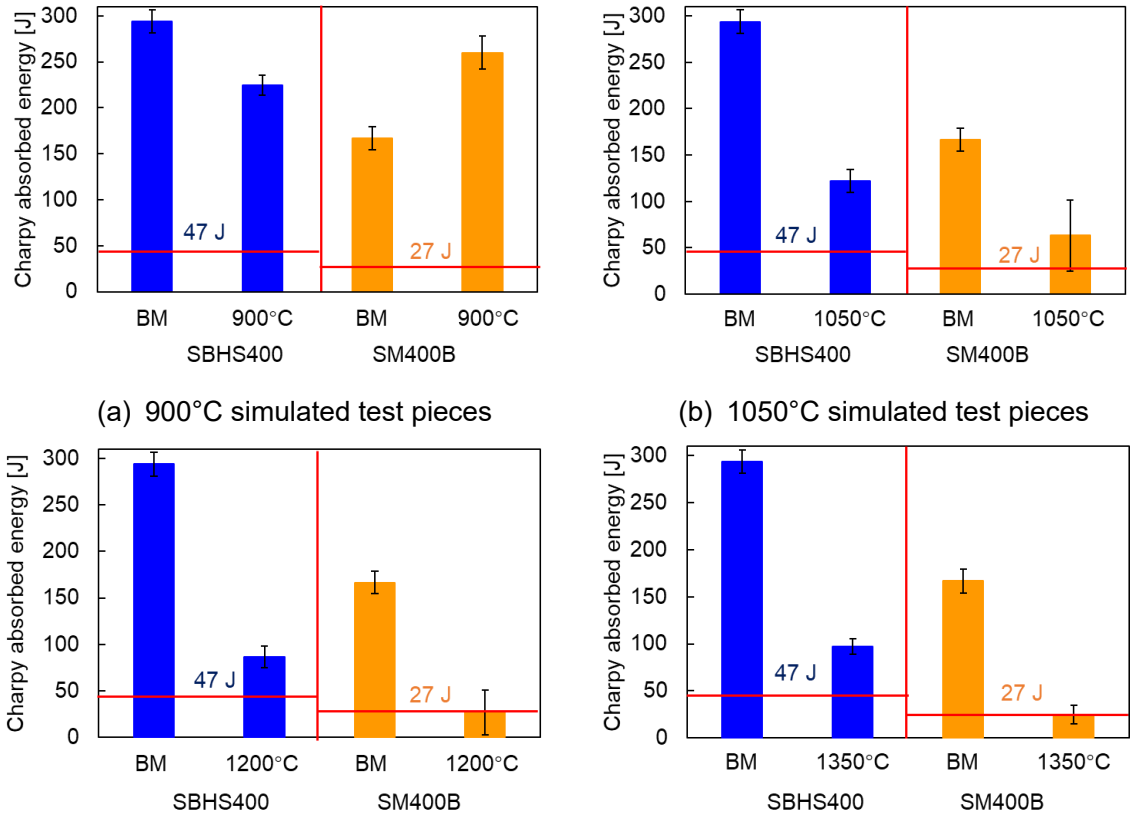

(a) 900°C simulated test pieces

(b) 1050°C simulated test pieces

(c) 1200°C simulated test pieces

(d) 1350°C simulated test pieces

Figure 4.19 Charpy absorbed energy of thermal cycle simulated test piece of SBHS400 and SM400

4.6 Summary

In this chapter, the fatigue characteristics of hybrid-welded joints were compared with those of conventional arc-welded joints. Specimens extracted from both hybrid- and arc-welded joints were subjected to four-point bending fatigue tests to assess their performance under cyclic loading. Moreover, the toughness of the hybrid-welded joints was thoroughly evaluated. The findings can be summarized as follows:

(1) Fatigue test results revealed that under nominal stress ranges exceeding 250 N/mm², hybrid-welded joints displayed equal or superior fatigue strength compared to arc-welded

joints, due to the hardening around the weld toe that enhanced strength and suppressed the rate of crack initiation and early-stage propagation.

(2) Following the JSSC guidelines, after applying the 4/5 conversion factor, hybrid-welded joints met the class D design curve, unlike arc-welded joints, which underperformed at higher stress levels.

(3) Every specimen extracted from the weld metal and the heat-affected zone (HAZ) exhibited fracture path deviation (FPD), which obstructed the precise assessment of Charpy absorbed energy.

(4) Simulated thermal cycle tests were executed at peak heating temperatures of 1350°C, 1200°C, 1050°C, and 900°C, accompanied by a cooling rate of 80°C/sec. These experiments effectively replicated the coarse-grained, fine-grained, and transitional areas of the heat-affected zone (HAZ), as verified through assessments of metallographic structures and hardness profiles.

(5) The results from Charpy impact tests on SBHS400 materials, subjected to simulated thermal cycles at peak temperatures of 1350°C, 1200°C, 1050°C, and 900°C, indicated that the Charpy absorbed energy in the simulated HAZ met the required 47 J to prevent brittle fracture.

(6) The comparison of Charpy absorbed energy between SBHS400 and SM400B showed that both materials satisfied their respective requirements (47 J for SBHS400 and 27 J for SM400B) at 900°C and 1050°C. However, at 1200°C and 1350°C, SM400B's Charpy absorbed energy did not reach 27 J, while SBHS400 consistently achieved 47 J. These outcomes indicate that SBHS likely provides enhanced toughness in the heat-affected zone (HAZ) of hybrid-welded joints due to its higher Charpy absorbed energy in the base metal (BM).

Reference

[4.1] Hassan Al-Karawi, Karawi, Rüdiger U. Franz von Bock und Polach, Mohammad Al-Emrani. (2021) Crack detection via strain measurements in fatigue testing. Strain 57(4): e12384. https://doi.org/10.1111/str.12384

[4.2] Japan Society of Steel Construction. (2012) The Fatigue Design Recommendations for Steel Structures. (in Japanese).

[4.3] Inose, K., Yamaoka, H., Nakanishi, Y. et al. (2017) Toughness assessments of laser arc-hybrid welds of ultra-high strength steel. Weld World 61: 955–961. https://doi.org/10.1007/s40194-017-0483-4

[4.4] Ohata M, Morimoto G, Fukuda Y, Minami F, Inose K, Handa T. (2015) Prediction of ductile fracture path in Charpy V-notch specimen for laser beam welds. Weld. World 59:667–674. https:// doi.org/10.1007/s40194-015-0256-x

[4.5] Japan Welding Engineering Society (1995) WES3003 Evaluation criterion of rolled steels for low temperature application. The Japan Welding Engineering Society, Tokyo

Chapter 5 Load-carrying Capacity of Hybrid-welded Column with L-shaped Section

5.1 Introduction

The load-carrying capacity of steel bridge structural components is pivotal for maintaining their structural integrity and safety, as it determines their ability to withstand daily traffic loads and environmental stresses. Section 3.3.3 (c) of Chapter 3, drawing on empirical data, suggested that hybrid welding may offer superior performance compared to conventional arc welding in terms of the compressive load-carrying capacity of welded structures. This chapter aims to rigorously evaluate this hypothesis through a comprehensive comparative analysis of the load-carrying capacities of hybrid-welded and arc-welded columns. The selected specimens are taken from the corner part of the diagonal members in truss bridges shown in Figure 5.1. The diagonal members have a box section made of 10-12 mm thick steel plates. The corner part, forming an L-shaped section, is extracted from the box section with welded joints. Monotonic compressive loading experiments are performed on these specimens to determine the maximum compressive loads. Eventually, the effectiveness of hybrid welding in the fabrication of steel bridge components is confirmed through comparisons with the widely used arc welding technique. This comparison synthesizes findings from this and previous chapters, examining factors such as out-of-plane deformation, residual stress, fatigue strength, toughness, load-carrying capacity, and constructability.

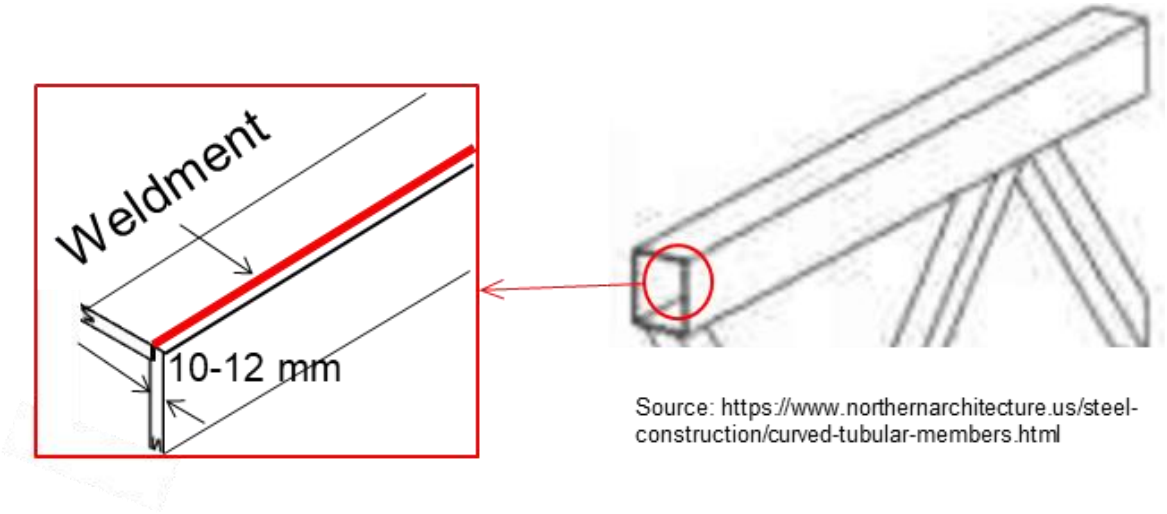

Figure 5.1 Diagonal member in truss bridges

5.2 Corner Joint Welding

5.2.1 Experimental Specimens

In this section, hybrid- and arc-welded columns with L-shaped sections were fabricated to prepare for subsequent monotonic compressive loading experiments. Figure 5.2 depicts the three-dimensional geometries and dimensions of the specimens, alongside the groove configurations used for both welding methods. The joints were assembled from two 12 mm steel plates, tack welded together to connect the loading plates, forming an L-shaped cross-section. This assembly method was designed to facilitate precise load transfer during the testing phase and to mitigate the impact of residual stresses on the corner joints, thereby enhancing the reliability of the experimental outcomes.

For the hybrid-welded specimens, a gap of 0.5 mm was precisely maintained between the plates. The selection of a 0.5 mm gap was based on earlier research [5.1], which demonstrated the capacity of hybrid welding to bridge gaps up to 0.8 mm in 15 mm thick structural steel. In contrast, the arc-welded specimens were engineered with a single 45° bevel and a 1 mm root face to ensure robust joint formation conducive to achieving sound arc-welded corner joints,

similar to the groove processing strategies detailed in section 2.3.1 of Chapter 2 for arc-welded butt joints.

The chemical composition and mechanical properties of the base metal and filler materials used are comprehensively detailed in Table 5.1. It is noteworthy that the steel grade used for constructing the column differs from that employed in the hybrid-welded and arc-welded butt joints discussed in Chapter 2. In the case of the hybrid-welded and arc-welded butt joints, SBHS400 was utilized, whereas this chapter employed SBHS500. SBHS500, offering higher strength and more extensive applications compared to SBHS400, was selected for the fabrication of the columns. This selection is underpinned by the superior mechanical properties and broader applications of SBHS500.

5.2.2 Experimental Methods

Figure 5.3 demonstrates the experimental setup for both hybrid and arc welding techniques, with 100% CO_2 used as the shielding gas for each. In the hybrid welding setup, the arc torch was positioned ahead of the laser head, facilitating one-pass full penetration as outlined in the welding conditions listed in Table 5.2. In stark contrast, the arc welding technique required four welding passes: it began with three passes along the machined groove sides of the joints, followed by gouging, and concluded with a final pass from the rear to achieve equivalent full penetration. Each welding method was applied to four joints, designated as HWJ-1, HWJ-2, HWJ-3, HWJ-4 for hybrid welding and AWJ-1, AWJ-2, AWJ-3, AWJ-4 for arc welding. Hybrid welding was performed in a horizontal orientation, whereas all passes in arc welding were conducted downward.

For each type of welding technique, three thermocouples were attached to the surface of Panel 2. For hybrid welding, the thermocouples were positioned at coordinates x = 27.5 mm,

37.5 mm, 47.5 mm; y = 250 mm; z = 0 mm. For arc welding, they were positioned at x = 38 mm, 48 mm, 58 mm; y = 250 mm; z = 0 mm.

The out-of-plane deformations of the specimens were measured along the y-direction before and after welding. For Panel 1, measurements were taken along the lines at x = 0 mm and z = 50 mm, and for Panel 2, along the line at x = 65 mm and z = 0 mm. The differences in these measurements correspond to the deformations caused by welding.

Residual stress in Panel 1 was measured using X-ray diffraction. Measurements were taken at various points (z-values of 2.5, 7.5, 12.5, 17.5, 22.5, 27.5, 32.5, 37.5, 47.5, 57.5, 67.5, 77.5, 87.5 mm) along the line at y = 230 mm and x = 0 mm for both hybrid- and arc-welded specimens. For hybrid-welded specimens, measurements were also taken on the x-axis at 2.5, 20, 25, 30, 35, 40, 45, 50, 55, 60, 65, 75, 85, 95 mm, and for arc-welded specimens at x-values of 2.5, 30, 35, 40, 45, 50, 55, 60, 65, 75, 85, 95 mm, with both sets along the line at y = 230 mm and z = 0 mm. Before these measurements were taken, the area surrounding the measurement positions was electropolished to a depth of about 300 μm in order to remove any influences from surface treatments.

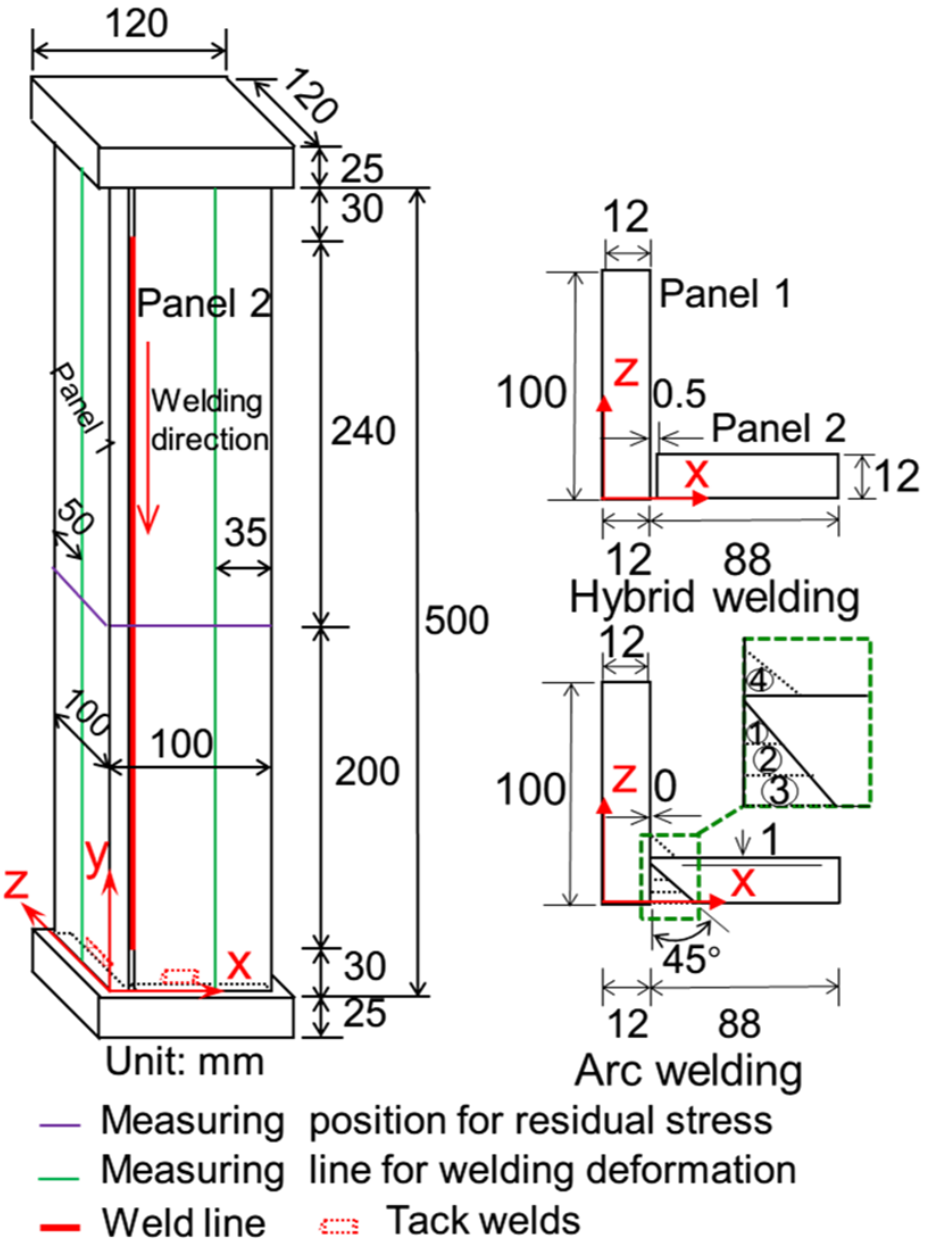

Figure 5.2 Three-dimensional geometries and dimensions of columns

Table 5.1 Chemical composition and mechanical properties of SBHS500 and filler material

Material	Chemical compositions [mass%]								Yield strength [N/mm²]	Tensile strength [N/mm²]	Elon-gation [%]
	C	Si	Mn	P	S	Ni	Cr	Cu			
SBHS500	0.10	0.22	1.54	0.014	0.002	0.02	0.14	0.01	587	684	35
YGW11	0.08	0.51	1.10	0.010	0.010	—	—	—	490	570	31

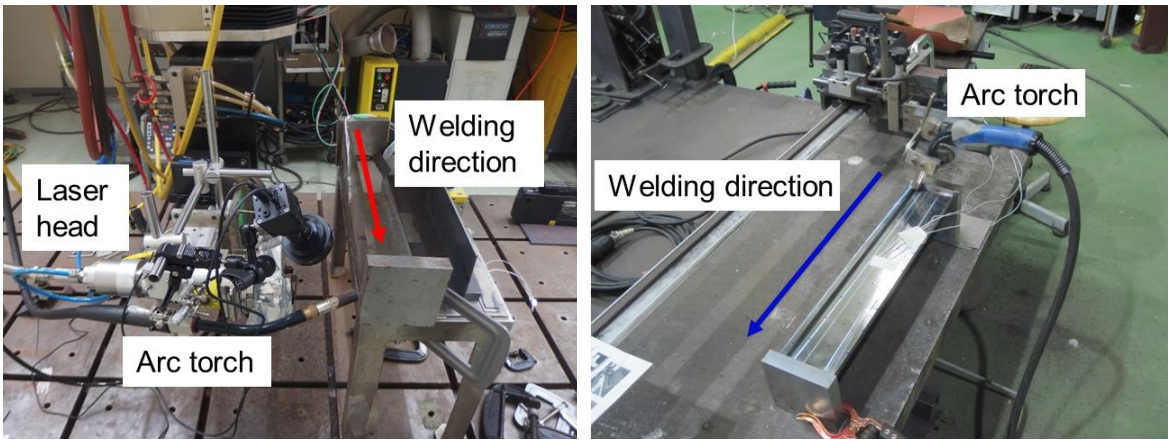

(a) Hybrid welding (b) Arc welding

Figure 5.3 The experimental setup for hybrid and arc welding

Table 5.2 Welding conditions

Welding condition	Welding pass	Laser power [kW]	Arc current [A]	Arc voltage [V]	Welding speed [m/min]	Heat input [J/mm]		
						Laser	Arc	Total
Hybrid welding	1	6.8	230	23.8	1.2	340	274	614
Arc welding	1	—	175	24.5	0.35	—	735	7652
	2	—	250	30.5	0.35	—	1307	
	3	—	250	31.0	0.2	—	2325	
	4	—	300	36.5	0.2	—	3285	

Figure 5.4 illustrates the as-welded conditions of both hybrid-welded and arc-welded specimens. To assess the quality of these joints, cross-sectional observation was performed on specimens (HWJ-4 and AWJ-4) from both welding methods, after measuring the out-of-plane deformation and residual stress. Their cross-sections were meticulously observed to assess the integrity and quality of the welds.

Figure 5.5 presents cross-sectional macroscopic photographs of joints using both hybrid and arc welding. Meticulous visual inspection revealed no defects in the joints from either method, underscoring the high quality and effectiveness of the welding procedures employed. Notably, hybrid welding achieved significantly deeper penetration compared to arc welding, a feature

clearly shown in Figure 5.5. While arc welding required four passes to achieve full penetration, hybrid welding accomplished this in a single pass, even with thick steel plates. This stark contrast not only highlights the superior efficiency and process simplification afforded by hybrid welding but also enhances the structural integrity of the welds.

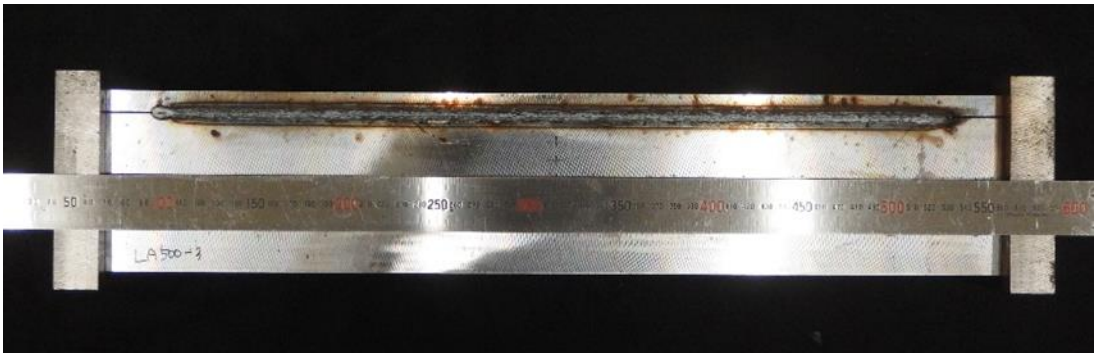

(a) Hybrid welding

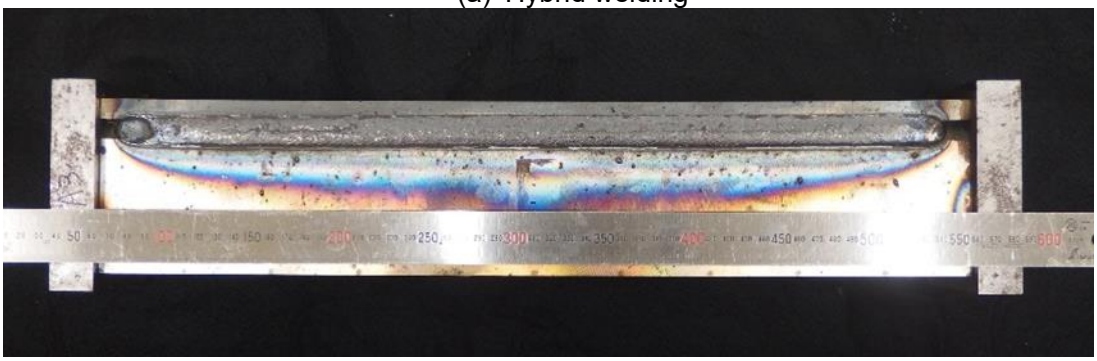

(b) Arc welding

Figure 5.4 As-welded conditions of both hybrid-welded and arc-welded specimens

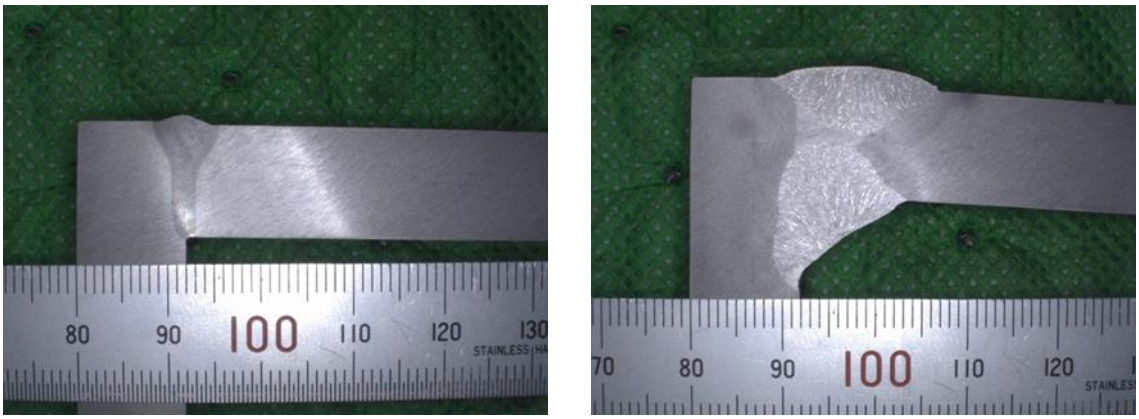

(a) Hybrid welding (b) Arc welding

Figure 5.5 Cross-sectional macroscopic photographs of joints

5.2.3 Experimental Results

(a) Temperature history

Figures 5.6 and 5.7 illustrate the temperature profiles recorded for the two types of joints. Notably, hybrid welding demonstrates a more rapid reduction in temperature compared to arc welding, leading to a pronounced temperature gradient. This substantial gradient increases the propensity for hardening phenomena in the vicinity of the weld metal.

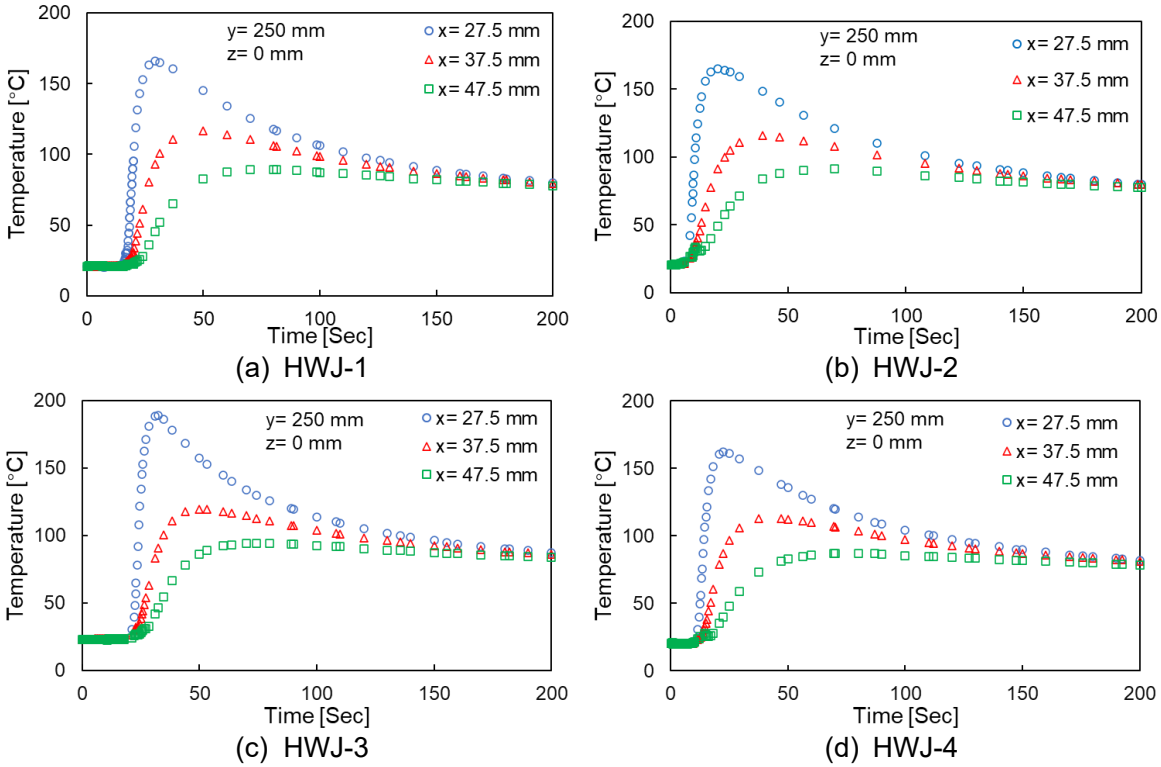

Figure 5.6 Temperature histories for hybrid welding

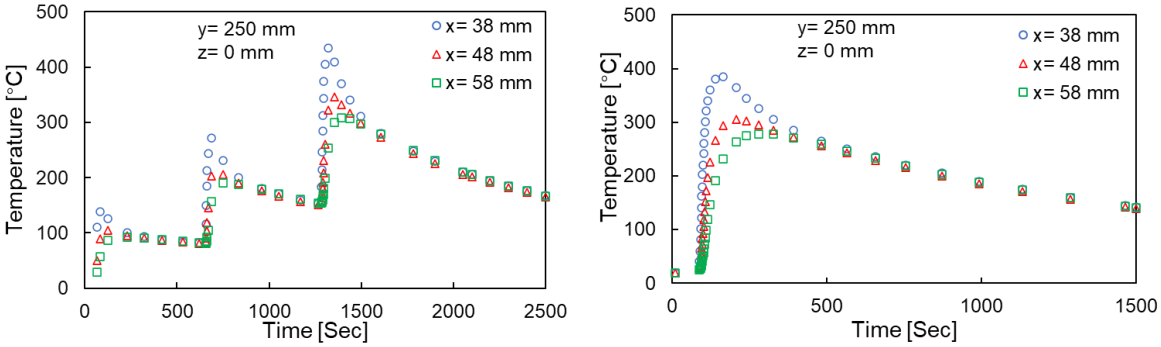

(a) Passes 1 to 3 for AWJ-1 (b) Pass 4 for AWJ-1

(c) Passes 1 to 3 for AWJ-2 (d) Pass 4 for AWJ-2

(e) Passes 1 to 3 for AWJ-3 (f) Pass 4 for AWJ-3

(g) Passes 1 to 3 for AWJ-4 (h) Pass 4 for AWJ-4

Figure 5.7 Temperature histories for arc welding

(b) Welding deformation

The out-of-plane deformations, as depicted in Figure 5.8, were determined by averaging measurements from four specimens each for the hybrid and arc welding processes. Notably, Panel 1 reported maximum deformations of 0.67 mm for hybrid-welded joints, significantly lower than the 2.37 mm observed in arc-welded joints. Similarly, Panel 2 showed deformations of 0.47 mm and 1.87 mm for hybrid and arc welding, respectively.

This marked reduction in deformation between the two welding processes is striking, with hybrid-welded specimens showcasing a reduction of approximately 70% as compared to their arc-welded counterparts. This substantial difference is predominantly attributable to the reduced heat input required in hybrid welding compared to that of arc welding. Detailed quantification of this variation in heat input is comprehensively documented in Table 5.2.

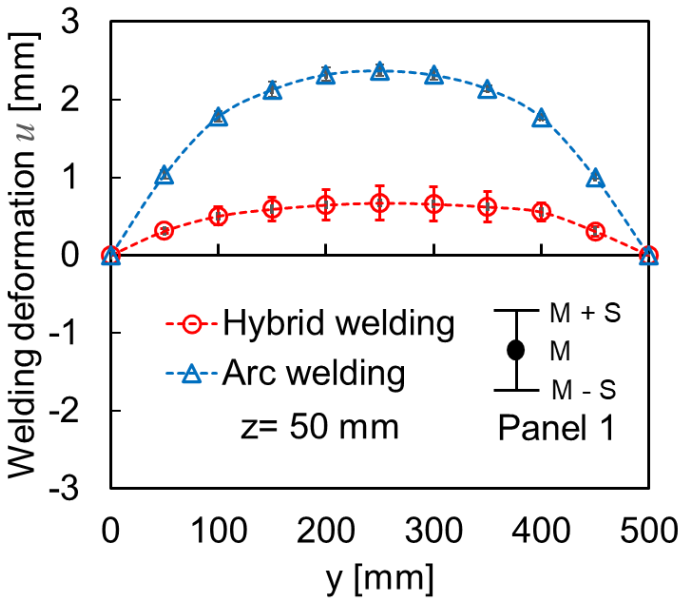

(a) Panel 1

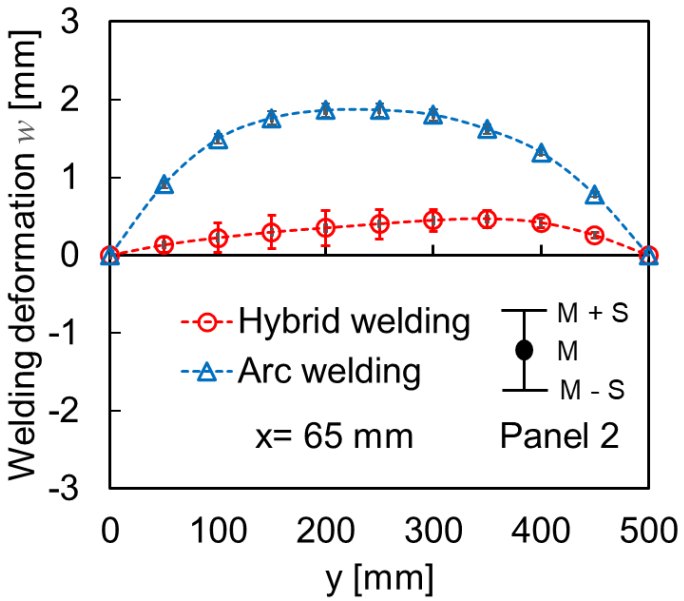

(b) Panel 2

Figure 5.8 Averaged out-of-plane deformation

(c) Residual stress

Figure 5.9 demonstrates the distribution of stress components along the welding direction for Panels 1 and 2, compiling the average residual stresses from four specimens each of both hybrid and arc welding techniques. The weld bead areas are distinctly marked: light red for hybrid welding and light blue for arc welding. Crucially, the figure reveals that the residual stresses were not directly measured on the weld beads. This omission is primarily attributable to the inherent complexities within the weld bead areas, such as intricate microstructures, pronounced temperature gradients, and rapid material properties variations, all of which can compromise the accuracy and reliability of stress measurements. Therefore, measurements were strategically performed on the surface areas immediately adjacent to the weld beads of Panels 1 and 2. This strategic approach facilitates more reliable data acquisition by effectively managing the challenges associated with the physical characteristics of the weld beads.

Experimental results demonstrated significant differences in the residual stress profiles between the two welding techniques. For Panel 1, peak compressive residual stresses were

recorded at -143.3 N/mm² for hybrid welding and -307.8 N/mm² for arc welding. In a similar fashion, Panel 2 exhibited the compressive stresses of -105.5 N/mm² in hybrid-welded joints and -188 N/mm² in their arc-welded counterparts, indicating that compressive stresses in hybrid-welded joints are approximately half those observed in arc-welded joints.

In the case of hybrid welding, tensile residual stresses emerged adjacent to the weld bead areas, precipitated by the contraction during the rapid cooling phase— an effect that was particularly pronounced in Panel 2. In stark contrast, the arc-welded specimens exhibited minimal residual stresses near the weld zones. This is likely attributable to the tempering effect of the thermal cycles from successive welding passes, which acted as a localized heat treatment to alleviate residual stress. Furthermore, the out-of-plane deformation induced by welding, which manifested as a convex configuration oriented towards the positive directions on the x and z axes, might have imposed additional bending stresses on Panels 1 and 2. This deformation is hypothesized to superimpose compressive stress onto the surfaces of the panels, potentially explaining the reduced residual stresses observed near the weld bead regions.

From the investigation above, it can be observed that, compared to arc welding, hybrid-welded joints exhibited lower compressive residual stress and out-of-plane deformation. This may imply that the load-carrying capacity of joints welded by hybrid welding could potentially be superior to those produced by arc welding.

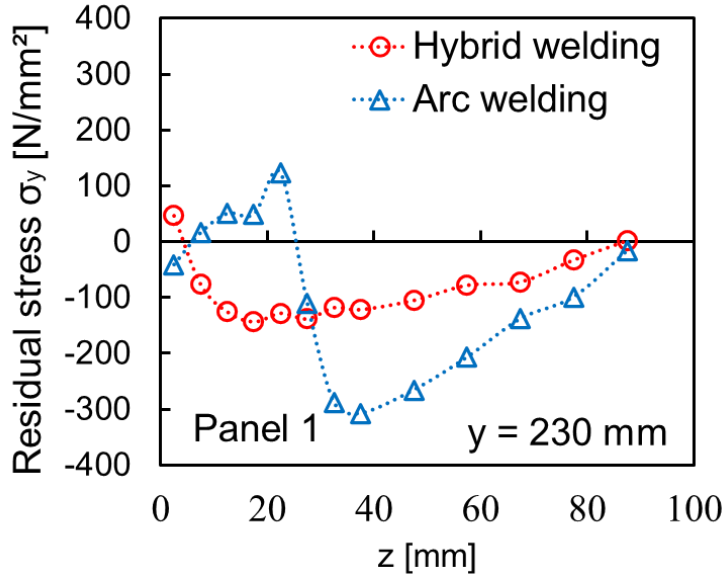

(a) Panel 1

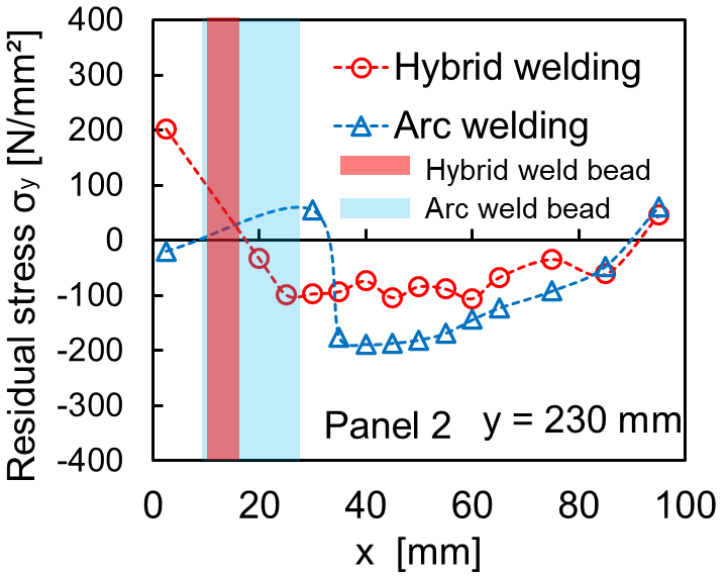

(b) Panel 2

Figure 5.9 Mean residual stress

5.3 Monotonic Compressive Loading Experiments

5.3.1 Experimental Specimens

In this section, monotonic compressive loading experiments were conducted to evaluate the load-carrying capacities of hybrid-welded joints (HWJs) and arc-welded joints (AWJs). Specifically, specimens HWJ-1, HWJ-2, HWJ-3, AWJ-1, AWJ-2, and AWJ-3 were subjected to the loading experiments. Since specimens HWJ-4 and AWJ-4 have been utilized for cross-sectional observations, they were consequently unavailable for monotonic compressive loading experiments, as elaborated in Section 5.2.2.

5.3.2 Experimental Setup

Figure 5.10 depicts the setup used for the monotonic compressive loading experiments. A universal testing machine was utilized to apply a static compressive load axially to the specimen. After confirming that the maximum load had been reached, the load was then removed. Vertical displacement was measured at the central lower surface of the loading plate.

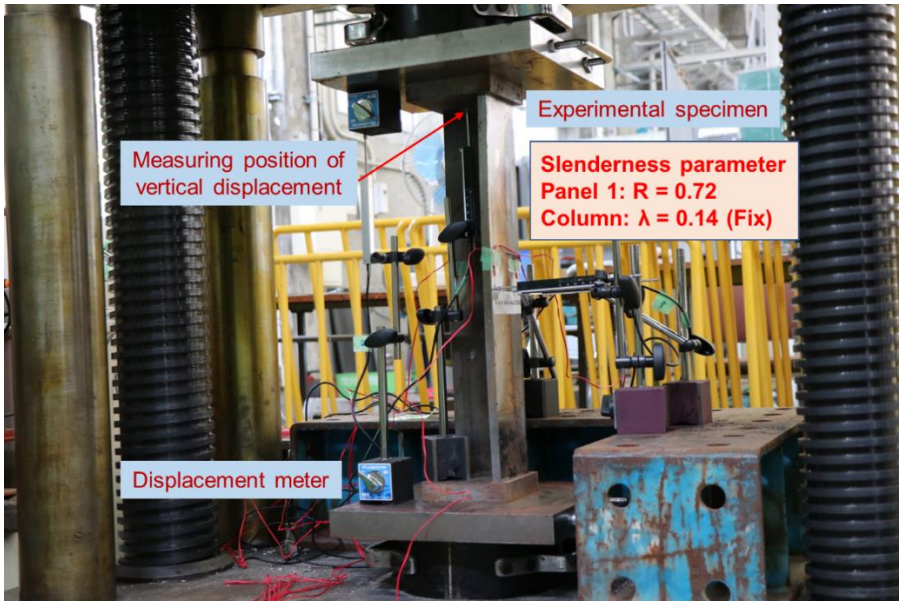

Figure 5.10 Setup for monotonic compressive loading experiments

5.3.3 Experimental Results

Figure 5.11 illustrates the relationship between compressive load and vertical displacement for two specimen types: hybrid-welded joints and arc-welded joints. The three specimens in each category demonstrated similar load-displacement behaviors. The average values for elastic stiffness and maximum compressive load are documented in Table 5.3. Due to imperfect contact between the specimen and the testing machine immediately after loading, accurate measurement of the load-displacement relationship was not feasible. Therefore, the elastic stiffness was determined within the load range of 400 to 800 kN, where the material exhibited elastic behavior. In this study, linear regression was employed to calculate the elastic stiffness, ensuring precise estimation despite the initial measurement challenges.

The average elastic stiffnesses were determined to be 864.8 kN/mm for hybrid-welded specimens and 698.1 kN/mm for arc-welded specimens. Notably, the stiffness of the hybrid-welded specimens exceeded that of the arc-welded specimens by approximately 24%, a discrepancy likely stemming from differential welding deformation. The deformation, corresponding to the welding initial deflections [5.2], [5.3] during the loading process, profoundly impacted both elastic stiffness and the maximum load capacity. As indicated in Table 5.2, arc-welded joints were subjected to a higher heat input relative to their hybrid-welded counterparts during the welding process, culminating in more substantial welding deformation. Such augmented deformation precipitated increased strains and displacements, consequently diminishing the structural stiffness. In contrast, hybrid-welded joints exhibited reduced welding deformation, which in turn, had a lesser effect on their elastic stiffness.

The average peak compressive loads for hybrid- and arc-welded specimens were respectively quantified at 1343 kN and 1280 kN. Notably, the load exhibited by the hybrid-welded specimens surpassed that of the arc-welded specimens by approximately 5%. This discrepancy can be attributed not only to differences in welding deformations but also to variations in

compressive residual stresses. Significantly, the compressive residual stress, denoted as σ_y, is identified as a pivotal factor affecting the maximum compressive loads. As depicted in Figure 5.9, the σ_y in the arc-welded specimens was higher than that in the hybrid-welded specimens, which instigated an earlier yield during the loading experiments. Such premature yielding constrains the ultimate compressive loads that arc-welded specimens can withstand.

Therefore, in light of the absence of detectable welding defects in the macroscopic cross-sectional imagery, the load-carrying capacity of the hybrid-welded joints could indeed surpass that of their arc-welded counterparts.

Table 5.3 Elastic stiffness and maximum compressive load

Specimen No.	Elastic stiffness [kN/mm]	Maximum load [kN]	Average elastic stiffness [kN/mm]	Average maximum load [kN]
HWJ-1	863.9	1350.2		
HWJ-2	860.8	1345.1	864.8	1343
HWJ-3	869.6	1332.5		
AWJ-1	693.1	1282.5		
AWJ-2	698.1	1284.6	698.1	1280
AWJ-3	703.1	1273.1		

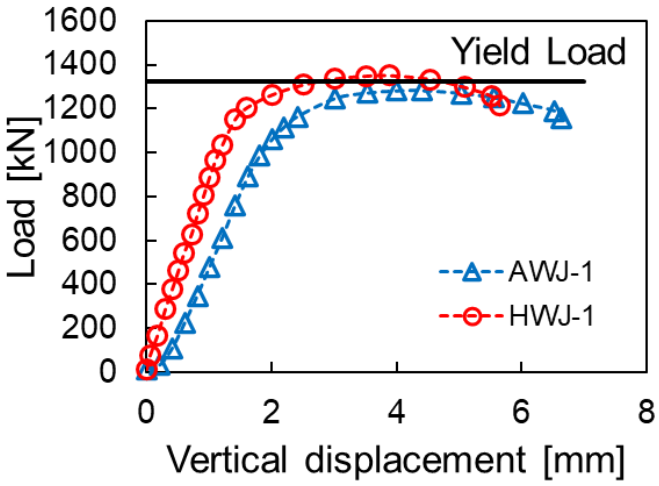

(a) Load-carrying capacity of HWJ-1 and AWJ-1

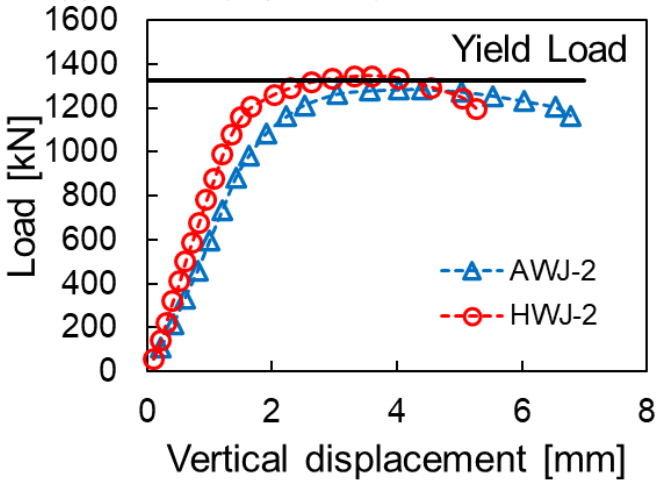

(b) Load-carrying capacity of HWJ-2 and AWJ-2

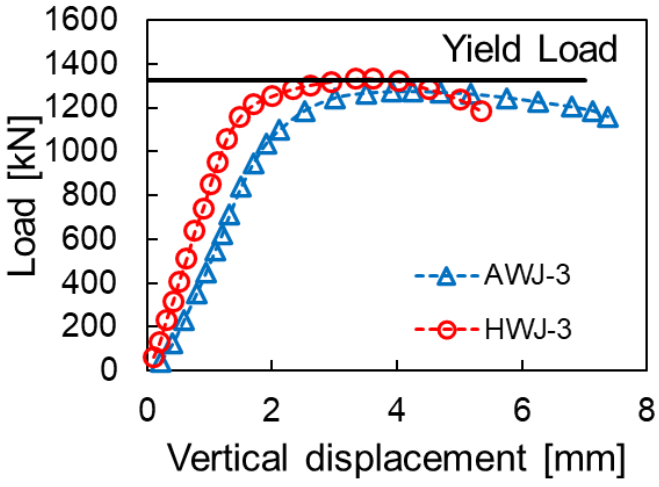

(c) Load-carrying capacity of HWJ-3 and AWJ-3

Figure 5.11 Relationship between compressive load and vertical displacement

5.4 Summary

In this chapter, one-pass full penetration hybrid-welded columns with L-shaped sections fabricated using SBHS500 were examined. For comparative analysis, joints created using conventional arc welding were also produced. Monotonic compressive loading experiments were conducted to assess the load-carrying capacity of the hybrid-welded columns. The principal findings are encapsulated as follows:

(1) The deformation resulting from welding in the hybrid-welded joints was approximately 70% less compared to the arc-welded joints. Additionally, the peak compressive residual stresses observed in the hybrid-welded joints were roughly 50% lower than those in their arc-welded counterparts.

(2) Compared to arc-welded joints, the average elastic stiffness of the specimens welded using hybrid techniques demonstrated a 24% enhancement, and the maximum average compressive load exhibited by these hybrid-welded specimens saw a 5% increase.

Reference

[5.1] Kristensen, J.K. (2009) Thick Plate CO2-Laser Based Hybrid Welding of Structural Steels. Weld World 53: 48–57. https://doi.org/10.1007/BF03266691

[5.2] Akira Tatsumi, Yuji Kageyama. (2024) Ultimate strength assessment of rectangular plates subjected to in-plane compression using a statistical model of welding initial deflection. Marine Structures 93: 103523. https://doi.org/10.1016/j.marstruc.2023.103523

[5.3] Xiang Chen, Shozo Nakamura, Toshihiro Okumatsu. et al. (2020) Formulation of the quantitative influence of local and overall initial deflections on load-bearing capacity of unstiffened welded square box section columns under axial compression. Thin-Walled Structures 147: 106539. https://doi.org/10.1016/j.tws.2019.106539

Chapter 6 Conclusions

6.1 Summary and Discussion

In this study, with the intention of broadening the application of laser-arc hybrid welding to joining steel bridge structural components, the objectives were twofold: to verify the effectiveness of hybrid welding in the fabrication of steel bridge components and to evaluate the mechanical performance of hybrid-welded joints. A series of experimental investigations and numerical simulations were conducted to achieve the aims. The subsequent sections will systematically summarize the principal insights derived from this research.

In Chapter 1, the background of this research was established by highlighting the increasing applicability of hybrid welding in the fabrication of steel bridge components. The objectives of the study were clearly defined, and the structure of this dissertation was outlined to provide a comprehensive overview of the research framework.

In Chapter 2, a hypothesized 15 mm thick SBHS400 steel plate was investigated for its feasibility of being penetrated in a single pass using hybrid welding through weld cracking experiments. The findings indicated that, under the conditions of 12.5 kW laser power, 1.6 m/min welding speed, 250 A arc current, and 28 V arc voltage, a robust welded joint could be obtained. Employing these parameters, subsequent butt welding experiments were conducted to produce hybrid-welded butt joints. Regarding time efficiency and energy preservation, hybrid welding exhibited enhancements of approximately 98% and 92%, respectively, relative to conventional arc welding.

In Chapter 3, the hybrid-welded butt joints crafted in Chapter 2 were utilized to assess out-of-plane deformations and residual stresses. A thermal elastic-plastic analysis was executed to illuminate the intricate distribution of these deformations and stresses. A numerical simulation model for hybrid welding was developed by combining the different heat sources with laser and

arc welding. For a comparative evaluation, analogous measurements and simulations were performed on conventionally arc-welded butt joints. This analysis yielded several notable conclusions. The angular distortions measured were 0.6 mm for hybrid welding and 10.8 mm for arc welding, indicating a reduction in angular distortion by 95% in hybrid welding compared to arc welding. The peak compressive residual stress along the weld line direction in hybrid welding was approximately 70 N/mm² lower than that observed in arc welding. Additionally, the range of tensile residual stress was diminished by roughly 50%. Owing to the reduced out-of-plane deformation elicited by hybrid welding, it was postulated that hybrid welding could enhance the compressive load-carrying performances of welded structures relative to arc welding. Moreover, a significant reduction of 125 N/mm² in tensile residual stress along the transverse direction was noted in hybrid welding compared to arc welding. Consequently, butt joints using hybrid welding were posited to exhibit enhanced fatigue strength when contrasted with those fabricated via arc welding. In addition, material hardening was observed in the heat-affected zone (HAZ) and weld metal (WM) of hybrid-welded joints, a phenomenon that could diminish the toughness of welded joints and elevate the risk of failure under sudden or unpredictable loads. As a result, Chapter 3 proposed two inferences and one concern.

Chapter 4 validated one of the inferences and addressed the concern raised. To elucidate the fatigue characteristics of hybrid-welded joints using SBHS400, four-point bending fatigue tests were conducted. Given the limited research on the fatigue properties of hybrid-welded joints, this study is pivotal for accumulating essential data for their practical application. The fatigue tests undertook a comparative analysis with arc-welded joints as a basis. According to the findings from fatigue tests, when subjected to nominal stress ranges exceeding 250 N/mm², hybrid-welded joints demonstrated fatigue strengths that were equivalent to or surpassed those of arc-welded joints. This enhanced performance was attributed to the hardening around the weld toe, which significantly contributed to strength augmentation and mitigates the initiation and

early-stage propagation of cracks. Following the application of a 4/5 conversion factor, in alignment with the JSSC guidelines, hybrid-welded joints adhered to the class D design curve requirements. In contrast, arc-welded joints exhibited suboptimal performance under similar high-stress conditions. By contrasting these two types of joints, the fatigue test results provided a clearer understanding of the specific benefits and limitations inherent in the use of hybrid welding technology, thereby contributing to its advancement and implementation in structural applications. In addition, to address the concern mentioned above, the Charpy impact test was conducted to provide a straightforward indicator of toughness via the Charpy absorbed energy. This evaluation focused on the toughness of the heat-affected zone (HAZ) and weld metal (WM) within the hybrid-welded joint. However, the occurrence of fracture path deviation (FPD) in all test pieces extracted from both the HAZ and WM presented challenges in accurately assessing the Charpy absorbed energy. As an alternative approach, simulated test pieces were meticulously fabricated to closely replicate the actual metallographic structures of the HAZ. For comparative purposes, traditional SM400B steel underwent the identical thermal cycle as the simulated HAZ. The subsequent Charpy impact tests on these pieces revealed that both SBHS400 and SM400B met their respective requirements— 47 J for SBHS400 and 27 J for SM400B— at temperatures of 900°C and 1050°C. However, at elevated temperatures of 1200°C and 1350°C, only SBHS400 consistently achieved the required 47 J, indicating enhanced toughness, while SM400B failed to meet its required 27 J. This suggests that SBHS400 likely offers superior toughness in the heat-affected zones of hybrid-welded joints compared to SM400B.

Chapter 5 resolved another inference previously proposed in Chapter 3. The columns with L-shaped sections assembled by one-pass full-penetration joints of SBHS500 with a thickness of 12 mm were constructed using hybrid welding. For comparison, columns with the same dimensions and L-shaped sections assembled by identical full-penetration joints were also

produced using arc welding. The welding deformation experienced by the hybrid-welded joints was significantly reduced, showing approximately 70% less distortion compared to the arc-welded joints. Furthermore, the peak compressive residual stress observed in the hybrid-welded joints was about 50% lower than that in their arc-welded counterparts. Monotonic compressive loading experiments were conducted to assess the load-carrying capacities of both types of welded joints. The results revealed that the hybrid-welded joints exhibited a 24% increase in average elastic stiffness and a 5% increase in maximum mean compressive load compared to the arc-welded joints.

6.2 Effectiveness of Hybrid Welding in Fabricating Steel Bridge Components

In this section, to verify the effectiveness of laser-arc hybrid welding in fabricating steel bridge structural components, this dissertation systematically evaluated its potential through four distinct lenses: manufacturing efficiency, economic efficiency, mechanical properties, and alignment with Sustainable Development Goals (SDGs). Interviews with five domestic bridge manufacturers were conducted to explore this topic, incorporating both the experimental and analytical results obtained from hybrid and arc welding in this study. This approach enabled a comprehensive assessment of the implications and potential advantages of hybrid welding in bridge construction.

(a) Manufacturing efficiency

The welding experiments conducted in this study demonstrated that hybrid welding can achieve substantially higher welding speeds compared to conventional arc welding. Specifically, for butt joint welding, the speed of arc welding ranged from 0.15 m/min to 0.25 m/min, while hybrid welding reached speeds up to 1.6 m/min, thereby reducing the welding time for butt joints

by over 98%. For corner joint welding, the speed increased from 0.20 m/min to 0.35 m/min in arc welding to 1.2 m/min in hybrid welding, achieving a time reduction of more than 94%. Additionally, the use of single-pass penetration in hybrid welding eliminates the need for inter-pass cooling time required in arc welding, further reducing the total construction time.

Interviews revealed that submerged arc welding and semi-automatic arc welding are predominantly used in field operations. For butt joint welding of 15 mm thick steel plates, submerged arc welding is typically performed at speeds ranging from 0.3 m/min to 0.45 m/min, usually involving about two passes with bevels on both sides. Semi-automatic welding is carried out at speeds between 0.25 m/min and 0.4 m/min, requiring approximately four to six passes with beveling on one side and including backside operations. The length of welds for butt-jointed components, such as in plate connections, correlates to dimensions such as web height or flange width, with a maximum of approximately 3500 mm.

This research also explored the potential time-saving effects of replacing these conventional welding methods with hybrid welding, offering a detailed assessment of efficiency gains within the context of modern structural engineering practices. Assuming the same hybrid welding conditions as in the experimental setting and arc welding conditions under semi-automatic settings with a welding speed of 0.3 m/min and five passes on one side, hybrid welding required 131.25 seconds for a 3500 mm weld, whereas arc welding took 3500 seconds. Factoring in approximately 500 seconds for inter-pass cooling, the total time for arc welding amounted to 5500 seconds. Thus, hybrid welding reduced the welding time by approximately 5369 seconds (about 1.5 hours) compared to arc welding. These findings underscore the considerable advantages of hybrid welding, including significant reductions in welding time and the elimination of backside operations and associated tasks. However, precise gap management is crucial for successful hybrid welding, necessitating further investigation for field application. Although precision management is more feasible in factory settings, exploring the applicability of hybrid

welding even for fillet welds, which are commonly performed in factories, is considered worthwhile.

(b) Economic efficiency

The welded steel structures require a straightening process to correct welding deformations. Interviews regarding the time and economic costs associated with the straightening process during factory production revealed that it constitutes 2 to 9% of the total. Due to the variability in straightening processes among companies and the diversity of steel structural member sizes, it is challenging to generalize total production times or costs. However, it was estimated that for a 500t class bridge, the straightening process would take approximately 225 hours. In this study, hybrid welding produces less out-of-plane deformation compared to arc welding. If applied in actual construction, hybrid welding could shorten the straightening process and reduce economic costs, thus potentially affecting the cost-effectiveness of fabricating steel bridge components significantly.

(c) Mechanical property

(i) Fatigue strength

Steel bridges are frequently subjected to repetitive traffic loads, making fatigue strength a critical factor in assessing their long-term structural safety. Bridges with high fatigue strength can endure more frequent and prolonged load cycles without succumbing to material fatigue damage or cracking. As detailed in Chapter 4, fatigue test results have indicated that under nominal stress ranges exceeding 250 N/mm², hybrid-welded joints demonstrated equivalent or superior fatigue strength compared to arc-welded joints. Following the guidelines of the Japanese Society of Steel Construction (JSSC) and applying the 4/5 conversion factor, hybrid-welded joints met the standards of the Class D design curve, whereas arc-welded joints underperformed at higher

stress levels. Consequently, bridge components fabricated using hybrid welding technology are less prone to fatigue cracking when subjected to repetitive loads, significantly enhancing the reliability and lifespan of the bridge.

(ii) Toughness

The Charpy absorbed energy serves as an essential metric for evaluating the resistance of materials to fracture under impact loads. This parameter is particularly critical in low-temperature environments where steel becomes increasingly brittle and prone to fracture. Chapter 4 discussed experiments that replicated the metallographic structures within the heat-affected zone (HAZ) of hybrid-welded joints through simulated thermal cycle tests, assessing their Charpy absorbed energy. The assessments revealed that the Charpy absorbed energy in the simulated HAZ achieved the required 47 J, effectively preventing brittle fracture. This result underscores that, in cold climates or during winter's low-temperature conditions, the utilization of hybrid welding techniques in steel bridges significantly enhances structural integrity and safety. Moreover, this welding technology not only improves the mechanical properties of materials but also boosts the reliability and durability of steel bridges under extreme weather conditions.

(iii) Load-carrying capacity

The load-carrying capacity of steel bridges directly determines the maximum permissible load of the bridges, which is crucial for ensuring traffic safety and maintaining bridge functionality. Through the application of hybrid welding technology, material deformation and residual stresses induced by welding processes can be significantly reduced. Moreover, the enhancements in fatigue strength and Charpy absorbed energy contribute to improved structural integrity and safety. This augmentation not only improves the stability of the structure but also enables the design of lighter bridge structures, thereby saving on materials and costs. Furthermore, a higher

load-carrying capacity allows bridges to better withstand unexpected overload events, reducing the likelihood of structural damage resulting from such incidents.

(d) Sustainable Development Goals (SDGs)

In the context of SDGs Goal 9, which emphasizes industry, innovation, and infrastructure, the comparison of heat input between hybrid welding and conventional arc welding technologies becomes particularly relevant. As detailed in Chapters 2 and 5, hybrid welding offers a significant reduction in heat input compared to conventional arc welding. This reduction in heat input not only minimizes thermal distortion and residual stresses in welded components but also enhances the overall energy efficiency of the fabrication process.

From an industrial innovation perspective, the lower heat input associated with hybrid welding translates into improved structural integrity and performance of welded components. This is crucial for critical infrastructure projects, where the longevity and safety of steel structures such as bridges and buildings are paramount. Furthermore, the precision and control afforded by hybrid welding technology allow for more complex and finely tuned welding operations, pushing the boundaries of what can be achieved in modern construction and manufacturing processes.

Moreover, the adoption of hybrid welding aligns with the infrastructure component of SDGs Goal 9 by promoting sustainable industrial processes. By reducing energy consumption, hybrid welding supports the development of greener fabrication methods. This contributes to the construction of more sustainable infrastructures, which is vital for reducing the environmental impact of the industrial sector.

In conclusion, hybrid welding represents a pivotal advancement in welding technology with significant implications for industry, innovation, and infrastructure. Its ability to decrease heat input while enhancing component quality and production efficiency exemplifies the kind of

technological innovation that drives sustainable industrial practices, ultimately supporting the objectives of SDGs Goal 9.

From the detailed analysis above, hybrid welding technology not only significantly enhances the structural integrity and safety of steel bridges but also offers substantial economic benefits. Therefore, considering these advantages, hybrid welding technology emerges as a valuable method, particularly in bridge engineering projects with high standards.

6.3 Future Work

In this study, hybrid welding was compared with arc welding for 12 mm and 15 mm thick SBHS steel, clearly demonstrating the superiority of hybrid welding. The plate thickness commonly used in the fabrication of steel bridge components ranges approximately from 9 to 40 mm. Given this range, it is necessary to explore the application of hybrid welding to plate thicknesses exceeding 15 mm in future studies. In such cases, the feasibility of single-pass full penetration welding, which was effective in this research, might become challenging, suggesting a need for further investigation into multi-pass hybrid welding techniques. Such studies are crucial as they potentially address the complexities associated with welding thicker sections, thereby ensuring the integrity and fabrication efficiency of steel bridge components.

Acknowledgment

Amidst the COVID-19 pandemic, I overcame numerous obstacles and finally arrived in Japan at the end of 2020. In Japan, I encountered my most esteemed supervisor, Associate Professor Mikihito Hirohata. He made an unforgettable impression on me with his profound sense of responsibility, exceptional kindness, and unwavering support for his students.

Throughout my years in the lab, I benefited immensely from his enthusiastic guidance. Every time I completed a draft of my paper, he would promptly provide insightful feedback and revisions. When my research progress faltered, he displayed remarkable patience and understanding. When I expressed my desire to pursue academic visits in other countries, he supported me unconditionally. Associate Professor Hirohata is a paragon of excellence; through his conduct and words, he has shown me the kind of person I should aspire to become. I endeavor to become a professional who treats everyone with the utmost consideration and respect, fostering congenial and harmonious relationships. I wish to convey my deepest and most sincere gratitude to my supervisor for his unwavering support.

I would like to express my sincere gratitude to Professor Zaeh for allowing me to visit the Institute for Machine Tools and Industrial Management at the Technical University of Munich as a guest researcher. I had the privilege of attending seminars, broadening my horizons. I would also like to extend my special thanks to Mr. Michael Kick from TUM, who took me to the carnival and allowed me to experience authentic German culture.

I would like to express my gratitude to Professor Kamada and Professor Inui for taking the time to review my dissertation in the middle of their busy schedules.

I would like to extend my heartfelt gratitude to Dr. Koutarou Inose of IHI Corporation for his invaluable assistance with this research. Additionally, I would like to express my sincere appreciation to Mr. Naoyuki Matsumoto and Mr. Kengo Hyoma of IHI Corporation for their support and contributions to the welding experiments conducted as part of this study.

I would like to express my gratitude to Secretary Ms. Nagaoka for capturing so many wonderful moments with her camera. I am also deeply grateful to my seniors, peers, and juniors in the field of structural engineering for their support, not only in my research but also in daily life. I am especially thankful to my seniors, Ms. Natsumi Sakai and Mr. Kuya Morioka, for their exceptional guidance.

I would like to express my gratitude to the Support for Pioneering Research Initiated by the Next Generation program for providing me with scholarships and funding.

I would like to thank the staff of the Osaka Convention & Tourism Bureau for organizing a variety of activities that made my life in Osaka vibrant and colorful.

June 2024

Chen Gang

Publications

Peer-reviewed original research

[1] Experimental investigation on load-carrying performance of corner joints by laser-arc hybrid welding

G. CHEN, M. HIROHATA, K. Hyoma, N. Matsumoto and K. Inose.

Welding letters Vol.41 No.4 (2023), *p.9WL-12WL*. DOI:10.2207/qjjws.41.9WL

[2] Charpy absorbed energy in simulated heat-affected zone of laser-arc hybrid welded joints by high strength steel for bridge structures

G. CHEN, M. HIROHATA, N. Sakai, K. Hyoma, N. Matsumoto and K. Inose.

Int J Adv Manuf Technol 127, (2023), 2655–2669. https://doi.org/10.1007/s00170-023-11420-2

[3] Bending fatigue characteristics of butt joints by laser-arc hybrid welding for steel bridge members

G. Chen, N. Sakai, M. Hirohata, K. Hyoma, N. Matsumoto and K. Inose.

Vehicle and Automotive Engineering 4, (2022), 904-916. DOI: 10.1007/978-3-031-15211-5_75 (Lecture Notes in Mechanical Engineering)

[4] An investigation on laser-arc hybrid welding of one-pass full-penetration butt-joints for steel bridge members

M. Hirohata, **G. Chen**, K. Morioka, K. Hyoma, N. Matsumoto and K. Inose.

Welding in the World 66, (2021), 515-527. DOI: 10.1007/s40194-021-01221-0

International and Domestic Conferences

[1] Experimental investigation on load-carrying performance of corner joints by laser-arc hybrid welding

CHEN Gang, HIROHATA Mikihito, HYOMA Kengo, INOSE Koutarou, MATSUMOTO Naoyuki.

National Meeting of Japan Welding Society, 2023.4, Tokyo

[2] Bending fatigue characteristics of butt joints by laser-arc hybrid welding for steel bridge members

G. Chen, N. Sakai, M. Hirohata, K. Hyoma, N. Matsumoto, K. Inose.

4th International Conference on Vehicle and Automotive Engineering, 2022.9, Hungary (online)

[3] Characteristics of Charpy Absorbed Energy in HAZ of Laser-arc Hybrid Welded Joints
G. CHEN, M. HIROHATA, N. Sakai, K. Hyoma, N. Matsumoto and K. Inose.

The 75th IIW Annual Assembly and International Conference, 2022.7, Tokyo